Turbine–Diffuser Interaction

Von der Fakultät für Maschinenbau
der Gottfried Wilhelm Leibniz Universität Hannover
zur Erlangung des akademischen Grades
Doktor-Ingenieur
genehmigte Dissertation

von

Dajan Mimic, M. Sc.

2021

Schlagwörter:
Turbine, Diffusor, Grenzschicht, Radialspalt-Wirbel, Strömungsablösung

Keywords:
Turbine, diffuser, boundary layer, tip-leakage vortex, flow separation

Vorsitzender: Prof. Dr.-Ing. Eduard Reithmeier
1. Referent: Prof. Dr.-Ing. Jörg Seume
2. Referent: Prof. Seung Jin Song

Tag der Promotion: 13. November 2020

Abstract

Diffusers increase the power output and cycle efficiency of gas turbines by reducing the back pressure of the turbine, thus, increasing the work extracted from the fluid by the turbine. They are, however, challenging to design. This is due to the inherent predisposition of the flow to separate under the adverse pressure gradients generated by diffusers, hence negating their benefit. This condition of imminent flow separation is aggravated because diffuser designers seek ever-shorter diffusers with correspondingly steeper opening angles and, thus, higher adverse pressure gradients, to reduce frictional losses and costs.

This work presents a novel theory of turbine–diffuser interaction. More specifically, this theory addresses the stabilisation of diffuser boundary layers induced by tip-leakage vortices from an upstream rotor.

The theory provides a framework to characterise tip-leakage vortices based upon integral stage-design parameters. The stage parameters loading coefficient, flow coefficient, swirl angle, and non-dimensional blade-passing frequency have been identified as the determinants for the intensity, orientation, and duty cycle of the tip-leakage vortices. These parameters have been condensed into the stabilisation number as a predictor for the inflow-dependent diffuser performance. Several hypotheses are derived from the theory and subsequently confirmed using partially scale-resolving simulations and experimental data.

Additionally, a prediction method for the vortex-induced boundary-layer stabilisation in annular diffusers has been developed. The results of the prediction method are shown to be consistent with the theory presented.

Zusammenfassung

Diffusoren steigern die Leistung sowie den Wirkungsgrad von Gasturbinen, indem sie den Gegendruck der Turbine herabsenken und somit den Arbeitsumsatz in der Turbine erhöhen. Jedoch ist die Auslegung von Diffusoren herausfordernd. Dies ist auf die inhärente Neigung von Strömungen zurückzuführen, unter Einwirkung adverser Druckgradienten, wie sie in Diffusoren vorliegen, abzulösen und somit den Nutzen des Diffusors zunichte zu machen. Dieser Umstand wird dadurch verschärft, dass kürzere Diffusoren mit folglich größeren Öffnungswinkeln und somit ausgeprägteren adversen Druckgradienten wünschenswert sind, um Totaldruckverluste und Kosten zu senken.

Die bisherige Forschung hat gezeigt, dass die Sekundärströmungsstrukturen in der Abströmung der Turbine durchaus positiv auf die Grenzschicht des Diffusors einwirken können. In dieser Arbeit wird eine neuartige Theorie der Turbine-Diffusor-Interaktion vorgestellt. Genauer gesagt, adressiert diese Theorie die Stabilisation der Diffusor-Grenzschichten durch Radialspaltwirbel eines stromauf liegenden Rotors.

Die Theorie liefert ein Grundgerüst für die Charakterisierung des Radialspaltwirbels basierend auf integralen Stufenkennzahlen. Die Stufenkennzahlen Leistungszahl, Durchflusszahl, Abströmwinkel und dimensionslose Schaufelwechselfrequenz wurden als die ausschlaggebenden Faktoren der Intensität, Orientierung sowie des Tastgrads der Radialspaltwirbel identifiziert. Diese Parameter wurden zu einer Stabilisationskennzahl zusammengeführt, welche als Vorhersagewerkzeug für die zuströmbedingungsabhängige Leistungsfähigkeit des Diffusors dient. Eine Reihe an Hypothesen wird aus der Theorie abgeleitet und anschließend anhand partiell skalenauflösender Simulationen sowie experimenteller Daten bestätigt.

Zusätzlich wurde eine Vorhersagemethode für die wirbelinduzierte Grenzschichtstabilisation in Ringdiffusoren entwickelt. Es wird gezeigt, dass deren Ergebnisse zur vorgestellten Theorie konsistent sind.

Acknowledgements

The research presented in this thesis was conducted at the Institute of Turbomachinery and Fluid Dynamics, Leibniz Universität Hannover, between February, 2016 and September, 2020.

I am grateful to my advisor, Prof. Dr.-Ing. Joerg R. Seume, for giving me the opportunity to pursue my doctoral degree at the Institute of Turbomachinery and Fluid Dynamics and for his valuable comments to my work.

I would like to thank my second advisor, Prof. Seung Jin Song from Seoul National University, for giving the impetus to devise the prediction method for the vortex-induced boundary-layer stabilisation presented in this thesis.

I would like to thank Prof. Dr.-Ing. Eduard Reithmeier, the chair of my thesis committee.

I would also like to thank Dr.-Ing. Florian Herbst, who guided me through the initial years of my doctoral studies, for the numerous fruitful discussions which often challenged me to sharpen my reasoning.

My sincere thanks are due to Dr.-Ing. Stephan Behre and Dr.-Ing. Robert Kluxen, my advisors during my master's studies, who introduced me to the field of turbomachinery research.

Thanks to Sven Schumacher, the system administrator at the Institute of Turbomachinery and Fluid Dynamics, for his support in solving many computing-related challenges.

I would also like to express my gratitude to my friends and colleagues, especially Christoph Jätz, Hye Rim Kim, Philipp Sauer, and Marcel Oettinger, who are with me on this exciting journey.

I am forever indebted to my parents, Graziella and Husein Mimic, who support me unconditionally and never cease to encourage me.

Dajan Mimic
Hanover, Germany
October, 2020

Contents

List of figures

Nomenclature

Roman symbols

Symbol	Unit	Description	Defined by *Eqn.*
a		generic coefficient	
A	m^2	area	
$\mathfrak{A}$	–	area ratio	(1.15)
B	–	diffuser blockage	(1.38), (1.39), (3.67)
C_f	–	skin-friction coefficient	(3.69)
C_p	J/K	isobaric heat capacity	
C_S	K	Sutherland constant	
C_V	J/K	isochoric heat capacity	
c_p	–	static-pressure recovery coefficient	(1.18)
c	–	calibration constant	
c_p	J/kg K	specific isobaric heat capacity	(3.36)
c_V	J/kg K	specific isochoric heat capacity	(3.36)
E	m/s	entrainment rate	(3.65)
E	J	internal energy	
E_tot	J	total energy	(3.26)
e	J/kg	specific internal energy	
e_tot	J/kg	specific total energy	
F	–	non-dimensional blade-passing frequency	(4.26)
$\mathbf{F}$		flux vector	(5.3)
f	1/s	frequency	
f	$\mathrm{N/m^3}$	volume-specific force	
$\mathbf{f}$	$\mathrm{N/m^3}$	volume-specific force vector	
$\mathscr{f}$		generic function	
H	–	shape factor	(1.36)
h	J/kg	specific enthalpy	(1.1)
h	–	shape parameter	(3.70)
$\mathbf{I}$	–	identity matrix	(3.11)
J	kg m/s	momentum	
$\mathbf{J}$	kg m/s	momentum vector	
k	$\mathrm{m^2/s^2}$	turbulent kinetic energy	
ℓ	m	characteristic length	
M	kg/mol	molar mass	
m	kg	mass	
Ma	–	Mach number	(3.44)

Symbol	Unit	Description	Defined by *Eqn.*
N	1/s	rotor speed	
n	–	blade count	
$\mathcal{P}$		production term	
p	Pa	pressure	(3.9)
Pr	–	PRANDTL number	(3.41)
Q	m^2/s	volume-flow rate per unit span	
$\dot{Q}$	J/s	heat-flow rate	
$\mathbf{Q}$		source vector	(5.4)
$\mathcal{Q}$	J	dissipation function	(3.31)
q	J/kg	specific heat quantity	
$\mathbf{q}$	J/m^2 s	heat-flux vector	
R	J/kg K	specific gas constant	
R	1/s	rotation rate	
$\mathbf{R}$	1/s	rotation-rate tensor, rotation-rate vector	(3.74)
$\mathcal{R}$	J/mol K	universal gas constant	
r	m	radius	
r	m	characteristic radius	
Re	–	REYNOLDS number	(3.43)
S	1/s	strain rate	
$\mathbf{S}$	1/s	strain-rate tensor	(3.14), (3.15)
$\mathbf{S}^*$	1/s	traceless strain-rate tensor	(3.19)
$\mathcal{S}$	m^2	characteristic surface	
s	J/kg K	specific entropy	
T	K	temperature	
$\mathcal{T}$	s	characteristic time scale	
t	s	time	
$\mathbf{U}$		state vector	(5.2)
$\mathcal{U}$	m/s	characteristic velocity	
u	m/s	flow velocity	
$\mathbf{u}$	m/s	flow-velocity vector	
u_τ	m/s	shear velocity	(4.13)
V	m^3	volume	
$\mathcal{V}$	m^3	characteristic volume	
v	m/s	velocity	
W	J	work	
$\mathcal{W}$	m	diffuser width (planar), diffuser channel height (annular)	
w	J/kg	specific work	
x	m	spatial coordinate	

Greek symbols

Symbol	Unit	Description	Defined by *Eqn.*
α	°	swirl angle	
Γ	$\mathrm{m^2/s}$	circulation	(3.78)
γ	–	heat-capacity ratio	(3.37)
Δ		difference	
δ	°	diffuser half-opening angle	
δ	m	boundary-layer thickness	
δ^*	m	displacement thickness	(1.29)
ϵ	–	diffuser effectiveness	(1.35)
ζ	–	total-pressure loss coefficient	(1.27)
η	–	efficiency	(1.1)
θ	°	circumferential coordinate	
ϑ	m	momentum thickness	(1.30)
κ	–	von Kármán constant	
Λ	–	boundary-layer blockage	(3.68)
λ	$\mathrm{kg/m\,s}$	Lamé constant	
λ	$\mathrm{J/m\,s\,K}$	thermal conductivity	
μ	$\mathrm{kg/m\,s}$	dynamic viscosity	
ν	$\mathrm{m^2/s}$	kinematic viscosity	
Ξ	–	extrapolation factor	(4.36)
ξ	–	dynamic-pressure coefficient	(1.25)
ρ	$\mathrm{kg/m^3}$	density	
Σ	–	stabilisation number	(4.30)
σ	$\mathrm{N/m^2}$	stress	
$\boldsymbol{\sigma}$	$\mathrm{N/m^2}$	Cauchy stress tensor	(3.8)
τ	$\mathrm{N/m^2}$	deviatoric stress	
$\boldsymbol{\tau}$	$\mathrm{N/m^2}$	deviatoric stress tensor	(3.12)
Φ	–	flow coefficient	(4.23)
Φ	J	potential energy	
ϕ	$\mathrm{J/kg}$	specific potential energy	
ϕ		generic flow variable	
φ	°	generic angle	
Ψ	–	loading coefficient	(4.22)
Ω	1/s	vorticity	
$\boldsymbol{\Omega}$	1/s	vorticity vector	(3.76)
ω	1/s	specific turbulence-dissipation rate	

Sub- and Superscripts

Symbol	Description	Type
BL	boundary layer	Subscript
BP	blade passing	Subscript
C	compressor	Subscript
calib	calibrated	Subscript
cas	casing	Subscript
ch	chord	Subscript
D	diffuser	Subscript
dyn	dynamic	Subscript
eff	effective	Subscript
hub	hub	Subscript
id	ideal	Subscript
in	inlet	Subscript
is	isentropic	Subscript
out	outlet	Subscript
p	pitch	Subscript
rel	relative	Subscript
rev	reversible	Subscript
rot	rotor	Subscript
sep	separation	Subscript
sys	system	Subscript
T	turbine	Subscript
th	thermal	Subscript
tot	total	Subscript
turb	turbulent	Subscript
U	useful	Subscript
∞	free stream, infinity	Subscript
$+$	non-dimensional	Superscript

Further symbols

Symbol	Description
$\boxtimes$	generic placeholder
$\otimes$	dyadic product
$:$	double-dot product
$\boldsymbol{\nabla}\boxtimes$	gradient operator
$\boldsymbol{\nabla}\cdot\boxtimes$	divergence operator
$\boldsymbol{\nabla}\times\boxtimes$	curl operator
$(\boxtimes\otimes\boldsymbol{\nabla})$	vector-gradient operator
$\boldsymbol{\nabla}^2\boxtimes$	(vector) Laplacian operator
$\operatorname{sgn}(\boxtimes)$	sign function

Symbol	Description
$\mathrm{tr}(\boxtimes)$	trace operator
$\lvert \boxtimes \rvert$	modulus
$\lVert\boxtimes\rVert_F$	Frobenius norm
$\lVert\boxtimes\rVert_2$	Euclidean norm
$\max(\boxtimes_1; \boxtimes_2)$	the greater of $\boxtimes_1$ and $\boxtimes_2$
$\min(\boxtimes_1; \boxtimes_2)$	the lesser of $\boxtimes_1$ and $\boxtimes_2$
$\boxtimes_1 \propto \boxtimes_2$	$\boxtimes_1$ is proportional to $\boxtimes_2$
$\boxtimes_1 \sim \boxtimes_2$	$\boxtimes_1$ scales with $\boxtimes_2$

Acronyms

Acronym	Meaning
CPF	cross-passage flow
DLR	*Deutsches Zentrum für Luft- und Raumfahrt* (German Aerospace Center)
HSV	horseshoe vortex
ILU factorisation	incomplete lower-upper factorisation
MUSCL	monotonic upstream-centered scheme for conservation laws
NACA	National Advisory Committee for Aeronautics
PV	passage vortex
RANS	Reynolds-averaged Navier–Stokes
SAS	scale-adaptive simulation
SST	shear-stress transport
TFV	trailing-filament vortex
TRACE	Turbomachinery Research Aerodynamic Computational Environment
(2G-)URANS	(second-generation) unsteady Reynolds-averaged Navier–Stokes

Abbreviations

Abbreviation	Meaning
App.	*Appendix*
Ass., Asss	*Assumption, Assumptions*
Chap.	*Chapter*
Con.	*Conclusion*
Eqn., Eqns	*Equation, Equations*
Fig., Figs	*Figure, Figures*
Hyp., Hyps	*Hypothesis, Hypotheses*
Imp., Imps	*Implication, Implications*
Lst.	*Listing*
p.	*Page*
Sec., Secs	*Section, Sections*

Introduction

Diffuser flows pose a *formidable challenge* to both turbomachinery engineers and aerodynamicists. Diffusers convert the kinetic-energy density of a flow into static pressure, thereby decelerating the flow. In the case of subsonic flow, this is achieved by increasing the cross-sectional area in the stream-wise direction.

This passive energy conversion comes in very useful in the context of turbomachinery where diffusers are employed mainly at the inlet of aircraft engines, downstream of compressors, as transitional ducts between turbine stages, and as exhaust diffusers downstream of turbines. By raising the pressure of the turbine outflow before it encounters ambient conditions upon leaving the gas turbine, an exhaust diffuser allows for lower pressure levels at the turbine outlet. This, in turn, improves the turbine performance, as the flow can be expanded across a greater pressure difference and more work can be extracted by the turbine.

This desirable increase in static pressure, at the same time, defines the *challenge* which diffuser designers have to face: the flow has to overcome an adverse pressure gradient. The low-momentum flow regions adjacent to the diffuser walls—the boundary layers—are prone to flow separation when confronted with adverse pressure gradients. This issue is aggravated when it becomes an additional objective to reduce the diffuser length in order to decrease frictional losses and manufacturing cost. An increase in pressure rise and decrease in diffuser length necessitate an increased aerodynamic loading, often achieved by increasing the opening angle of the diffuser. Such *highly loaded diffusers* tend to exhibit *massive flow separation:* a state where the flow is no longer guided by the diffuser walls and large recirculation zones form. The deceleration of the core flow and, therefore, its pressure rise are severely impeded by this occurrence.

The *challenge* encountered by aerodynamicists lies in the great uncertainty in the prediction of such violently separated flows. It is not for nothing that the accurate prediction of boundary-layer separation—and reattachment, for that matter—represents a cornerstone when validating and assessing turbulence and transition models. Not only the prediction, but also the measurement of massive flow separation poses several problems due to the highly unsteady and three-dimensional nature of the flow.

The complexity of this task is exacerbated by the fact that a diffuser downstream of a turbine experiences an already unsteady and three-dimensional inflow. Wakes and vortices emerging from the turbine, together with circumferential velocity components, interact with the boundary layers in the diffuser and give rise to a series of intriguing effects. The most astounding observation is probably that vortices generated at the tip of the turbine blades—structures associated with high losses and performance decrease in turbomachines—can actually serve to *increase the static-pressure rise* in the subsequent diffuser.

The purpose of this work is to devise a theoretical framework that allows a *qualitative understanding* of the mechanisms involved in the process of turbine–diffuser interaction and a *quantitative prediction* of their impact on diffuser performance.

Epistemology

One fundamental question precedes all research: *How can we gather knowledge about the nature surrounding us?* Popper (1994) articulated a theoretical framework which, even if it is not an accurate representation of the *reality of science*, provides a useful, structured approach. This framework is usually referred to as the *scientific method* and distinguishes between the different stages of the scientific cognition process.

The process begins with a *question;* this question is often derived from a particular *observation.* Based upon the current *theory,* the observer then formulates a *hypothesis*. The hypothesis is essentially any "if–then" statement: it states conditions under which a certain outcome is predicted. In order to determine whether the hypothesis can be confirmed or not, the observer devises an *experiment,* which recreates the conditions premised. The theory is considered valid if the hypothesis is confirmed. If the hypothesis is not confirmed, the theory has to be revised and new hypotheses need to be formulated to test the new theory. In this context, it is a central aspect of a scientific theory that it must be *falsifiable.* This means that it must be possible to derive hypotheses from the theory which can potentially be shown to be false.

In engineering

The above cognition process is closely related to the philosophy of natural sciences. In the field of engineering, the fundamental question about the acquisition of knowledge is accompanied by the rather practically oriented question: *Which pieces of information do we need?* The main implication of this question is that theories in engineering serve an external purpose. Often, this purpose is to provide information or rule sets—or, more generally, a framework—with the goal of enabling, facilitating, or improving a system or design process. This entails two general principles:

1. It must be possible to derive hypotheses from the theory proposed which contain predictions about relevant quantities.
2. It must be possible to derive hypotheses from the theory proposed which apply under the conditions available in the intended application.

The theory must, therefore, be *accessible* to its intended users. It can be argued, from this point of view, that intuitive explanations of phenomena, easy-to-handle tools and time-efficient methods are to be favoured over unnecessary complexity.

The same goes for *models* derived from the theories. If theories are understood as the abstract description of systems, objects, and processes, then models represent the manifestation of these descriptions as quantitative relationships. Consequently, models should generate predictions about the quantities of interest from easily obtained input parameters while displaying stable behaviour and computational efficiency.

In this work

This work does not contest the established theories of fluid dynamics and all predictions can probably, at least in principle, be derived from high-fidelity flow simulations with sufficiently accurate boundary conditions. Nevertheless, it seemed prudent to adhere to the maxims laid out above.

For this reason, an attempt was made to describe the turbine–diffuser interaction in terms of different features, which were treated as conceptual objects: free stream, boundary layer, and vortex. These features were modelled in a simple and rather fundamental way, which, due to the clear distinction between these objects, serves to facilitate future incremental improvements. Likewise, the most fundamental descriptions of exchange processes between these objects were favoured. This comprises, e.g., a very basic consideration of turbulence effects in the form of an artificial viscosity. Also, regression analyses of a higher order than warranted by the data were avoided.

This was partially driven by the vanity to find an *elegant* explanation of the matter, but even more so by the optimism that this theory can be expanded to cover a broader class of flow problems in the future: different diffuser types, diffusers downstream of compressors, and intermediate ducts with adverse pressure gradients. Moreover, it is to be hoped that the intended rigour will help to identify open questions concerning vortex–boundary-layer interactions as well as prospective research to answer these questions.

Structure

Derived from the cognition process explained and the ambitions expressed above, this work is structured in eight major parts.

1. The chapter *Problem* lays out the necessity for diffusers, the problem associated with diffuser flows and the benefit of a *concurrent design approach* towards turbines and diffusers.
2. The chapter *Literature* reviews the state of current diffuser research with a focus on the stabilisation of diffuser flows, i.e., the prevention or reduction of boundary-layer separation.
3. The chapter *Fundamentals* introduces the fundamentals of fluid dynamics and turbomachinery flows necessary to understand the interaction mechanisms between turbine and diffuser.
4. The chapter *Theory* introduces and details the theory of turbine-induced effects on the diffuser performance. A series of hypotheses are derived, which refer to individual stages of the interaction process.
5. The chapter *Method* presents the experimental and numerical configurations that were used to gather the data used to test the hypotheses.
6. The chapter *Evidence* comprises the testing and discussion of the individual hypotheses.
7. The chapter *Applicability* summarises the relationships established in the previous chapter and explains how they can be used in turbomachine design processes.
8. The chapter *Conclusions* reiterates the findings of this work, shows the limitations of the theory and gives an outlook on prospective research.

Chapter 1.

Problem

Diffusers increase the power output and cycle efficiency of gas turbines by reducing the back pressure of the turbine, thus, increasing the work extraction from the fluid in the turbine. They are, however, challenging to design. This is due to the inherent predisposition of the flow to separate under adverse pressure gradients as they are generated by diffusers, hence, negating their benefit. This condition of imminent flow separation is aggravated because diffuser designers seek ever-shorter diffusers with, consequently, steeper opening angles and, thus, higher adverse pressure gradients, to reduce frictional losses and costs.

1.1. Gas-turbine cycle

To understand why the use of diffusers is beneficial to overall gas-turbine performance, it is helpful to consider the gas-turbine cycle, i.e., the open BRAYTON cycle*. As can be seen in *Fig.* 1.1, this cycle consists of the distinct phases *compression, heating, and expansion.* During the compression process, the compressor performs the specific compression work w_C, whereby the total specific enthalpy h_tot and total pressure p_tot of the fluid are increased. Naturally, this exchange of work is tied to an increase in entropy. The *isentropic compressor efficiency* quantifies how closely a real compression process corresponds to its isentropic counterpart:

$$\eta_\mathrm{is,C} := \frac{w_\mathrm{C,rev}}{w_\mathrm{C}} = \frac{h_\mathrm{tot,3,is} - h_\mathrm{tot,2}}{h_\mathrm{tot,3} - h_\mathrm{tot,2}}, \tag{1.1}$$

where the subscripts "rev" and "is" stand for *reversible* and *isentropic,* respectively. The specific heat quantity q is added in the subsequent combustor.

In contrast to the compressor, the turbine extracts the specific expansion work w_T from the fluid. As a result, both total enthalpy and total pressure of the fluid decrease. Again, the real change of states can be quantified in relation to an isentropic expansion process via the *isentropic turbine efficiency:*

$$\eta_\mathrm{is,T} := \frac{w_\mathrm{T}}{w_\mathrm{T,rev}} = \frac{h_\mathrm{tot,5} - h_\mathrm{tot,4}}{h_\mathrm{tot,5,is} - h_\mathrm{tot,4}}. \tag{1.2}$$

Since the turbine drives the compressor, some of the work extracted is redirected to the compressor. The remaining work is called the *specific useful work* w_U and can be defined as

$$w_\mathrm{U} := w_\mathrm{C} + w_\mathrm{T}. \tag{1.3}$$

---

*also referred to as JOULE cycle

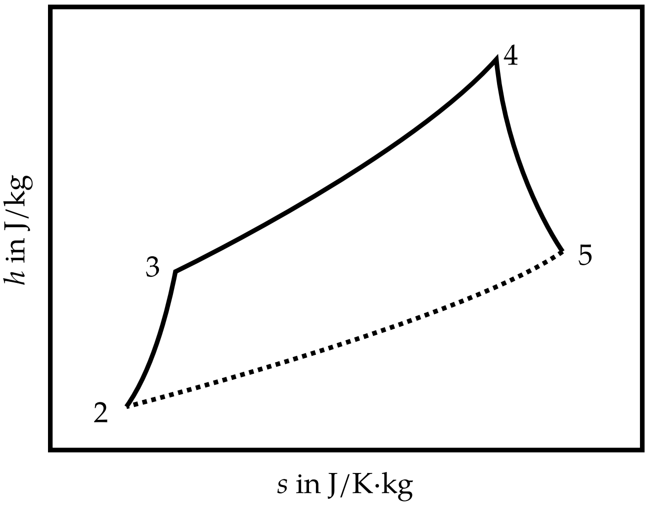

Figure 1.1.: Mollier diagram of the open Brayton cycle

The efficiency of the overall cycle, i.e., the cycle thermal efficiency, is defined by the ratio of useful work extracted from the cycle to the heat input:

$$\eta_{\text{th}} := \frac{|w_{\text{U}}|}{q}. \tag{1.4}$$

It can be inferred from *Eqns* (1.3) and (1.4) that both the specific useful work and the thermal efficiency of the Brayton cycle increase with a higher work extraction during the expansion process if the specific heat quantity q added remains constant. The expansion process, however, is bounded by two constraints:

1. The upper limit for the temperature at the beginning of the expansion process is determined by the thermal resilience of the turbine.
2. The final pressure of the expansion process corresponds to the pressure at the turbine outlet.

Since the extractable expansion work is largely dependent upon the pressure difference between the beginning and the end of the expansion process, two parameters can be manipulated to increase the expansion work:

1. It is possible to increase the pressure ratio of the compression. This allows the maximum turbine entry temperature to be reached at a higher pressure. This, however, necessitates additional compression work which, if the pressure ratio is increased beyond the optimum, results in a decrease in useful work.
2. The final pressure of the expansion can be reduced. Because the static pressure at the gas-turbine exhaust is determined by the ambient static pressure, a component which increases the static pressure of the turbine outflow before it reaches the exhaust becomes necessary: the diffuser. Since the diffuser is a passive component which

converts the kinetic-energy density of the turbine outflow into pressure, it does not introduce additional work and, thus, does not impact the useful work directly.

It can be concluded from the above elaborations that it is desirable to maximise the static-pressure rise in diffusers.

1.2. Diffuser types

Most diffusers can be assigned to one of the following four main classes: planar (two-dimensional), rectangular, conical, and annular. Annular diffusers can be further classified depending upon their hub and casing divergence (or convergence) angle. This work is focused on annular diffusers with diverging casing walls and cylindrical hub walls.

1.3. Diffuser flows

It is the function of a diffuser to convert the kinetic-energy density of a flow into static pressure, i.e., to decelerate the flow. The following is assumed, unless stated otherwise:

Assumption 1.1. The flow is *steady*, i.e., the flow quantities do not change over time:

$$\frac{\partial \boxtimes}{\partial t} = 0. \tag{1.5}$$

Assumption 1.2. The density ρ of the fluid is not dependent upon its pressure, i.e., the flow is *incompressible*[*] and, therefore,

$$\boldsymbol{\nabla} \cdot \mathbf{u} = 0. \tag{1.6}$$

Assumption 1.3. The density ρ of the fluid is uniform:

$$\boldsymbol{\nabla} \rho = 0. \tag{1.7}$$

Assumption 1.4. The fluid does not transport momentum normal to the flow direction, i.e., it is *inviscid:*

$$\mu = 0. \tag{1.8}$$

Implication 1.1. *Assumption* 1.4 implies that the flow velocity at the wall does not equal zero, i.e., the no-slip condition is not fulfilled.

Assumption 1.5. The flow is *irrotational* (the concept of rotation is explained in *Sec.* 3.4), i.e.,

$$\boldsymbol{\nabla} \times \mathbf{u} = 0. \tag{1.9}$$

Assumption 1.6. The heat fluxes across the diffuser walls equal zero, i.e., the walls are *adiabatic.* Likewise, there are no thermal inhomogeneities at the inlet.

Implication 1.2. Due to *Ass.* 1.6, the total enthalpy is constant and the flow is *isoenergetic:*

$$\boldsymbol{\nabla} h_{\text{tot}} = 0. \tag{1.10}$$

---

[*] and, by extension, subsonic

Implication 1.3. Crocco (1937) showed that for an inviscid, incompressible flow

$$T\boldsymbol{\nabla}s = (\boldsymbol{\nabla} \times \mathbf{u}) \times \mathbf{u} + \boldsymbol{\nabla}h_{\text{tot}}. \tag{1.11}$$

Therefore, *Ass.* 1.5 (irrotational flow) and *Imp.* 1.2 (isoenergetic flow) imply an *isentropic flow:*

$$\boldsymbol{\nabla}s = 0. \tag{1.12}$$

Since the flow considered is isentropic, the total pressure does not change between the inlet and outlet of the diffuser. It can be seen from Bernoulli's equation that a deceleration of the flow in the diffuser raises the static pressure:

$$p_{\text{tot}} = p + p_{\text{dyn}} = p + \frac{\rho}{2}u^2 = \text{const.} \tag{1.13}$$

For a subsonic flow, which is implied by *Ass.* 1.2 above, deceleration implies an increase in the cross-sectional area in the stream-wise direction in order to satisfy the conservation of mass, i.e.,

$$\rho u A = \text{const.} \tag{1.14}$$

Area ratio
The ratio of the inlet and outlet areas of the diffuser necessary to achieve a certain deceleration, and consequently, a certain static-pressure rise of the flow can be represented by the *area ratio,*

$$\mathfrak{A} := \frac{A_{\text{out}}}{A_{\text{in}}}. \tag{1.15}$$

It follows from (1.14) that the resulting velocity ratio is the inverse of the area ratio:

$$\frac{u_{\text{out}}}{u_{\text{in}}} = \frac{1}{\mathfrak{A}}. \tag{1.16}$$

Static-pressure recovery
The static-pressure rise, or *static-pressure recovery,* in a diffuser is defined as the difference between the static pressures at the inlet and outlet of the diffuser:

$$\Delta p := p_{\text{out}} - p_{\text{in}}. \tag{1.17}$$

To compare the static-pressure recovery of different diffuser flows at different pressure levels, the static-pressure rise can be non-dimensionalised with the dynamic pressure at the diffuser inlet:

$$c_p := \frac{p_{\text{out}} - p_{\text{in}}}{p_{\text{dyn,in}}}. \tag{1.18}$$

Using the relationship given in *Eqn.* (1.13) and $p_{\text{tot,in}} = p_{\text{tot,out}}$, the above equation can be rewritten to yield

$$c_p = \frac{\left(p_{\text{tot,out}} - p_{\text{dyn,out}}\right) - \left(p_{\text{tot,in}} - p_{\text{dyn,in}}\right)}{p_{\text{dyn,in}}} = 1 - \frac{u_{\text{out}}^2}{u_{\text{in}}^2}. \tag{1.19}$$

Together with *Eqn.* (1.16), the *ideal static-pressure recovery coefficient* $c_{p,\mathrm{id}}$ is then defined as

$$c_{p,\mathrm{id}} := 1 - \frac{1}{\mathfrak{A}^2}. \tag{1.20}$$

This coefficient quantifies the static-pressure recovery in an ideal, inviscid diffuser with axial inflow and depends solely upon the area ratio. When *inlet swirl*[*], that is, an inflow with a circumferential component, is to be considered, the deceleration due to the conservation of angular momentum has to be taken into account as well. The ideal static-pressure recovery coefficient may then be defined as:

$$c_{p,\mathrm{id}} := 1 - \frac{{}^{1}\!/_{\mathfrak{A}^2} + \tan^2(\alpha)\left(\frac{r_{\mathrm{Euler,in}}}{r_{\mathrm{Euler,out}}}\right)^2}{1 + \tan^2(\alpha)} \tag{1.21}$$

where the inlet swirl angle

$$\alpha := \arctan\left(\frac{u_{\theta,\mathrm{in}}}{u_{x,\mathrm{in}}}\right) \tag{1.22}$$

is calculated at the Euler radius which is defined as the radius which evenly divides the inner and the outer cross-sectional area, i.e.,

$$r_{\mathrm{Euler}} := \sqrt{\frac{r_{\mathrm{hub}}^2 + r_{\mathrm{cas}}^2}{2}} \tag{1.23}$$

with the subscripts "hub" and "cas" indicating the hub and casing, respectively.

Residual dynamic pressure

Equations (1.20) and (1.21) indicate that complete static-pressure recovery—or complete deceleration of the flow—meaning that the entire inlet dynamic pressure is converted into a static-pressure rise, requires an infinite area ratio. Conversely, a diffuser flow with a finite area ratio will always see a *residual dynamic pressure*

$$p_{\mathrm{dyn,out}} > 0. \tag{1.24}$$

Using a non-dimensional formulation, the *dynamic-pressure coefficient* is obtained:

$$\xi := \frac{p_{\mathrm{dyn,out}}}{p_{\mathrm{dyn,in}}}. \tag{1.25}$$

1.4. Viscous effects

The flow problem becomes disparately more complicated if viscous effects are to be included. By waiving the assumption of an inviscid flow (*Ass.* 1.4), neighbouring streamlines are now exchanging momentum normal to the flow direction via shear stresses. *Implication* 1.1 is no longer valid and a *no-slip* boundary condition must be assumed at the wall: the wall-parallel flow velocity at the wall now equals zero. The wall-normal momentum exchange due to viscous shear stresses leads to the formation of *boundary layers* at the diffuser walls. Their

---

[*] The term *whirl* is also found in some older references.

velocity profiles assume a wall-parallel velocity of zero at the wall and free-stream velocity at a sufficient distance from the wall.

It can be shown that such a velocity profile does not fulfil *Eqn.* (1.9): boundary layers are rotational flow regions (see *Ass.* 1.5). It follows from this and *Eqn.* (1.11) that the flow is no longer isentropic in the rotational regions and *Imp.* 1.3 is no longer valid. Hence, kinetic flow energy is dissipated into heat in the boundary layers.

Total-pressure losses

The dissipation of kinetic energy manifests itself in a *total-pressure loss,*

$$\Delta p_{\mathrm{tot}} := p_{\mathrm{tot,in}} - p_{\mathrm{tot,out}} > 0, \tag{1.26}$$

or expressed in non-dimensional form as the total-pressure loss coefficient:

$$\zeta := \frac{p_{\mathrm{tot,in}} - p_{\mathrm{tot,out}}}{p_{\mathrm{dyn,in}}}. \tag{1.27}$$

It follows from the definitions of c_p, ζ, and ξ given in *Eqns* (1.18), (1.27), and (1.25) that

$$c_p + \zeta + \xi \equiv 1. \tag{1.28}$$

Generally, it can be expected that increased total-pressure losses are linked to a decrease in static-pressure recovery.

1.4.1. Boundary layers

The exact values of the real static-pressure recovery coefficient depend upon the total-pressure losses generated in the boundary layers. It is, thus, not surprising that their prediction is anything but trivial. Nevertheless, several inferences can be drawn from a simple description of the characteristic boundary layer parameters. A detailed introduction will be given in *Sec.* 3.3.

The first parameter which comes to mind when trying to describe a boundary layer is its *thickness.* The boundary-layer thickness δ is not rigidly quantifiable because the boundary-layer velocity profile approaches the free-stream velocity asymptotically. It has, however, proven to be practical to define the boundary-layer edge as the streamline where 99 % of the free-stream velocity is attained; the wall-normal distance between the wall and the streamline with $u = 0.99\,\mathcal{U}_\infty$ is termed δ_{99}.

Two, more physically motivated, properties are the *displacement thickness* δ^* and *momentum thickness* ϑ, which can be derived from the respective conservation laws of mass and momentum.

The displacement thickness δ^* follows from the velocity-deficit distribution $\mathcal{U}_\infty - u$ in the boundary layer. It labels the hypothetical distance by which the flow boundary would have to be displaced in an inviscid flow in order to achieve the same reduction in mass flow rate caused by the integrated velocity-deficit distribution of the boundary layer:

$$\delta^*\,\mathcal{U}_\infty = \int_0^\delta (\,\mathcal{U}_\infty - u\,)\,\mathrm{d}x_2. \tag{1.29}$$

Likewise, the momentum thickness ϑ labels the hypothetical distance by which the flow boundary would have to be displaced in an inviscid flow to achieve the same reduction in momentum-flux caused by the boundary layer:

$$\vartheta\, U_\infty^2 = \int_0^\delta u \,(U_\infty - u)\, \mathrm{d}x_2. \tag{1.30}$$

Effective static-pressure recovery

The displacement thickness allows relating a viscous flow problem to an equivalent inviscid flow problem. It can be used to formulate an effective area ratio for a viscous diffuser flow,

$$\mathfrak{A}_{\mathrm{eff}} := \frac{A_{\mathrm{out,eff}}}{A_{\mathrm{in,eff}}} \tag{1.31}$$

where the effective area ratio is a ratio of the effective inlet and outlet areas; an effective area is defined as the difference between the actual cross-sectional area of the diffuser and the area blocked by the displacement thickness, i.e., A_{δ^*}:

$$A_{\mathrm{eff}} := A - A_{\delta^*}. \tag{1.32}$$

By inserting the effective area ratio into the definition of the ideal static-pressure recovery coefficient given in *Eqn.* (1.20), the *effective static-pressure recovery coefficient*, i.e., the static-pressure recovery achieved in the diffuser with boundary layers may be written as:

$$c_{p,\mathrm{eff}} = 1 - \frac{1}{\mathfrak{A}_{\mathrm{eff}}^2}. \tag{1.33}$$

The term *effective static-pressure recovery* is used here, rather than *real static-pressure recovery*, to emphasise that it is based upon simplified descriptions of the boundary layers.

To quantify how well a diffuser with boundary layers performs in comparison to its ideal counterpart, the *diffuser effectiveness* is introduced, i.e.,

$$\epsilon := \frac{c_{p,\mathrm{eff}}}{c_{p,\mathrm{id}}}, \tag{1.34}$$

or, expressed more generally with regard to real diffuser flows,

$$\epsilon := \frac{c_p}{c_{p,\mathrm{id}}}. \tag{1.35}$$

The diffuser effectiveness is generally below unity. Exceptions to this can arise when the dissipation of sufficiently strong inflow inhomogeneities raises the thermal energy and, thereby, static pressure of the flow. This is presumably mostly the case for area ratios close to unity where this effect would be the predominant cause of the static-pressure rise. According to FLEIGE (2002), *tailpipes*[*] downstream of diffusers with strong outflow inhomogeneities are employed to realise a residual static-pressure recovery based upon this effect.

---

[*] Duct sections of constant cross-sectional area

Momentum losses
The momentum deficit in the boundary layers determines the total-pressure loss of the diffuser if the boundary layers are the only loss-generating mechanisms present. Thus, a greater increase in momentum thickness along the diffuser results in higher total-pressure losses.

1.4.2. Boundary-layer separation

Boundary layers tend to have the strongest impact upon diffuser performance when they separate. Flow separation occurs under adverse pressure gradients because the low-momentum fluid adjacent to the wall reacts more sensitively to the pressure rise. Experiencing deceleration, the boundary-layer velocity profile develops an inflection point at the wall where the wall shear stress is zero and which demarcates the region of separated flow. Upon further deceleration, the boundary layer exhibits regions of *reversed flow* and, on a greater scale, *recirculation zones.* Both displacement thickness and momentum thickness increase drastically downstream of the separation point.

It is a common observation that the shape of boundary-layer velocity profiles is a good predictor for the likelihood of separation. A widely used parameter to describe the shape is the ratio of the displacement thickness to the momentum thickness, i.e., the *boundary-layer shape factor,*

$$H := \frac{\delta^*}{\vartheta}, \tag{1.36}$$

Gruschwitz (1931) reported separation of strictly turbulent boundary layers shortly after H reaches approximately 1.85; von Doehnhoff and Tetervin (1943) observed that flow separation never occurs for $H < 1.8$ and definitely happens when $H > 2.6$. Senoo and Nishi (1977b) argued that most H-based separation criteria are valid only for external flows. For internal flows, however, they postulated that boundary layers can stay attached at considerably higher shape-factor values. They attributed this effect to blockage of the duct due to boundary layers and provided the following *separation relationship:*

$$H_{\text{sep}} = 1.8 + 3.75 B_{\text{sep}} \tag{1.37}$$

where the subscript "sep" denotes values at the separation point and where the authors defined the blockage B as the ratio of the total displacement to the diffuser width $\mathcal{W}$,

$$B := \frac{2\delta^*}{\mathcal{W}}, \tag{1.38}$$

for planar diffusers and the ratio of the total displacement to the diffuser radius,

$$B := \frac{2\delta^*}{r}, \tag{1.39}$$

for conical diffusers. Even though these separation criteria differ substantially, they all indicate that a reduction of the shape factor—and, consequently, of the displacement thickness relative to the momentum thickness—is beneficial to avoid separation.

1.5. Derived objectives

Two main objectives for the design of diffusers can be derived from the above discussion.

1. Increase static-pressure recovery.
2. Reduce total-pressure losses.

Both objectives require the reduction of the boundary-layer displacement thickness in the diffuser in order to prevent or delay separation and, in the case of attached boundary layers, increase the effective area ratio.

This would favour long diffusers with a low aerodynamic loading, i.e., shallow opening angles. However, a third objective is mentioned by Fleige (2002): when considering gas-turbine power plants, longer diffusers lead to increased investment cost for the surrounding facility as well as for the diffuser itself if the generator is located upstream of the compressor. In the case where the generator is located downstream of the diffuser, additional vibrational problems can arise due to the need for a longer shaft.

It becomes, thus, a third objective to minimise the diffuser length. This can only be realised by increasing the aerodynamic loading and designing aggressive diffuser geometries with steep opening angles. These seemingly conflicting goals motivate a thorough investigation of opportunities for increasing the resilience of diffusers against flow separation.

In the context of the present work, the improvement in diffuser performance, i.e., the increase in static-pressure recovery and decrease in total-pressure losses by means of reducing the boundary-layer displacement thickness and, by extension, delaying or preventing flow separation will be referred to as *diffuser stabilisation;* the physical process by which this is achieved will be referred to as *boundary-layer stabilisation* while the capacity of the boundary layer to yield an improved diffuser performance will be referred to as *boundary-layer stability.* It should be noted that the terms *stability* and *stabilisation* are often used in the context of boundary-layer transition from laminar to turbulent as well as the suppression of such boundary-layer transition; this use, however, is precluded in the present work to avoid possible ambiguities.

Chapter 2.

Literature

It is the aim of this chapter to review how the stabilisation of diffuser flows has been approached in past research and to identify how the present work can be integrated into the body of literature.

Investigations into diffusers were reported as early as 1797 by Venturi (Venturi 1797). The first systematic studies of pressure losses in diffusing water pipes were performed by Andres (1909)* and Gibson (1910). Patterson (1938) reviewed data from literature and provided an extensive analysis of diffuser efficiencies depending upon swirl and flow uniformity as well as geometric parameters, which would serve as a standard reference for a long time.

Similarly, Bardili et al. (1939) provided a series of empirical diffuser design charts which can be regarded as early predecessors of the well-known design charts by Reneau et al. (1967) as well as Sovran and Klomp (1967). The extensive experimental studies of Sovran and Klomp (1967), which considered a multitude of diffuser geometries, were later compiled together with additional corrections for real diffuser flows, e.g., in ESDU (1977).

2.1. Empirical studies

2.1.1. Boundary layers

Reneau et al. (1967) found a decrease in static-pressure recovery for an increasing displacement thickness at the diffuser inlet. Sovran and Klomp (1967) confirmed these observations for conical diffusers. While they did not consider variations in the inlet displacement thickness for annular diffusers, similar studies were conducted by Howard et al. (1967) for fully developed turbulent boundary layers

2.1.2. Turbulence

Using arrays of rods, round in cross section, located upstream of a planar diffuser, Hoffmann (1981) and Hoffmann and Gonzalez (1984) were able to increase the static-pressure recovery by increasing the free-stream turbulence intensity and, thereby, enhancing mixing between the free stream and boundary layers.

Interestingly, they noted an influence of the rod orientation as well as turbulence intensity and length scale. The improvements were most significant when the rods—and, therefore, the principal rotational axes of the turbulent structures—were oriented normal to the flow direction and parallel to the diverging wall, as shown in *Fig.* 2.1. They reported significant improvements for turbulence intensities greater than 3.5 % and integral turbulence length

---

*The experiments were conducted at the University of Hanover.

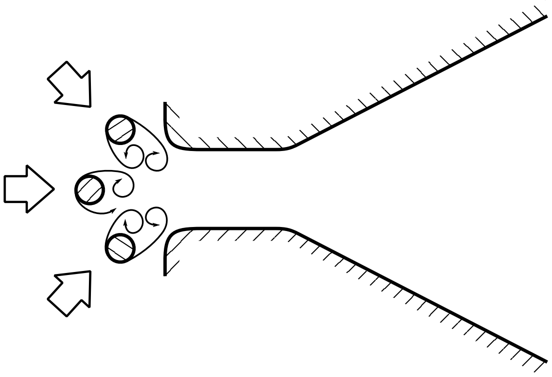

Figure 2.1.: Diffuser with upstream turbulence grid: experimental configuration used by Hoffmann (1981) and (with five rods) by Hoffmann and Gonzalez (1984)

scales of at least 7.2 times the boundary-layer displacement thickness. These results suggest that, for the purpose of diffuser stabilisation, well-oriented large-scale vortical structures are to be favoured over small-scale more isotropic turbulence.

2.1.3. Swirl

Lohmann et al. (1979) showed that, for annular diffusers with conical walls of various divergence angles, inlet swirl leads to an increase in the turbulent kinetic energy at the casing walls, whereas the turbulent kinetic energy decreased at the hub walls. As a result, the hub boundary layer becomes less resilient against flow separation. The converse can be said for the casing boundary layer. Overall, the authors noted a decrease in diffuser performance when inlet swirl is present. These changes in turbulent kinetic energy are commonly observed along curved streamlines where Coriolis forces impact the production and decay of turbulence (Kožulović and Röber 2006).

Later, Fleige and Riess (2001), Vassiliev et al. (2003), and Vassiliev et al. (2011) studied the impact of inlet swirl on the performance of annular diffusers. The studies agreed in showing that moderate swirl angles are able to reduce or prevent boundary-layer separation at the diffuser casing and, thereby, increase the static-pressure recovery. The investigations revealed, however, an increase in separation at the diffuser hub and a decrease in static-pressure recovery. These results confirmed the earlier findings of Hoadley (1970).

2.1.4. Turbine outflow

In the case where a diffuser is located downstream of a turbine stage, it experiences the inflow variations mentioned previously in this chapter. Additionally, the diffuser is subjected to inhomogeneities and a high degree of unsteadiness: this expands the parameter space which can be explored to a considerable degree.

Kluss et al. (2009) simulated an annular diffuser with a subsequent conical diffuser downstream of a spoked-wheel rotor and obtained a static-pressure recovery higher than predicted by common diffuser design charts. Drechsel et al. (2015) simulated the same annular diffuser downstream of a rotor equipped with symmetric NACA-0020 blades and obtained results consistent with Kluss et al. (2009). This indicates that some structures in the turbine outflow act on the diffuser boundary layer in a stabilising manner.

Experiments conducted by Sieker (2010)* and Kuschel (2014)† confirmed the results of the numerical simulations. The experiments featured the same configuration as the annular diffuser and rotor used in this work. The rotor was equipped with either cylindrical spokes or symmetric NACA-0020 blades. The annular diffusers featured half-opening angles of 15° and 20°. For both rotors and both diffusers, significant increases in static-pressure recovery could be achieved. These increases varied with the rotor operating point, which is a clear indicator of the involvement of secondary-flow structures in the stabilisation process.

Mimic et al. (2018a) identified the velocity field induced by the tip-leakage vortices as a central aspect of the stabilisation process.

2.2. Separation-prevention methods

Having discussed the predominant influences which contribute to deviations of diffuser performance from an idealised state, the focus will be placed on select examples of methods which deliberately control the diffuser flow in a beneficial way, before finally moving on to methods for predicting the diffuser performance accurately.

Moore and Kline (1958) and Cochran and Kline (1958) visualised the flow-separation structures emerging in planar diffusers with varying opening angles. The authors provided a comprehensive analysis of the transition process from fully attached to fully separated diffuser flows. The data show that—adopting the terminology introduced by Cochran and Kline (1958)—the process begins with the occurrence of asymmetric, *intermittent transitory separation* regions on one of the two diverging walls, while the flow remains quite steady. As intermittent transitory flow separation forms on the opposite wall, the unsteadiness of the flow increases until one wall reaches *transitory flow separation*, characterised by moving separation cores and three-dimensional flow. At this point, the flow is subjected to strong pulsations. After further increase of the opening angle, the steadiness of the flow increases again until one diffuser wall exhibits rather stable flow separation while the other wall experiences fully attached flow. The flow was reported to be very steady.

Building upon these results, Cochran and Kline (1958) inserted *splitter vanes* into the inlet section of a planar diffuser. They were able to reduce flow separation and increase static-pressure recovery tremendously, even at steeper opening angles. Senoo and Nishi (1977b) commented on this; the authors conjectured that the increase in blockage caused by the additional boundary layers on the splitter vanes leads to a stabilisation as expressed in their empirically derived separation relationship (see *Eqn.* 1.37).

Vortex generators represent another class of separation-preventing or reducing devices. The physical mechanism by which they act shares some similarities with the turbine–diffuser interaction measured by Sieker (2010)* and Kuschel (2014)† as well as with the rod-induced stabilisation described by Hoffmann (1981) and Hoffmann and Gonzalez (1984), in the sense that they cause the formation and shedding of vortical or turbulent structures. This, in turn, promotes the exchange of fluid and momentum between the free stream and boundary layer. Based upon this effect, improvements in diffuser performance were achieved by

---

[*] for preliminary results, see also Sieker and Seume (2008a) and Sieker and Seume (2008b)

[†] see also Kuschel et al. (2015)

using vortex generators, e.g., by Brown et al. (1968) and Senoo and Nishi (1974). It is noteworthy that Brown et al. (1968) observed a distinct dependency of the benefit of vortex generators upon their positioning and orientation, with some cases even impeding diffuser performance. This dependency is consistent with the influence of turbulence directionality seen by Hoffmann (1981).

The injection of fluid into the casing boundary layer at the diffuser inlet was investigated by Babu et al. (2011), who found that the overall effect of this active flow-control method was positive. Similarly, Thomas et al. (2015) performed detailed measurements in an annular and subsequent conical diffuser where they injected fluid into the casing boundary layer to emulate strong tip-leakage flow—a so-called *tip jet*. Their experimental set-up allowed the variation of the injection mass-flow fraction and injection slot height*, effecting variable injected mass flow and jet velocity. The static-pressure recovery increased after exceeding a certain minimum injection rate. After further increase of the injection rate, this trend was reversed, as more and more fluid was entrained from the free-stream into the casing boundary layer, ultimately causing separation at the hub.

2.3. Concurrent design of turbine and diffuser

Another conceptually more holistic approach to improving diffuser performance is the *concurrent* or *combined design of turbine and diffuser.* Unlike the methods presented in the previous section, this approach does not require any additional devices or moving components. As discussed in *Sec.* 2.1, the inflow conditions experienced by the diffuser can impact its performance tremendously. It is, therefore, logical to investigate methodologies for the design of turbines that generate an outflow which benefits the diffuser.

Quest and Scholz (1980) conducted extensive experimental studies on annular diffusers with divergent casing walls and parallel hub walls downstream of a turbine. They reported an optimum tip gap which, while reducing the turbine efficiency, increases the overall system efficiency. They noted, however, that certain combinations of turbine-outflow swirl and strut orientation may increase losses.

Farokhi (1987) presented a simplified thermodynamic analysis of the turbine–diffuser system. His calculations yielded a possible increase in turbine power output for larger tip gaps, however, at the expense of a reduced system efficiency. Zimmerman and Stetter (1993) arrived at similar conclusions when interpreting their experimental data. Willinger and Haselbacher (1998), however, found virtually no dependency between tip gap and system efficiency.

Mihailowitsch et al. (2018) compared different shroud seal gaps in their numerical analysis of a turbine–diffuser system with a shrouded rotor. The authors found an adverse effect of the gap size on the diffuser performance. This was partially due to changes in incidence on the subsequent struts. They noted, however, a current trend towards more compact gas turbines with consequently shorter diffusers and acknowledged that larger gaps could be beneficial in such configurations.

---

*in analogy to a tip-gap variation

2.4. Diffuser-performance prediction

Great attention should be paid to the prediction of diffuser performance. Due to the occurrence of flow separations and the ensuing highly three-dimensional flow conditions, this task is certainly not trivial. The diffuser design charts introduced at the beginning of this chapter and the quantification of inflow-related deviations from an idealised diffuser flow can be regarded as a form of diffuser-performance prediction. Their heuristic nature, however, usually confines their applicability to a rather limited class of cases.

Senoo and Nishi (1977a) and Senoo and Nishi (1977b) devised an algorithm for the calculation of boundary-layer parameters and static-pressure recovery in diffusers, using an integral form of the boundary-layer momentum equation and a correlation-based approach to evaluate the shape factor H. In connection with their empirically derived separation relationship (see *Eqn.* 1.37), they were among the first to successfully calculate the behaviour of real diffuser flows—even downstream of the separation onset. Bardina et al. (1982), however, referred to this approach as "postdictive" in order to emphasise its heavy reliance upon measurement data.

Building upon the work of Kline (1978), Bardina et al. (1982) implemented a *zonal method* where the flow is subdivided into two "zones" or "modules"[*]: free stream and boundary layer. The exchange of mass and momentum between the two is captured in a system of two ordinary differential equations, which will be discussed in *Sec.* 3.3.5. The equations for the conservation of both mass and momentum are based upon wall-normal integrals of the boundary-layer flow quantities. The correlations employed in the calculation process are derived from the generalised, non-dimensional boundary-layer profiles of Coles (1956) and Coles (1962) as well as the entrainment relationship of Head (1958). Using this approach, Bardina et al. (1982) were able to successfully predict boundary-layer parameters and static-pressure recovery for a multitude of planar diffusers and some annular diffusers. Childs (1981) integrated compressibility effects into the approach and Lyrio et al. (1981) adapted the method to cover unsteady free-stream flow. A detailed overview of these and further associated developments is given by Johnston (1998).

2.5. Prediction of turbine–diffuser interaction

The inclusion of unsteady free-stream flow by Lyrio et al. (1981) can be seen as a first step towards the prediction of the behaviour of turbine–diffuser systems.

The work of Kuschel (2014)[†] revealed a correlation between *apparent stresses*—i.e., Reynolds stresses caused by highly unsteady vortical flow conditions measured just downstream of the rotor near the tip—with a dominant radial component and the static-pressure recovery coefficient of the annular diffuser. Again, some similarity to the work of Hoffmann (1981) can be inferred, who noted the importance of the orientation of the vortical flow structures.

Drechsel et al. (2015) were able to reproduce these results numerically. However, this was only possible to a sufficient accuracy by applying the partially scale-resolving *scale-adaptive simulation* (*SAS*) approach by Menter and Egorov (2010). Drechsel et al. (2016) demonstrated in a comparative study between conventional unsteady Reynolds-averaged

---

[*] or conceptual objects, to continue the wording introduced initially

[†] see also Kuschel et al. (2015)

Navier–Stokes (URANS) simulations, SAS, and hot-wire measurements that URANS failed to render the unsteady vortical structures in the tip region accurately.

For the first time, Mimic et al. (2018a) formulated a non-dimensional number from integral stage-design parameters with the aim of predicting the influence of the turbine outflow on the static-pressure recovery in annular diffusers. The authors found a linear correlation between their newly defined *stabilisation number* and the diffuser effectiveness using experimental data from Kuschel (2014)*, additional measurements from the same diffuser test rig, and a computational flow model using the SAS approach.

Mimic et al. (2018b) found a linear correlation between the stabilisation number, multiplied by a second non-dimensional number calculated from integral stage data, and the total-pressure losses generated in the diffuser. Again, both experimental and numerical data were used for this correlation.

Mimic et al. (2018c) were able to expand the static-pressure recovery correlation to several other diffuser half-opening angles, although most of the newly added diffusers were only investigated numerically. Finally, Mimic et al. (2019) expanded the total-pressure loss correlation to other diffuser half-opening angles.

2.6. Subsumption of the present work

The preceding sections give an overview of previous diffuser research relevant to this work. The content of this work, especially the stabilisation number and its correlation with the static-pressure recovery and total-pressure losses, is closely related to the publications by Mimic et al. (2018a), Mimic et al. (2018b), Mimic et al. (2018c), and Mimic et al. (2019). In the present work, however, the stabilisation number is derived with greater rigour. Several improvements have also been incorporated into the approach.

Additionally, the method of Bardina et al. (1982) has been implemented and extended to predict the vortex-induced boundary-layer stabilisation. It is shown that the stabilising vortices are modelled consistently with the definition of the stabilisation number.

The literature suggests that both the vortex–boundary-layer prediction method and the correlation-based approach using the stabilisation number are novel.

---

*see also Kuschel et al. (2015)

Chapter 3.

Fundamentals

This chapter presents a review of the fluid-mechanical fundamentals necessary to develop a coherent theory about the *turbine–diffuser interaction*, starting from first principles and moving on to specific applications of these principles.

3.1. Continuum flows

Real fluids consist of molecules or atoms, in short *fluid particles*, which interact with each other by exchanging momentum through different forces. While it is possible to derive and solve the equations of motion for such a system, the sheer number of fluid particles (approximately 2.7×10^{16} particles per mm^3 for a gas under standard conditions), it is certainly not trivial for most flows considered in engineering. With certain assumptions, however, it is possible to simplify the problem (Schlichting and Gersten 2006).

Assumption 3.1. The characteristic length scale of the flow problem considered is much larger than the mean free path between fluid particles.

Implication 3.1. It follows from *Ass.* 3.1 that the fluid can be modelled as a continuum, i.e., a material with a continuous distribution of mass, momentum, and energy.

Assumption 3.2. The torque acting upon a fluid element is not dependent upon its volume.

Implication 3.2. *Assumption* 3.2 implies that no electro- or magnetodynamic forces arise in the fluid.

Assumption 3.3. The principal directions of the stresses and strains arising in the fluid are aligned, i.e., the fluid is considered *isotropic.*

Assumption 3.4. The stresses arising in the fluid are related linearly to the strains, i.e., it is a *Newtonian fluid.* The proportionality factor is the molecular viscosity.

Assumption 3.5. Internal relaxation processes in the fluid happen on a significantly shorter time scale than deformation processes.

Assumption 3.6. Thermodynamic state equations are independent from local or temporal gradients, i.e., they are the same as in a resting system.

Assumption 3.7. The flow exhibits a single phase. Hence, the thermodynamic state of the fluid can be described using only two state variables (e.g., static pressure and temperature).

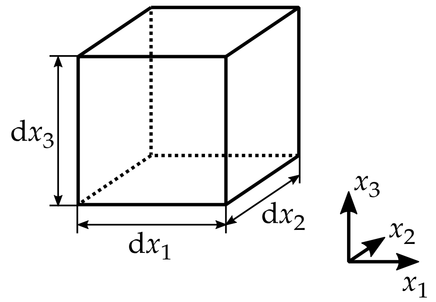

Figure 3.1.: Infinitesimal fluid element

Assumption 3.8. Heat fluxes in the fluid are related linearly to temperature gradients. The proportionality factor is the thermal conductivity.

Assumption 3.9. There are no heat sources in the fluid, such as, e.g., nuclear decay or chemical reactions.

Following these assumptions, it is necessary to derive equations for the distribution of mass, momenta in three spatial dimensions, and internal energy in order to describe the behaviour of the flow, giving a total of five equations. As will be shown in the following sections, two further variables are involved: pressure and temperature. It will, therefore, be necessary to provide two thermodynamic state equations to close the system. To establish these fundamental relationships, an infinitesimal fluid element, as shown in *Fig.* 3.1, is considered.

3.1.1. Continuity equation

The temporal rate of change of the mass contained in the fluid element is determined by the integral of the rate of change in fluid mass density ρ over the element volume $\mathcal{V}$:

$$\frac{\mathrm{D}m}{\mathrm{D}t} = \iiint_{\mathcal{V}} \frac{\mathrm{D}\rho}{\mathrm{D}t} \mathrm{d}V. \tag{3.1}$$

The *material derivative* $\mathrm{D}\boxtimes/\mathrm{D}t$ describes the overall temporal rate of change of a physical quantity in any fluid element and can be separated into

$$\frac{\mathrm{D}\rho}{\mathrm{D}t} := \frac{\partial\rho}{\partial t} + \frac{\mathrm{d}\rho}{\mathrm{d}t} \tag{3.2}$$

where $\partial\rho/\partial t$ is the *local derivative* which describes changes due to inherent unsteadiness in the flow field and where $\mathrm{d}\rho/\mathrm{d}t$ is the *advective* or *convective derivative* which represents the advective transport of a physical quantity—here the density—into and out of the fluid element. The advective derivative can, therefore, be expressed as

$$\frac{\mathrm{d}\rho}{\mathrm{d}t} = \mathbf{u} \cdot \boldsymbol{\nabla}\rho. \tag{3.3}$$

The overall rate of change of the density, as quantified by the material derivative, is determined by the presence of *sources* or *sinks* in the fluid element. These sources and sinks are given by the *divergence* $\boldsymbol{\nabla} \cdot \mathbf{u}$ of the velocity field: sources imply $\boldsymbol{\nabla} \cdot \mathbf{u} > 0$ and are seen as diverging streamlines leading to a reduction in fluid density, whereas sinks imply $\boldsymbol{\nabla} \cdot \mathbf{u} < 0$ and are seen as converging streamlines corresponding to an increase in density. This can be written as

$$\boxed{\frac{\mathrm{D}\rho}{\mathrm{D}t} + \rho\,\boldsymbol{\nabla} \cdot \mathbf{u} = 0,} \tag{3.4}$$

which is the *continuity equation for compressible flows* and describes the conservation of mass. The use of the qualifier "compressible" implies that there is also an incompressible form of the equation. In an incompressible flow, the density of a fluid element does not change during its movement along a streamline, i.e., its material derivative vanishes:

$$\frac{\mathrm{D}\rho}{\mathrm{D}t} = 0. \tag{3.5}$$

Therefore, the *continuity equation for incompressible flows* becomes

$$\boldsymbol{\nabla} \cdot \mathbf{u} = 0. \tag{3.6}$$

3.1.2. Momentum equations

In a similar way to the temporal rate of change of the mass, the temporal rate of change of the momentum carried by the fluid element can be formulated as the sum of all forces acting upon the element. Distinguishing between volume-specific *volume forces* and volume-specific surface *forcers*, this may be written as

$$\frac{\mathrm{D}\mathbf{J}}{\mathrm{D}t} = \iiint_{\mho} \rho \frac{\mathrm{D}\mathbf{u}}{\mathrm{D}t} \mathrm{d}V = \iiint_{\mho} \mathbf{f}_S \mathrm{d}V + \iiint_{\mho} \mathbf{f}_V \mathrm{d}V. \tag{3.7}$$

The term $\mathbf{f}_V\,\mathrm{d}V$ refers to the volume-specific forces acting upon the entire volume of the fluid element, e.g., gravitation or fictitious forces when an accelerated frame of reference is considered, whereas $\mathbf{f}_S\,\mathrm{d}V$ describe the volume-specific surface forces.

The surface forces are caused by stresses acting upon the surface of the fluid element which are expressed by the Cauchy stress tensor,

$$\boldsymbol{\sigma} := \begin{pmatrix} \sigma_1 & \tau_{12} & \tau_{13} \\ \tau_{21} & \sigma_2 & \tau_{23} \\ \tau_{31} & \tau_{32} & \sigma_3 \end{pmatrix}, \tag{3.8}$$

where σ_i are the normal stresses and τ_{ij} are the shear stresses.

The Cauchy stress tensor is symmetric (see *Ass.* 3.3) and its use carries the implicit assumption that the shear-stress-induced torque imposed upon a fluid element does not depend upon its volume, as may be the case in electrostatic fields (Schlichting and Gersten 2006).

For most gases, the mechanical pressure can be defined as the *first invariant* of the stress tensor:

$$p := -\frac{\sigma_1 + \sigma_2 + \sigma_3}{3}. \tag{3.9}$$

The normal stresses in *Eqn.* (3.8) can then be decomposed into isotropic and deviatoric components, yielding the following decomposition of the Cauchy stress tensor:

$$\boldsymbol{\sigma} = \boldsymbol{\tau} - p\mathbf{I} \tag{3.10}$$

where $\mathbf{I}$ is the *identity matrix,*

$$\mathbf{I} := \begin{pmatrix} 1 & 0 & 0 \\ 0 & 1 & 0 \\ 0 & 0 & 1 \end{pmatrix}, \tag{3.11}$$

and $\boldsymbol{\tau}$ is the *deviatoric stress tensor,* i.e.,

$$\boldsymbol{\tau} := \begin{pmatrix} \tau_{11} & \tau_{12} & \tau_{13} \\ \tau_{21} & \tau_{22} & \tau_{23} \\ \tau_{31} & \tau_{32} & \tau_{33} \end{pmatrix}. \tag{3.12}$$

Note that the trace of the deviatoric stress tensor vanishes for incompressible flows (Schlichting and Gersten 2006).

Using the decomposition of the Cauchy stress tensor into an isotropic pressure and a deviatoric stress tensor, as shown in *Eqn.* (3.10), the *general continuum equation* can be derived from *Eqn.* (3.7):

$$\rho \frac{\mathrm{D}\mathbf{u}}{\mathrm{D}t} = -\boldsymbol{\nabla} p + \boldsymbol{\nabla} \cdot \boldsymbol{\tau} + \mathbf{f}_V. \tag{3.13}$$

In order to derive an equation for the motion of the fluid from the force equilibrium stated in the above equation, a nexus between the stresses and deformations acting upon the fluid element needs to be determined. The deformations can be expressed in terms of the *strain-rate tensor,*

$$\mathbf{S} := \begin{pmatrix} \frac{\partial u_1}{\partial x_1} & \frac{1}{2}\left(\frac{\partial u_2}{\partial x_1} + \frac{\partial u_1}{\partial x_2}\right) & \frac{1}{2}\left(\frac{\partial u_3}{\partial x_1} + \frac{\partial u_1}{\partial x_3}\right) \\ \frac{1}{2}\left(\frac{\partial u_1}{\partial x_2} + \frac{\partial u_2}{\partial x_1}\right) & \frac{\partial u_2}{\partial x_2} & \frac{1}{2}\left(\frac{\partial u_3}{\partial x_2} + \frac{\partial u_2}{\partial x_3}\right) \\ \frac{1}{2}\left(\frac{\partial u_1}{\partial x_3} + \frac{\partial u_3}{\partial x_1}\right) & \frac{1}{2}\left(\frac{\partial u_2}{\partial x_3} + \frac{\partial u_3}{\partial x_2}\right) & \frac{\partial u_3}{\partial x_3} \end{pmatrix}, \tag{3.14}$$

or, in brief,

$$\mathbf{S} := \frac{1}{2}\left[(\boldsymbol{\nabla} \otimes \mathbf{u}) + (\mathbf{u} \otimes \boldsymbol{\nabla})\right]. \tag{3.15}$$

Using the assumption of a Newtonian fluid (see *Ass.* 3.4), the deviatoric stresses can be expressed through linear functions of the strain rates,

$$\boldsymbol{\tau} = \lambda \operatorname{tr}(\mathbf{S})\, \mathbf{I} + 2\mu \mathbf{S}, \tag{3.16}$$

where $\operatorname{tr}(\mathbf{S}) = \boldsymbol{\nabla} \cdot \mathbf{u}$ denotes the trace of the strain-rate tensor and where λ is called the Lamé constant, which relates the normal stresses to a volume dilation. By invoking Stokes' hypothesis, i.e.,

$$3\lambda + 2\mu = 0, \tag{3.17}$$

the deviatoric stress tensor can be reformulated to yield

$$\boldsymbol{\tau} = -\frac{2}{3}\mu \operatorname{tr}(\mathbf{S})\, \mathbf{I} + 2\mu \mathbf{S}. \tag{3.18}$$

Using the *traceless strain-rate tensor*,

$$\mathbf{S}^{*} := \mathbf{S} - \frac{1}{3}\,\mathrm{tr}(\mathbf{S})\,\mathbf{I}, \tag{3.19}$$

the deviatoric stress tensor can be conveniently rewritten as

$$\boldsymbol{\tau} = 2\mu\mathbf{S}^{*} \tag{3.20}$$

with the associated Cauchy stress tensor given by

$$\sigma = -p\mathbf{I} + 2\mu\mathbf{S}. \tag{3.21}$$

Inserting *Eqn.* (3.20) into *Eqn.* (3.13) gives

$$\rho\frac{\mathrm{D}\mathbf{u}}{\mathrm{D}t} = -\boldsymbol{\nabla}p + \boldsymbol{\nabla}\cdot(2\mu\mathbf{S}^{*}) + \mathbf{f}_V \tag{3.22}$$

and, after substituting the traceless strain-rate tensor, yields the vector form of the Navier–Stokes equations for *compressible flows:*

$$\boxed{\rho\frac{\mathrm{D}\mathbf{u}}{\mathrm{D}t} = -\boldsymbol{\nabla}p + \mu\boldsymbol{\nabla}^2\mathbf{u} + \frac{1}{3}\mu\boldsymbol{\nabla}(\boldsymbol{\nabla}\cdot\mathbf{u}) + \mathbf{f}_V.} \tag{3.23}$$

Since $\boldsymbol{\nabla}\cdot\mathbf{u} = 0$ for incompressible flows, and assuming constant viscosity, it follows that

$$\rho\frac{\mathrm{D}\mathbf{u}}{\mathrm{D}t} = -\boldsymbol{\nabla}p + \mu\boldsymbol{\nabla}^2\mathbf{u} + \mathbf{f}_V, \tag{3.24}$$

which represents the Navier–Stokes equations for *incompressible flows* in their vector form.

3.1.3. Energy equation

The next step in determining the state of the fluid is to establish the distribution of the *internal energy* and, by extension, temperature. Considering the same infinitesimal fluid element as before, the *first law of thermodynamics* is applied, which states that the rate of change of the total energy in the fluid element is balanced by the sum of the heat flow across the boundaries and the work performed due to deformation of the element:

$$\frac{\mathrm{D}E_{\mathrm{tot}}}{\mathrm{D}t} = \dot{Q} + W \tag{3.25}$$

where the total energy is defined as the sum of the internal energy, kinetic energy and potential energy:

$$E_{\mathrm{tot}} := E + \frac{1}{2}\,m\,(\mathbf{u}\cdot\mathbf{u}) + \Phi. \tag{3.26}$$

Using specific quantities and omitting the infinitesimal volume $\mathrm{d}V$, *Eqn.* (3.25) can be rewritten to yield

$$\rho\frac{\mathrm{D}e + {}^1\!/\!{}_2\,(\mathbf{u}\cdot\mathbf{u}) + \phi}{\mathrm{D}t} = -\boldsymbol{\nabla}\cdot\mathbf{q} + \boldsymbol{\nabla}\cdot(\sigma\mathbf{u}). \tag{3.27}$$

Following *Ass.* 3.8, the heat fluxes can be expressed as temperature gradients according to Fourier's law, i.e.,

$$\mathbf{q} = -\lambda \boldsymbol{\nabla} T \tag{3.28}$$

where λ is the thermal conductivity of the fluid. Consequently,

$$\boldsymbol{\nabla} \cdot \mathbf{q} = \boldsymbol{\nabla} \cdot (-\lambda \boldsymbol{\nabla} T) = -\lambda \boldsymbol{\nabla}^2 T. \tag{3.29}$$

By applying *Eqns* (3.10) and (3.28) and subsequently subtracting the mechanical energy, which is the dot product of the velocity vector $\mathbf{u}$ and *Eqn.* (3.23), the *energy equation for compressible flows* is obtained:

$$\boxed{\rho \frac{\mathrm{D}e}{\mathrm{D}t} = \lambda \boldsymbol{\nabla}^2 T - p \boldsymbol{\nabla} \cdot \mathbf{u} + \boldsymbol{\nabla} \cdot (\boldsymbol{\tau} \mathbf{u}) - \mathbf{u} \boldsymbol{\nabla} \cdot \boldsymbol{\tau}} \tag{3.30}$$

where

$$\mathcal{Q} := \boldsymbol{\nabla} \cdot (\boldsymbol{\tau} \mathbf{u}) - \mathbf{u} \boldsymbol{\nabla} \cdot \boldsymbol{\tau} \tag{3.31}$$

is the *dissipation function*, which quantifies the dissipation of mechanical energy into heat. The role of the energy equation is negligible for incompressible, adiabatic flows.

3.1.4. Thermodynamic state equations

As mentioned in the introduction to this chapter, the five equations derived in the previous sections contain seven variables: mass, momenta in three spatial dimensions, energy, temperature, and pressure. Two further relationships are, therefore, necessary to close the set of equations. Following *Ass.* 3.6, the thermodynamic state of the fluid is determined locally, i.e., it does not depend upon spatial or temporal gradients. Consequently, the temperature and pressure can be determined via two algebraic state equations, which can be derived for a resting fluid.

As emphasised earlier, real fluids consist of fluid particles interacting via various forces and, therefore, exchanging momentum. To narrow down the way in which fluid particles interact, the following is assumed:

Assumption 3.10. The fluid considered is in a *gaseous state.*

The fluid particles—or rather *gas particles*—in a resting gas are assumed to move randomly with certain momenta and kinetic energies (Feynman et al. 1965), where both quantities are statistically distributed and the sum of the momenta in all three spatial dimensions is the same. The sum of the momenta in one spatial dimension gives the pressure (hence the assumption of an isotropic mechanical pressure in the fluid), whereas the kinetic energies determine the temperature of the gas.

At this point, it should be clear that the way in which pressure and temperature are related to each other depends not only upon the mass of the individual gas particles, but also upon several assumptions about the forces acting between these particles and the spatial distribution of these forces. It is, thus, not surprising that the state equations are contingent upon these same assumptions. The following can be assumed for most gaseous flows at moderate pressures:

Assumption 3.11. The gas particles are mathematical points, i.e., they have no spatial extent.

Assumption 3.12. The gas particles all have the same mass.

Assumption 3.13. The gas particles interact with each other only by means of perfectly elastic collisions.

Assumptions 3.11, 3.12, and 3.13 are commonly summarised in the theoretical concept of an *ideal gas.* For such an ideal gas, the state variables pressure and temperature are related via the *ideal gas law,* i.e.,

$$p = \rho R T, \tag{3.32}$$

where R is the *specific gas constant,* which is defined as the ratio of the *universal gas constant* to the average molar mass of the gas, i.e.,

$$R = \frac{\mathscr{R}}{M}. \tag{3.33}$$

Furthermore, the specific internal energy and specific enthalpy can be related to the temperature via

$$e = c_V T, \tag{3.34}$$

$$h = c_p T, \tag{3.35}$$

where c_V and c_p are the specific heat capacities

$$c_{\boxtimes} := \frac{C_{\boxtimes}}{m} = \frac{1}{m} \frac{\mathrm{d}Q}{\mathrm{d}T}\bigg|_{\boxtimes = \text{const.}} \tag{3.36}$$

for constant volume and pressure, i.e., the *isochoric* and *isobaric heat capacities*, respectively. In addition, the following can be assumed:

Assumption 3.14. The isochoric and isobaric heat capacities are constant and do not depend upon the temperature and pressure of the gas, i.e., the gas is *calorically perfect.*

It follows that the *heat-capacity ratio* γ can be defined as

$$\gamma := \frac{C_p}{C_V} = \frac{c_p}{c_V} = \text{const.} \tag{3.37}$$

and, according to Mayer's relationship, that

$$R = c_p - c_V. \tag{3.38}$$

3.1.5. Material laws

In *Secs* 3.1.2 and 3.1.3, two proportionality factors were implicitly introduced: the dynamic viscosity μ in *Eqn.* (3.16) and the thermal conductivity λ in *Eqn.* (3.28). Both of these quantities are contingent upon material properties of the medium.

Dynamic viscosity

As it is the proportionality factor between stresses and strain rates, the viscosity is often mistaken for a form of friction. While the effects may be very similar, the *momentum diffusion* occuring in viscous fluids is the result of a more or less random exchange of fluid particles between neighbouring streamlines, as well as an exchange of momentum between interacting gas particles, leading to an averaging of the momenta carried by the streamlines. While it is possible to derive models that predict the viscosity from statistical analyses of ideal gases, the results are generally unsatisfactory. SUTHERLAND (1893) derived a more accurate model by waiving *Asss* 3.11 and 3.13 and, instead, conceptualising the gas particles as *finite particles,* which collide elastically at distances shorter than their diameter, and attract each other with a force inversely related to the distance between them for distances greater than their diameter. Using this gas-particle model SUTHERLAND (1893) obtained the following relationship:

$$\mu = \mu_\text{ref} \frac{T_\text{ref} + C_\text{S}}{T + C_\text{S}} \left(\frac{T}{T_\text{ref}} \right)^{3/2} \tag{3.39}$$

where C_S is the SUTHERLAND constant and where the reference values satisfy the following condition

$$\mu_\text{ref} \frac{T_\text{ref} + C_\text{S}}{T^{3/2}} = 1.456 \times 10^{-6}\,\text{kg/msK}^{1/2}. \tag{3.40}$$

Thermal conductivity

Since the diffusion of momentum and temperature follow similar mechanisms on a gas-particle scale, a relationship between the thermal conductivity λ and the dynamic viscosity μ can be expected. This relationship is characterised by the non-dimensional PRANDTL number:

$$\text{Pr} := \frac{c_p \mu}{\lambda}. \tag{3.41}$$

For gases, the PRANDTL number can be assumed constant across a wide temperature range.

3.1.6. Summary of the governing equations

Compressible

$$\begin{aligned} \frac{\text{D}\rho}{\text{D}t} + \rho \boldsymbol{\nabla} \cdot \mathbf{u} &= 0, \\ \rho \frac{\text{D}\mathbf{u}}{\text{D}t} &= -\boldsymbol{\nabla} p + \mu \boldsymbol{\nabla}^2 \mathbf{u} + \frac{1}{3} \mu \boldsymbol{\nabla} (\boldsymbol{\nabla} \cdot \mathbf{u}) + \mathbf{f}_V, \\ \rho \frac{\text{D}e}{\text{D}t} &= \lambda \boldsymbol{\nabla}^2 T - p \boldsymbol{\nabla} \cdot \mathbf{u} + \boldsymbol{\nabla} \cdot (\boldsymbol{\tau} \mathbf{u}) - \mathbf{u} \boldsymbol{\nabla} \cdot \boldsymbol{\tau}. \end{aligned}$$

Incompressible

$$\begin{aligned} \boldsymbol{\nabla} \cdot \mathbf{u} &= 0, \\ \rho \frac{\text{D}\mathbf{u}}{\text{D}t} &= -\boldsymbol{\nabla} p + \mu \boldsymbol{\nabla}^2 \mathbf{u} + \mathbf{f}_V. \end{aligned}$$

While the above equations fully describe any flow which satisfies *Asss* 3.1 to 3.14 as well as *Imps* 3.1 and 3.2, their complexity poses a hindrance to the derivation of algebraic solutions to most flow problems. This is especially true for flows considered in engineering. Solutions for such flow problems can often only be obtained by solving the *discretised* equations numerically. With high computing power now readily available, it is certainly feasible to obtain numerical solutions for most flow problems. However, the sheer complexity of the flows and the large amount of data generated can impede an intuitive understanding of the individual phenomena involved. In this case, further adaptations or simplifications of the governing equations can make the results more accessible for a more in-depth analysis.

3.2. Turbulent flows

It is a property of the Navier–Stokes equations, and an observable feature of real flows, that they can become unstable and yield chaotic solutions when certain conditions are satisfied. These conditions are *on one hand* the presence of an *initial disturbance* and *on the other hand* sufficiently small damping of the said disturbance. The ensuing *turbulent flow* is highly three-dimensional and unsteady. It is characterised by a significant increase in diffusivity compared to a *laminar flow.*

The degree to which disturbances are damped is determined by the ratio of inertial to viscous forces acting upon a fluid element, i.e.,

$$\frac{\text{Inertial force}}{\text{Viscous force}} = \frac{\rho u \partial u / \partial x_1}{\mu \partial^2 u / \partial x_2^2}. \tag{3.42}$$

Assuming $u \propto \mathcal{U}$, $\partial u / \partial x_1 \propto \mathcal{U}/\ell$, and $\partial^2 u / \partial x_2^2 \propto \mathcal{U}/\ell^2$, where $\mathcal{U}$ and ℓ are the respective characteristic velocity and length scale of the flow problem considered, the Reynolds number is defined as

$$\mathrm{Re} := \frac{\rho \mathcal{U} \ell}{\mu}. \tag{3.43}$$

A sufficiently high Reynolds number indicates the possibility of turbulent flow if disturbances are present. The exact value of the Reynolds number for which this happens is, however, dependent upon the flow problem considered.

A more in-depth discussion of the modelling and prediction of turbulent flows will be given in *Secs* 5.3.2 and 5.3.3.

3.3. Boundary-layer theory

The concept of boundary layers was first put forward by Prandtl (1904).* As detailed in the introduction of Schlichting and Gersten (2006), the concept of boundary layers reconciled the fields of *hydrodynamics* and *hydraulics*. While the former was dominated by mathematical approaches to solving inviscid flow problems, the latter was characterised by empirical approaches to highly specialised classes of problems. According to the framework proposed by Prandtl, the flow is divided into an inviscid and irrotational *free-stream region* and a viscous and rotational *boundary-layer region*. This subdivision allows a simplified prediction of the free stream using *potential theory*, which, in turn, provides boundary conditions for

---

*Prandtl was professor of fluid mechanics in Hanover at that time.

a simplified prediction of the boundary layers. Some key concepts of the boundary-layer theory were introduced in *Sec.* 1.4.1.

3.3.1. Laminar and turbulent boundary layers

Boundary layers can be subdivided into three *flow regimes: laminar, turbulent, and transitional,* where the transitional regime comprises the transition from laminar to turbulent. In the case of laminar boundary-layer flow, the fluid elements move along so-called *streamlines*. These streamlines, or rather *stream tubes* (the volume enclosed by the fluid elements travelling along a streamline), represent enclosed material tubes without any material exchange between neighbouring stream tubes.*

Turbulent boundary layers are characterised by strong velocity fluctuations, both in streamwise and stream-normal direction. The concept of streamlines or stream tubes is, thus, only applicable to turbulent flows if a time-averaged flow field is considered. These velocity fluctuations lead to a strong stream-normal exchange of fluid and momentum between neighbouring fluid elements and can be modelled using the concept of a *turbulent viscosity*. As a result, turbulent boundary layers—which are considered in the present work—exhibit velocity profiles which differ strongly from laminar velocity profiles. A common observation is that boundary layers experience a sudden drop in the shape factor H as they transition from laminar to turbulent (Schlichting and Gersten 2006). This means that their displacement thickness is significantly lower than their momentum thickness. Likewise, the increased lateral momentum exchange causes turbulent boundary layers to be more resilient against flow separation.

3.3.2. Boundary-layer equations

To derive a set of equations which explicitly model the behaviour of boundary layers, four simplifying steps need to be taken first.

The first simplification is that only steady boundary layers are considered, i.e., *Ass.* 1.1.

The second simplification is that only two-dimensional boundary layers are considered. This reduces the number of momentum-equation components from three to two.

The third simplification is the reintroduction of *Ass.* 1.2 (*incompressible flow*). Incompressibility can be assumed for the diffuser flows considered in this work, as they exhibit very low flow velocities or, expressed in fractions of the speed of sound a, i.e.,

$$\mathrm{Ma} := \frac{u}{a}, \tag{3.44}$$

low Mach numbers. As a consequence, all terms containing the divergence of the velocity field, $\boldsymbol{\nabla} \cdot \mathbf{u}$, vanish.

The fourth simplification is also partially rooted in the low flow velocities (and associated gradients) expected as well as the assumption of adiabatic flow (see *Ass.* 1.6): in the absence of both heat fluxes across the boundaries and strong heat sources due to dissipation, a

---

[*] The assumption of no material exchange is only valid within the context of continuum fluid mechanics, as modelled by the Navier–Stokes equations. In reality, there is an exchange of fluid molecules or atoms. This exchange is, however, modelled as the molecular viscosity in continuum fluid mechanics (see *Sec.* 3.1.5).

constant temperature throughout the entire flow can be assumed. Consequently, the energy equation does not need to be considered.

Without volume forces, the simplified equations then give, written in component form,

$$\frac{\partial u_1}{\partial x_1} + \frac{\partial u_2}{\partial x_2} = 0, \tag{3.45}$$

$$\rho u_1 \frac{\partial u_1}{\partial x_1} + \rho u_2 \frac{\partial u_1}{\partial x_2} = -\frac{\partial p}{\partial x_1} + \mu \left(\frac{\partial^2 u_1}{\partial x_1 \partial x_1} + \frac{\partial^2 u_1}{\partial x_2 \partial x_2} \right), \tag{3.46}$$

$$\rho u_1 \frac{\partial u_2}{\partial x_1} + \rho u_2 \frac{\partial u_2}{\partial x_2} = -\frac{\partial p}{\partial x_2} + \mu \left(\frac{\partial^2 u_2}{\partial x_1 \partial x_1} + \frac{\partial^2 u_2}{\partial x_2 \partial x_2} \right). \tag{3.47}$$

To derive a set of equations which describes the boundary-layer flow, the following problem is considered: a flat plate with a finite characteristic length ℓ in x_1 direction, a free stream with the characteristic velocity $\mathcal{U}_\infty$, and a boundary-layer thickness δ in x_2 direction, i.e., normal to the wall. Thus, x_1 can be non-dimensionalised with ℓ, x_2 with δ and, furthermore, p with $\rho\,\mathcal{U}_\infty^2$. Assuming that

$$\frac{\partial u_1}{\partial x_1} \sim \frac{\mathcal{U}}{\ell}, \tag{3.48}$$

it can be estimated from *Eqn.* (3.45) that

$$\frac{\mathcal{U}}{\ell} \sim \frac{u_2}{\delta}. \tag{3.49}$$

Moreover, it can be inferred from the following proportionality for the boundary-layer thickness (Schlichting and Gersten 2006):

$$\delta \propto \sqrt{\frac{\mu x}{\rho\,\mathcal{U}_\infty}} \tag{3.50}$$

that

$$\frac{\delta}{\ell} \propto \frac{1}{\sqrt{\mathrm{Re}_\ell}} \tag{3.51}$$

where

$$\mathrm{Re}_\ell := \frac{\rho\,\mathcal{U}_\infty \ell}{\mu}. \tag{3.52}$$

By inserting the transformations obtained from the above order-of-magnitude analysis into the simplified equations, it follows that

$$\frac{\partial {u_1}^+}{\partial {x_1}^+} + \frac{\partial {u_2}^+}{\partial {x_2}^+} = 0, \tag{3.53}$$

$${u_1}^+ \frac{\partial {u_1}^+}{\partial {x_1}^+} + {u_2}^+ \frac{\partial {u_1}^+}{\partial {x_2}^+} = -\frac{\partial p^+}{\partial {x_1}^+} + \frac{1}{\mathrm{Re}_\ell} \frac{\partial^2 {u_1}^+}{\partial {x_1}^+ \partial {x_1}^+} + \frac{\partial^2 {u_1}^+}{\partial {x_2}^+ \partial {x_2}^+}, \tag{3.54}$$

$$\frac{1}{\mathrm{Re}_\ell} {u_1}^+ \frac{\partial {u_2}^+}{\partial {x_1}^+} + \frac{1}{\mathrm{Re}_\ell} {u_2}^+ \frac{\partial {u_2}^+}{\partial {x_2}^+} = -\frac{\partial p^+}{\partial {x_2}^+} + \frac{1}{\mathrm{Re}_\ell^2} \frac{\partial^2 {u_2}^+}{\partial {x_1}^+ \partial {x_1}^+} + \frac{1}{\mathrm{Re}_\ell} \frac{\partial^2 {u_2}^+}{\partial {x_2}^+ \partial {x_2}^+}, \tag{3.55}$$

where $\boxtimes^+$ denotes the transformed variables.

It is evident that several terms disappear in these equations at a sufficiently high Reynolds number. This condition is often satisfied for flows considered in engineering. By applying the limit $\mathrm{Re}_\ell \to \infty$[*] and reversing the transformation, the *boundary-layer equations* as derived by Prandtl (1904) are finally obtained:

$$\frac{\partial u_1}{\partial x_1} + \frac{\partial u_2}{\partial x_2} = 0, \tag{3.56}$$

$$u_1 \frac{\partial u_1}{\partial x_1} + u_2 \frac{\partial u_1}{\partial x_2} = -\frac{1}{p}\frac{\partial p}{\partial x_1} + \mu \frac{\partial^2 u_1}{\partial x_2 \partial x_2}, \tag{3.57}$$

$$0 = -\frac{\partial p}{\partial x_2}. \tag{3.58}$$

The boundary-layer equations carry some implications: *Firstly,* only the wall-parallel shear stresses appear in *Eqn.* (3.57) since they are of significantly greater magnitude than their wall-normal counterparts. This is not surprising, considering that the wall-normal velocity gradients are considerably higher than those in the flow direction. *Secondly, Eqn.* (3.58) indicates that the wall-normal pressure gradient is zero in the boundary layer, i.e., the local pressure is dictated entirely by the free stream.

It follows that the wall-parallel pressure gradient can be expressed in terms of a free-stream acceleration parameter. Neglecting the temporal derivative (see *Ass.* 1.1) and body-force terms, the Euler equation of the free-stream velocity in one dimension gives

$$-\frac{1}{\rho}\frac{\partial p}{\partial x_1} = \mathcal{U}_\infty \frac{\partial \mathcal{U}_\infty}{\partial x_1}, \tag{3.59}$$

where the right-hand side defines the free-stream acceleration parameter. By inserting *Eqn.* (3.59) into *Eqn.* (3.57), the condition of a constant pressure in wall-normal direction stated in *Eqn.* (3.58) is implicitly satisfied, whereupon the above set of equations can be further simplified to

$$\frac{\partial u_1}{\partial x_1} + \frac{\partial u_2}{\partial x_2} = 0, \tag{3.60}$$

$$u_1 \frac{\partial u_1}{\partial x_1} + u_2 \frac{\partial u_1}{\partial x_2} = \mathcal{U}_\infty \frac{\partial \mathcal{U}_\infty}{\partial x_1} + \mu \frac{\partial^2 u_1}{\partial x_2 \partial x_2}. \tag{3.61}$$

3.3.3. Momentum integral

The boundary-layer equations shown above still represent a set of non-linear partial differential equations and, hence, require numerical solving in most cases. Due to computational limitations[†] in the early days of boundary-layer theory, von Kármán (1921) put forward an integral approach to describe the behaviour of boundary layers. This approach was further formalised and developed into the present notation of the von Kármán momentum integral by Gruschwitz (1931).

The momentum-integral equation is obtained by integrating *Eqn.* (3.57) or (3.61) in the wall-normal direction across the boundary layer, i.e., from $x_2 = 0$ to $x_2 = \delta$. Using the

---

[*] Here, ∞ denotes infinity instead of the free stream.

[†] Calculations had to be performed by hand.

displacement and momentum thicknesses introduced in *Eqns* (1.29) and (1.30), the integral momentum equation of the boundary layer is, according to Gruschwitz (1931),

$$\frac{\mathrm{d}\vartheta}{\mathrm{d}x_1} + \frac{\delta^*}{\mathcal{U}_\infty}\frac{\mathrm{d}\,\mathcal{U}_\infty}{\mathrm{d}x_1} + \frac{2\vartheta}{\mathcal{U}_\infty}\frac{\mathrm{d}\,\mathcal{U}_\infty}{\mathrm{d}x_1} = \frac{\tau_0}{\rho\,\mathcal{U}_\infty^2}, \tag{3.62}$$

where the right-hand side represents the impact of skin friction with τ_0 representing the shear stress immediately at the wall. With the definition of the boundary-layer shape factor from *Eqn.* (1.36), the equation becomes

$$\frac{\mathrm{d}\vartheta}{\mathrm{d}x_1} + (H+2)\,\frac{\vartheta}{\mathcal{U}_\infty}\frac{\mathrm{d}\,\mathcal{U}_\infty}{\mathrm{d}x_1} = \frac{\tau_0}{\rho\,\mathcal{U}_\infty^2}. \tag{3.63}$$

This equation is evidently considerably simpler than Prandtl's system of boundary-layer equations. The development of the shape factor, however, is heavily dependent upon the initial shape of the boundary layer. Pohlhausen (1921) published, in the same year as von Kármán[*], a calculation procedure for the above equation. He did so by defining polynomials to describe the boundary-layer velocity profiles and parametrising them using the boundary-layer quantities appearing in the above equation.

3.3.4. Entrainment relationship

Pohlhausen's method, however, failed to produce results for separated boundary layers, as explained by Veldman (2017) in his review of the boundary-layer theory. The solution to this problem would be found more than 30 years later when Head (1958) attempted to derive an equation similar in nature to *Eqn.* (3.63), yet related to mass conservation in the boundary layer. Head (1958) hypothesised an *entrainment* of mass from the free stream into the boundary layer. By introducing the shape factor,

$$H_{\delta-\delta^*} := \frac{\delta-\delta^*}{\vartheta}, \tag{3.64}$$

and the entrainment rate,

$$E := \frac{\mathrm{d}Q_{\mathrm{BL}}}{\mathrm{d}x_1} = \frac{\mathrm{d}}{\mathrm{d}x_1}\left[\,\mathcal{U}_\infty\,(\delta-\delta^*)\right], \tag{3.65}$$

as the spatial derivative of the boundary-layer volume-flow rate per unit span Q, he formulated the *entrainment relationship*,

$$\frac{1}{\mathcal{U}_\infty}E = \frac{1}{\mathcal{U}_\infty}\frac{\mathrm{d}}{\mathrm{d}x_1}\left[\,\mathcal{U}_\infty\,(\delta-\delta^*)\right] = \mathfrak{f}\left(H_{\delta-\delta^*}\right), \tag{3.66}$$

as an empirical function of his newly developed shape factor.

---

[*] Both articles were actually published in the same journal issue.

3.3.5. Application to diffusers

As mentioned in *Sec.* 2.4, Kline (1978) and, in succession, Bardina et al. (1982) developed a one-dimensional prediction method for planar and annular diffuser flows. The method is based upon the approach of solving *Eqns* (3.63) and (3.66) simultaneously.

The dependent variables, for which the system is solved, are the blockage factor,

$$B := \frac{\delta^*}{\mathcal{W}}, \tag{3.67}$$

and a *boundary-layer blockage factor,*

$$\Lambda := \frac{\delta^*}{\delta}, \tag{3.68}$$

where δ^* is the average displacement thickness and $\mathcal{W}$ is the diffuser width for planar diffusers and the channel height for annular diffusers. It is worth to be noted that the blockage factor B is defined differently than in *Eqns* (1.38) and (1.39); the definition given in *Eqn.* (3.67) will be used in the following.

Using the non-dimensional wall-wake boundary-layer velocity profiles of Coles (1956, 1962), Bardina et al. (1982) derived correlations between Λ and the non-dimensional shear velocity ${u_\tau}^+$ which, in turn, is used to predict, e.g., the skin-friction coefficient:

$$C_\mathrm{f} := 2\kappa^2 \left|{u_\tau}^+\right| {u_\tau}^+ \tag{3.69}$$

where κ is the von Kármán constant. Together with the definition of an alternative boundary-layer shape parameter,

$$h := \frac{H-1}{H} = \frac{\delta^* - \delta}{\delta^*}, \tag{3.70}$$

and using purely non-dimensional quantities, *Eqns* (3.63) and (3.66) may be rewritten as follows:

$$\begin{aligned} \frac{(1-h+C_2) + 2B\,(2-2h+0.015/\Lambda)}{B\,(1-2B)} \frac{\mathrm{d}B}{\mathrm{d}{x_1}^+} - C_1 \frac{\mathrm{d}\Lambda}{\mathrm{d}{x_1}^+} &= \frac{C_\mathrm{f}/2 + \beta E^+}{B\,\mathcal{W}^+} \\ &\quad + (2-2h+0.015/\Lambda)\,\frac{1}{\mathcal{W}^+}\frac{\mathrm{d}\mathcal{W}^+}{\mathrm{d}{x_1}^+} \\ &\quad - (1-h)\,\frac{1}{{r_\mathrm{m}}^+}\frac{\mathrm{d}{r_\mathrm{m}}^+}{\mathrm{d}{x_1}^+}, \end{aligned} \tag{3.71}$$

$$\frac{1}{B\,(1-2B)}\frac{\mathrm{d}B}{\mathrm{d}{x_1}^+} - \frac{1}{\Lambda\,(1-\Lambda)}\frac{\mathrm{d}\Lambda}{\mathrm{d}{x_1}^+} = E^+ - \frac{1}{{r_\mathrm{m}}^+}\frac{\mathrm{d}{r_\mathrm{m}}^+}{\mathrm{d}{x_1}^+}, \tag{3.72}$$

where ${x_1}^+$ is the non-dimensional wall-parallel coordinate and where C_1 and C_2 are calculated from empirical correlations dependent upon Λ and ${u_\tau}^+$. The derivative of the mid-span radius $\mathrm{d}{r_\mathrm{m}}^+/\mathrm{d}{x_1}^+$ has been adapted from Bardina et al. (1982) to account for the changes in transverse curvature. It vanishes in the case of an equiangular annular diffuser.* The

---

***Id est,* an annular diffuser where the convergence angle of the hub is equal and opposite to the divergence angle of the casing.

corresponding set of equations for planar diffusers is provided by Bardina et al. (1981) and Bardina et al. (1982).

A detailed derivation of the above equations is given by Bardina et al. (1982); a more succinct description, albeit for planar diffusers only, is given by Bardina et al. (1981). The method provides accurate predictions of attached and separated diffuser flows, as demonstrated by Bardina et al. (1982) and—in less detail and for planar diffusers only—by Bardina et al. (1981).

3.4. Vortex theory

By subtracting half of the strain-rate tensor, i.e., $1/2\,\mathbf{S}$ from the transposed velocity-gradient tensor $(\nabla \otimes \mathbf{u})$, i.e.,

$$(\nabla \otimes \mathbf{u}) - \frac{1}{2}\left[(\nabla \otimes \mathbf{u}) + (\mathbf{u} \otimes \nabla)\right] = \frac{1}{2}\left[(\nabla \otimes \mathbf{u}) - (\mathbf{u} \otimes \nabla)\right], \tag{3.73}$$

the following antisymmetric tensor is obtained:

$$\mathbf{R} := \begin{pmatrix} 0 & \frac{1}{2}\left(\frac{\partial u_2}{\partial x_1} - \frac{\partial u_1}{\partial x_2}\right) & \frac{1}{2}\left(\frac{\partial u_3}{\partial x_1} - \frac{\partial u_1}{\partial x_3}\right) \\ \frac{1}{2}\left(\frac{\partial u_1}{\partial x_2} - \frac{\partial u_2}{\partial x_1}\right) & 0 & \frac{1}{2}\left(\frac{\partial u_3}{\partial x_2} - \frac{\partial u_2}{\partial x_3}\right) \\ \frac{1}{2}\left(\frac{\partial u_1}{\partial x_3} - \frac{\partial u_3}{\partial x_1}\right) & \frac{1}{2}\left(\frac{\partial u_2}{\partial x_3} - \frac{\partial u_3}{\partial x_2}\right) & 0 \end{pmatrix}, \tag{3.74}$$

which is called the *rotation-rate tensor* and measures the angular velocity of a fluid element rotating about its own centre. Applying the rotation-rate tensor to the differential vector d$\mathbf{x}$ rotates the terminal point of d$\mathbf{x}$ about its origin. After some rearrangements, it can be shown by comparison that this relative motion is characterised by the vector $\mathbf{\Omega}$, i.e.,

$$\mathbf{R}\mathrm{d}\mathbf{x} = \frac{1}{2}\mathbf{\Omega} \times \mathrm{d}\mathbf{x}, \tag{3.75}$$

where

$$\mathbf{\Omega} := \nabla \times \mathbf{u} \tag{3.76}$$

is the *vorticity* vector; flow regions of non-zero vorticity are called *rotational flow regions*.

3.4.1. Vortex classification

Just like the rotation-rate tensor, the vorticity characterises the rotation of a fluid element about its own centre. It is important to note that a non-zero vorticity does not necessarily imply *swirling flow*, that is, an angular velocity of the fluid element about an external centre of rotation.

Rotational vortex

By applying the relationship given in *Eqn.* (3.75) to a finite region of swirling flow with a constant angular velocity determined by $\|\mathbf{R}\|_F := \sqrt{\mathbf{R} : \mathbf{R}}$, it is shown that the vorticity of the swirling flow region will be twice as large. A flow region which satisfies this relationship is called a *rotational vortex*; the corresponding motion is termed *rigid-body rotation.*

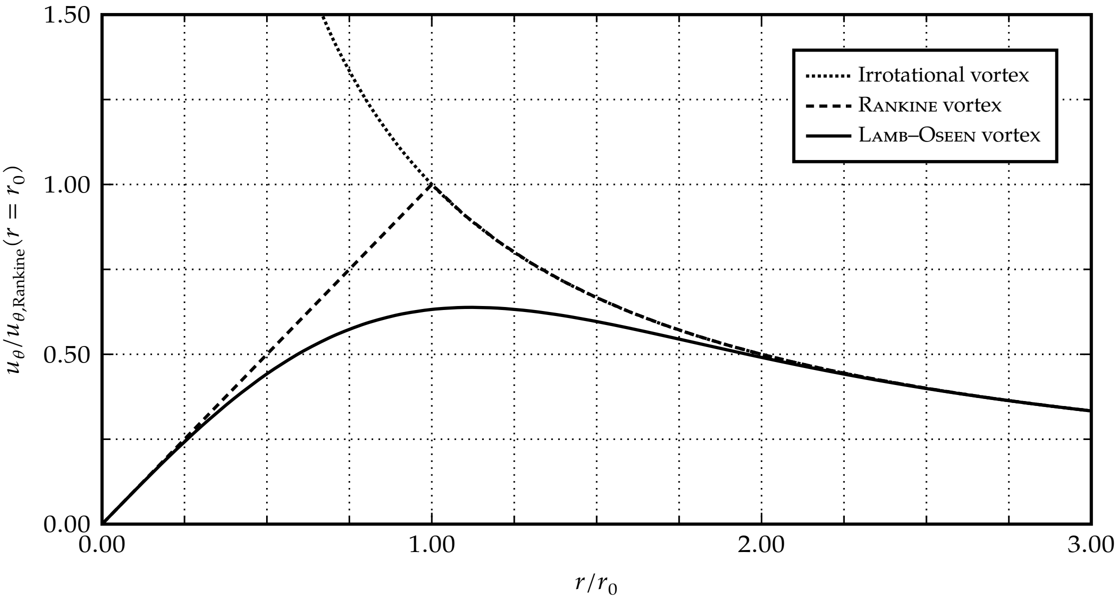

Figure 3.2.: Distributions of circumferential velocity provided by different vortex models

Irrotational vortex

It is also possible that a flow region undergoes a swirling motion without being rotational, i.e., $\mathbf{\Omega} = 0$. Such a flow region is called an *irrotational* or *potential vortex.* An irrotational vortex is a two-dimensional axisymmetric flow where the radial distribution of the circumferential velocity is determined by

$$u_\theta = \frac{\Gamma}{2\pi r} \tag{3.77}$$

where the *circulation* is defined as

$$\Gamma := \oint_{\partial \mathcal{S}} \mathbf{u} \cdot \mathrm{d}\mathbf{s}. \tag{3.78}$$

It can be shown that this solution satisfies $\mathbf{\Omega} = 0$ for $r > 0$.

While a pure potential vortex is merely a theoretical concept, Hamel (1941) showed that its velocity distribution corresponds to the analytical solution of the Navier–Stokes equations for an unbounded, two-dimensional flow field around a rotating cylinder. In this case, the conservation of kinetic energy is still fulfilled throughout the entire flow field, because the work performed on the fluid by the rotating cylinder is identical to the viscous dissipation rate of kinetic energy.

Viscous fluids

Strictly speaking, potential vortices can only occur in inviscid fluids (unless driven by a rotating cylinder, as explained above). For sufficiently small radial velocity gradients and, consequently, a sufficiently large radial distance from the centre of rotation, the potential-vortex model is also applicable to viscous fluids. For smaller radial distances, however, the contribution of viscous effects increases. The result is a finite rotational flow region around the centre of rotation. This has led to several models which describe vortices in viscous fluids to varying degrees of accuracy. Some of these models shall be introduced below.

Rankine vortex

An early and simple model of vortices in viscous fluids was devised by Rankine. Anticipating the findings of Hamel (1941), Rankine postulated that vortices in viscous fluids can be subdivided into an irrotational—or potential—outer region and a rotational—or rigid-body—vortex core with a characteristic core radius r_0:

$$u_\theta = \begin{cases} (\Gamma r) \,/\, \left(2\pi r_0^2\right) & \text{for } r \leq r_0, \\ \Gamma / \,(2\pi r) & \text{for } r > r_0. \end{cases} \tag{3.79}$$

It is evident that the Rankine vortex is only a rough approximation of the behaviour of a real vortex. This is most apparent when considering the radial discontinuity of the velocity gradient $\partial u_\theta / \partial r$.

Lamb–Oseen vortex

A significantly more elaborate vortex model was derived by Oseen (1911), Hamel (1917), and Lamb (1932). This Lamb–Oseen vortex* describes a vortex decaying over time where the initial conditions represent an irrotational vortex. It can be shown that this vortex is an analytical solution of the Navier–Stokes equations for $t > 0$. The radial distribution of circumferential velocity is, in cylindrical coordinates,

$$u_\theta = \frac{\Gamma_0}{2\pi r}\left(1 - \mathrm{e}^{-\frac{r^2}{4\nu t}}\right) \tag{3.80}$$

where $2\sqrt{\nu t} = r_0$ gives the characteristic radius of the vortex. The characteristic radius corresponds to the core radius of a Rankine vortex towards which the velocity distribution converges for $r \rightarrow \infty$†. Velocity profiles of the Lamb–Oseen, Rankine, and irrotational vortices are shown in *Fig.* 3.2.

By deriving the gradient of *Eqn.* (3.80) in cylindrical coordinates, i.e.,

$$\begin{aligned} (\nabla \mathbf{u})_{r,\theta} &= \begin{pmatrix} 0 & -\frac{u_\theta}{r} \\ \frac{\partial u_\theta}{\partial r} & 0 \end{pmatrix}_{r,\theta} \\ &= \begin{pmatrix} 0 & -\frac{\Gamma_0}{2\pi r^2}\left(1 - \mathrm{e}^{-\frac{r^2}{4\nu t}}\right) \\ -\frac{\Gamma_0}{2\pi r^2}\left(1 - \mathrm{e}^{-\frac{r^2}{4\nu t}}\right) - \frac{\Gamma_0}{2\pi r}\mathrm{e}^{-\frac{r^2}{4\nu t}}\left(-\frac{r}{2\nu t}\right) & 0 \end{pmatrix}_{r,\theta} \end{aligned} \tag{3.81}$$

and applying *Eqn.* (3.15), the strain-rate tensor is obtained:

$$\mathbf{S}_{r,\theta} = \begin{pmatrix} 0 & \frac{\Gamma_0}{8\pi\nu t}\left(1 + \frac{4\nu t}{r^2}\right)\mathrm{e}^{-\frac{r^2}{4\nu t}} - \frac{\Gamma_0}{2\pi r^2} \\ \frac{\Gamma_0}{8\pi\nu t}\left(1 + \frac{4\nu t}{r^2}\right)\mathrm{e}^{-\frac{r^2}{4\nu t}} - \frac{\Gamma_0}{2\pi r^2} & 0 \end{pmatrix}_{r,\theta}. \tag{3.82}$$

The strain-rate distribution along the radial coordinate is then:

$$S_{r,\theta} = \frac{\Gamma_0}{4\pi\nu t}\left(1 + \frac{4\nu t}{r^2}\right)\mathrm{e}^{-\frac{r^2}{4\nu t}} - \frac{\Gamma_0}{\pi r^2}. \tag{3.83}$$

---

[*] It is also commonly referred to as Hamel–Oseen vortex or simply Oseen vortex.

[†] Here, ∞ refers to infinity.

3.4.2. Vorticity transport

The transport of vorticity in a flow is obtained by applying the curl operator to the Navier–Stokes equations. This operation results in

$$\begin{aligned}\frac{\mathrm{D}\boldsymbol{\Omega}}{\mathrm{D}t} = \rho\left(\mathbf{u}\otimes\boldsymbol{\nabla}\right)\cdot\boldsymbol{\Omega} - \rho\boldsymbol{\Omega}\left(\boldsymbol{\nabla}\cdot\mathbf{u}\right) + \frac{1}{\rho}\boldsymbol{\nabla}\rho\times\boldsymbol{\nabla}p + \rho\frac{1}{3}\boldsymbol{\nabla}\mu\times\left[\boldsymbol{\nabla}(\boldsymbol{\nabla}\cdot\mathbf{u})\right] \\ + \mu\boldsymbol{\nabla}^2\boldsymbol{\Omega} + \boldsymbol{\nabla}\mu\times\left(\boldsymbol{\nabla}^2\mathbf{u}\right) + \rho\boldsymbol{\nabla}\times\mathbf{f},\end{aligned} \quad (3.84)$$

which constitutes the vorticity equation. Assuming that the fluid is incompressible, barotropic* and in an non-accelerating frame of reference, the above equation simplifies to

$$\rho\left(\boldsymbol{\Omega}\otimes\boldsymbol{\nabla}\right)\cdot\mathbf{u} = \rho\left(\mathbf{u}\otimes\boldsymbol{\nabla}\right)\cdot\boldsymbol{\Omega} + \mu\boldsymbol{\nabla}^2\boldsymbol{\Omega} \quad (3.85)$$

where the first term on the right-hand side describes the *vorticity deformation* due to velocity gradients and the second term the *vorticity diffusion.*

Depending upon the relative orientation of the velocity gradient and vorticity vector, this deformation can assume several fundamental modes:

1. vortex stretching, if a positive velocity gradient acts along the vorticity vector,
2. vortex squeezing, if a negative velocity gradient acts along the vorticity vector, and
3. vortex bending, if a velocity gradient acts normal to the vorticity vector.

3.5. Secondary flow in axial turbines

It can be inferred from the literature discussed in *Sec.* 2.1.4 that secondary-flow structures generated in the turbine, more specifically the tip-leakage vortex, can mitigate flow separation in a subsequent diffuser. A brief and simple introduction to the flow topology of the most prominent secondary-flow structures in subsonic axial turbines shall be given with a focus on the tip-leakage vortex. Detailed elaborations about the matter of secondary flow in axial turbines can be found in Sieverding (1985) or Langston (2001).

The individual secondary-flow structures can be classified into two categories: secondary-flow vortices which are fed directly by the end-wall boundary layers and vortices which are generated as a result of the aerodynamic blade-loading distribution. For the sake of brevity, the terms *end-wall–bound secondary flow* and *blade-bound secondary flow* shall be used.

3.5.1. End-wall–bound secondary flow

It follows from the nature of boundary layers that they are rotational flow regions. This means boundary layers can be represented as a bundle of *vorticity lines* normal to the flow direction and parallel to the wall, as indicated by the vortex line on the left-hand side of *Fig.* 3.3. Most end-wall–bound secondary-flow phenomena can be explained via deformation of these vorticity lines (see *Eqn.* 3.85). They are shown on the left-hand side of *Fig.* 3.3 together with the resulting vortex system.

---

*This means that surfaces of constant pressure and surfaces of constant density are coplanar.

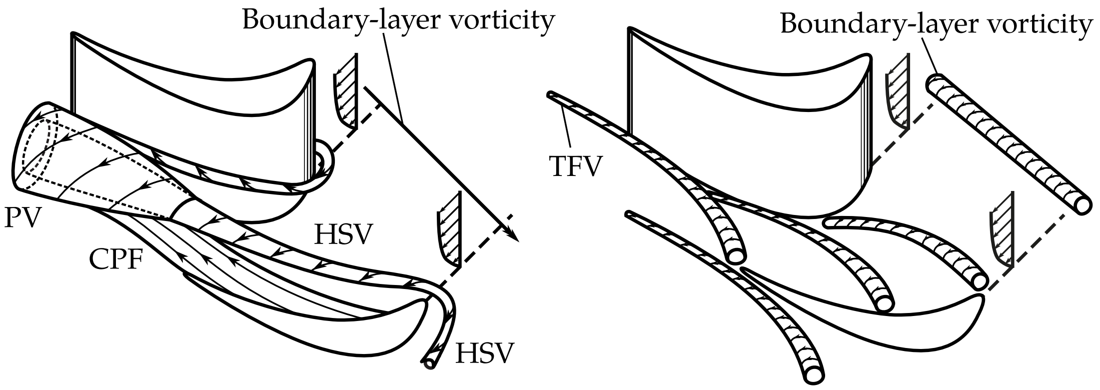

Figure 3.3.: Left (adapted from Pöhler 2013): horseshoe vortex (HSV), passage vortex (PV), and cross-passage flow (CPF); right: trailing filament vortex (TFV)

Horseshoe vortex

The *horseshoe vortex* is the secondary-flow structure which originates the furthest upstream: it forms as the incoming boundary-layer vorticity lines impinge upon the leading edge of the blade. The adverse pressure gradient caused by the potential field of the blade bends the vorticity lines, which drape around the leading edge in a horseshoe-like shape. The vorticity lines, now collinear with the streamlines, cause a helical motion of the latter and lead to the formation of the horseshoe vortex.

Passage vortex

The *passage vortex* is a result of the flow turning within the passage. The vortex lines of the incoming boundary layer undergo a change in orientation, since they remain roughly normal to the flow direction. The conservation of angular momentum necessitates the generation of a negative stream-wise vorticity component in order to compensate for this realignment of the vorticity vectors. This process can be understood as analogous to the effect of *gyroscopic precession* experienced by solid bodies. The induced rotational velocity field gives rise to the *cross-passage flow.*

Trailing filament vortex

The trailing filament vortex is caused by the differences in stream-wise acceleration between the pressure side of a blade and the suction side of the neighbouring blade, as shown on the right-hand side of *Fig.* 3.3. For the sake of visual clarity, the vorticity of the incoming boundary layer is depicted as a vortex tube, even though it does not form a coherent vortex, but merely a region of rotational flow. The differential acceleration in the passage causes strong stretching and bending near the suction side, i.e., an increase in vorticity with a simultaneous decrease in the cross-sectional area of the vortical flow region. The result of this simultaneous increase in vorticity and alignment with the flow is the *trailing filament vortex.*

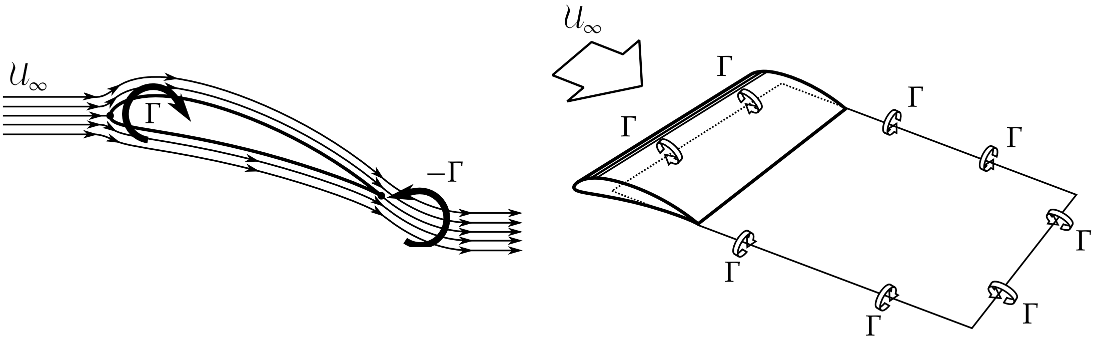

Figure 3.4.: Left: bound and free vortex for two-dimensional aerofoil; right: three-dimensional vortex system (adapted from Schlichting and Truckenbrodt 2001)

3.5.2. Blade-bound secondary flow

The blade-bound secondary-flow phenomena are closely tied to the generation of dynamic lift. Considering a two-dimensional potential flow around a lift-generating aerofoil, the flow can be decomposed into a purely translational component and a circulation around the aerofoil. This circulation is commonly referred to as the *bound vortex.* As shown in *Fig.* 3.4, a *free vortex* of equal and opposite circulation must then form downstream of the aerofoil due to the conservation of circulation in inviscid fluids, which is expressed in Thompson's theorem:

$$\frac{\mathrm{d}\Gamma}{\mathrm{d}t} \equiv 0. \tag{3.86}$$

Now considering a three-dimensional wing of finite span, the bound vortex is represented by a vortex line going through the wing along its span. Helmholtz's third theorem*, however, states that a vortex line in an inviscid fluid must be closed or end on the boundary of the flow domain (von Helmholtz 1858). The resulting system of bound vortex, free vortex and trailing vortices is shown in *Fig.* 3.4. This explanation, using Prandtl's lifting-line theory is, of course, heavily simplified.

To add to the accuracy, and complexity, of this simple representation of a wing, it must be considered that the wing does not generate the same lift at each span-wise position. Rather, the lift decreases approaching the wing tips. This is equivalent to a decrease in bound circulation. Again, invoking Prandtl's lifting line theory and dividing the wing into infinitesimal span-wise sections, starting from the symmetry plane and proceeding towards its tip, it can be determined that the circulation decreases by dΓ from one section to the next. Every section is, consequently, associated with a trailing vortex line of infinitesimal circulation. While the trailing vortex lines are now spread across a greater cross-sectional area, their total circulation remains the same as in the first case.

---

[*] The order in which Helmholtz's theorems are numbered varies in the literature. Here, the numbering has been chosen according to von Helmholtz (1858).

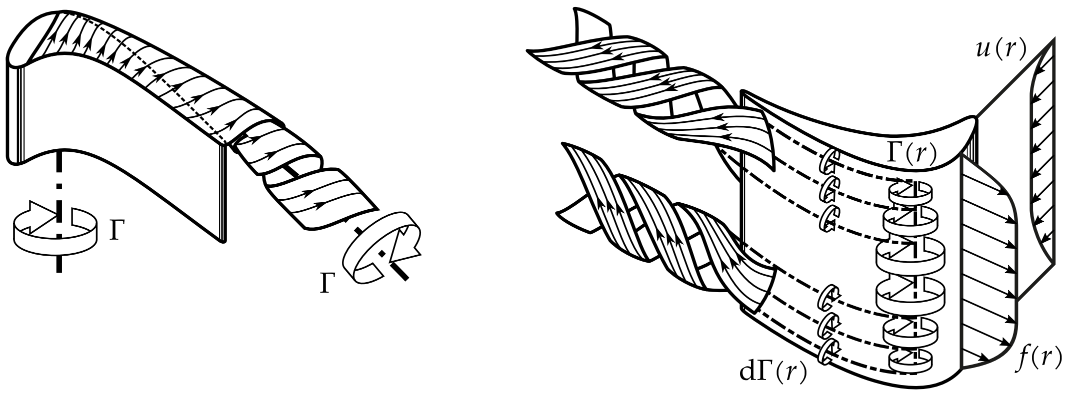

Figure 3.5.: Left: tip-leakage vortex (adapted from Mimic et al. 2018a); right: trailing shed vortices

Tip-leakage vortex

The formation of the tip-leakage vortex in a turbine, as shown in *Fig.* 3.5, can be explained using the same model described in the previous paragraph. The proximity of the blade to the casing, however, causes some differences in the span-wise loading distribution and, ultimately, in the shape of the vortex. These differences are caused *on one hand* by the limited gap between the blade and casing, which limits the mass-flow rate of the tip-leakage flow, and *on the other hand* by the casing boundary layer, which can reduce the aerodynamic loading of the tip region of the blade. In addition, a higher degree of three-dimensionality and viscous effects can be expected where the casing boundary layer and tip-leakage vortex interact. These influences, however, are highly dependent upon the blade and casing geometry and exceed the scope of this work.

Trailing shed vortex

The end-wall boundary layers, as mentioned in the previous paragraph, reduce the blade loading and, thus, the circulation in the near-wall regions. This causes the formation of the *trailing shed vortex* in a similar manner to the trailing vortices and the tip-leakage vortex as illustrated in *Fig.* 3.5.

Chapter 4.

Theory

The aim of this chapter is to devise a coherent theory that approaches the problem of turbine-induced boundary-layer stabilisation in annular diffusers. To approach the problem, the stabilisation process will be subdivided into a stream of "events". The sensitivity of each event towards the preceding one will then be evaluated. Starting with simple considerations about the relationship between the static-pressure recovery of the diffuser and the effective-area reduction due to boundary layers, the focus will move on to the stabilisation process taking place between the vortex and boundary layer, the transport of vortices and, finally, upstream towards the generation of vortices in the rotor and the link to certain integral rotor parameters.

4.1. Ideal reference

The first step towards a quantitative understanding of turbine–diffuser interactions is to define a suitable reference flow. This reference problem should be accessible algebraically, yet resemble the flow problem considered as closely as possible. It is then necessary to quantify the deviations of the real flow from this idealised view. The reference flow was introduced earlier in the form of the inviscid diffuser flow with homogeneous inlet swirl. Therefore, instead of the static-pressure recovery, the diffuser effectiveness will be considered, which is the ratio of the effective static-pressure recovery to the ideal static-pressure recovery with inlet swirl as defined in *Eqn.* (1.21). Using the effectiveness, most swirl-induced effects can be neglected and the focus can be placed on the axial components of the diffuser flow. Consequently, all changes in effectiveness can be attributed to inhomogeneities in the inlet flow field and viscous effects inside the diffuser.

4.2. Diffuser blockage

Although the increase in effective area ratio is, by definition, a result of a decrease in the blockage caused by boundary layers, it occurs in two distinct ways. *The first way* is a simple reduction in boundary layer thickness due to viscous interaction with the free stream. *The second way* is a delay in separation onset caused by changes in the boundary-layer momentum. The purely geometric impact of each way will be considered first, before approaching the underlying driving mechanisms. Evidently, only the first way is relevant in diffusers with fully attached boundary layers.

To determine how a change in boundary-layer displacement thickness affects the static-pressure recovery, an annular diffuser with constant hub radius and diverging outer walls is

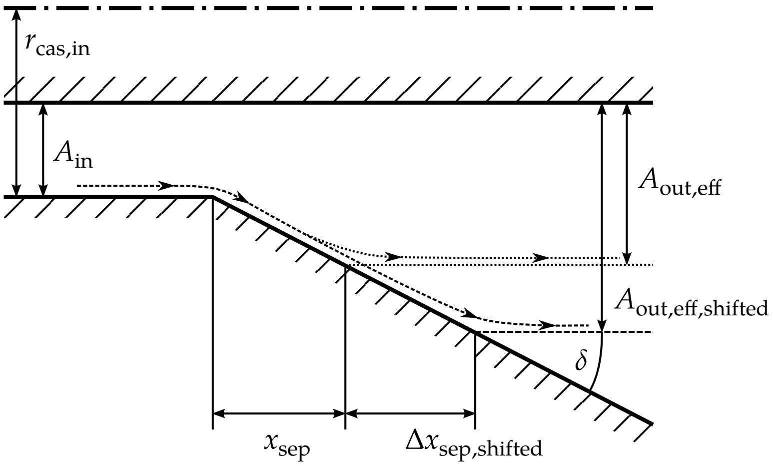

Figure 4.1.: Shifted location of separation onset and resulting difference in effective area ratio (adapted from Mimic et al. 2018c)

considered. With the exception of the boundary layers, the flow is assumed to be inviscid and the boundary layer at the hub is assumed to remain constant. For easier notation, the hub boundary layer is absorbed into the already displaced hub radius r^*_{hub}. Expanding the definition in *Eqn.* (1.34), the effectiveness is then given as

$$\epsilon = \frac{1 - \left[\frac{\left(r_{\mathrm{cas,in}} - \delta^*_{\mathrm{in}}\right)^2 - \left(r^*_{\mathrm{hub}}\right)^2}{\left(r_{\mathrm{cas,out}} - \delta^*_{\mathrm{out}}\right)^2 - \left(r^*_{\mathrm{hub}}\right)^2}\right]^2}{1 - \left[\frac{r^2_{\mathrm{cas,in}} - r^2_{\mathrm{hub}}}{r^2_{\mathrm{cas,out}} - r^2_{\mathrm{hub}}}\right]^2}. \tag{4.1}$$

Because the changes in δ^* are small compared to r, higher order terms of δ^* are negligible. From this, it can be inferred that the effect is not dominant for highly loaded diffusers.

In contrast, the connection between the boundary-layer separation and the change in diffuser effectiveness can be expected to be more dominant in these highly loaded diffusers. Mimic et al. (2018c) considered the diffuser shown in *Fig.* 4.1 and assumed, for the sake of simplicity, inviscid flow and a uniform velocity distribution at the diffuser inlet, where the circumferential flow components are neglected. Further assuming a circumferentially homogeneous flow, the problem can be regarded as two-dimensional.

Upon entering the divergent part of the duct, the flow initially remains attached until x_{sep}, where massive flow separation occurs abruptly. Obviously, an inviscid flow does not experience flow separation, which means that the sudden separation is imposed as a boundary condition in this thought experiment. Not accounting for any viscous effects, Mimic et al. (2018c) assumed that there is no appreciable static-pressure rise downstream of the location of separation onset. The streamlines downstream of the separation are, thus, aligned horizontally. While the last assumption is not accurate for a viscous flow, where static-pressure recovery can still be observed downstream of the separation onset (Senoo and Nishi 1977b), it proves useful in isolating the influence of the spatial shift in the location of separation onset.

It follows from the assumptions stated that the effective area ratio, which is defined similarly to *Eqn.* (1.15), i.e.,

$$\mathfrak{A}_{\text{eff}} = \frac{A_{\text{out,eff}}}{A_{\text{in}}}, \tag{4.2}$$

is significantly lower than the geometric area ratio of the entire diffuser if the flow separates far enough upstream. To express the effective area ratio in terms of the diffuser half-opening angle and location of separation onset, basic trigonometry can be used as shown by Mimic et al. (2018c):

$$\mathfrak{A}_{\text{eff}}\left(x_{\text{sep}}, \delta\right) = 1 + \frac{1}{A_{\text{in}}}\left[\pi x_{\text{sep}} \tan\left(\delta\right)\left(2r_{\text{cas,in}} + x_{\text{sep}} \tan\left(\delta\right)\right)\right]. \tag{4.3}$$

To determine the sensitivity of the effectiveness towards a downstream shift of the separation onset, i.e., the process of boundary-layer stabilisation, the partial derivative of the effectiveness is formed with regard to the location of separation onset, i.e., x_{sep}:

$$\frac{\partial \epsilon}{\partial x_{\text{sep}}} = \frac{1}{c_{p,\text{id}}} \frac{\partial c_{p,\text{eff}}}{\partial x_{\text{sep}}} = \frac{1}{c_{p,\text{id}}} \frac{2}{\mathfrak{A}_{\text{eff}}^3} \left(\frac{\partial \mathfrak{A}_{\text{eff}}}{\partial x_{\text{sep}}}\right). \tag{4.4}$$

The fully expanded expression is obtained by differentiating *Eqn.* (4.3) with regard to x_{sep} and inserting the result into *Eqn.* (4.4), i.e.,

$$\frac{\partial \epsilon}{\partial x_{\text{sep}}} = \frac{1}{c_{p,\text{id}}} \frac{\frac{4\pi}{A_{\text{in}}} \tan\left(\delta\right)\left(r_{\text{cas,in}} + x_{\text{sep}} \tan\left(\delta\right)\right)}{\left[1 + \frac{\pi}{A_{\text{in}}} x_{\text{sep}} \tan\left(\delta\right)\left(2r_{\text{cas,in}} + x_{\text{sep}} \tan\left(\delta\right)\right)\right]^3}. \tag{4.5}$$

The right-hand side of the above equation returns strictly positive values for diffuser half-opening angles greater than zero. *Figure* 4.2 shows solutions of *Eqn.* (4.5) for several diffuser half-opening angles.

It appears that steeper opening angles yield a higher sensitivity of the effectiveness if the location of separation onset is shifted in the first third of the diffuser: for steeper opening angles, the same axial shift of the separation onset yields a greater increase in effective cross-sectional area. This trend is reversed in the remaining diffuser, where steeper opening angles are less sensitive towards the axial shift. The reason for this behaviour can be found in the definition of the ideal static-pressure recovery coefficient. According to *Eqn.* (1.20), the ideal static-pressure recovery coefficient is determined solely by the area ratio and exhibits an initially steep slope, which decreases as $c_{p,\text{id}}$ approaches unity, i.e., any further increase in the area ratio produces a diminishing increase in static-pressure recovery. A steeper opening angle causes the ideal static-pressure recovery to converge faster and, therefore, flatten out earlier than shallower half-opening angles. Because diffusers with steeper half-opening angles tend to exhibit flow separation further upstream, the following hypothesis is inferred:

Hypothesis 4.1. The sensitivity of the diffuser effectiveness towards a given stabilising vortex increases with the diffuser opening angle.

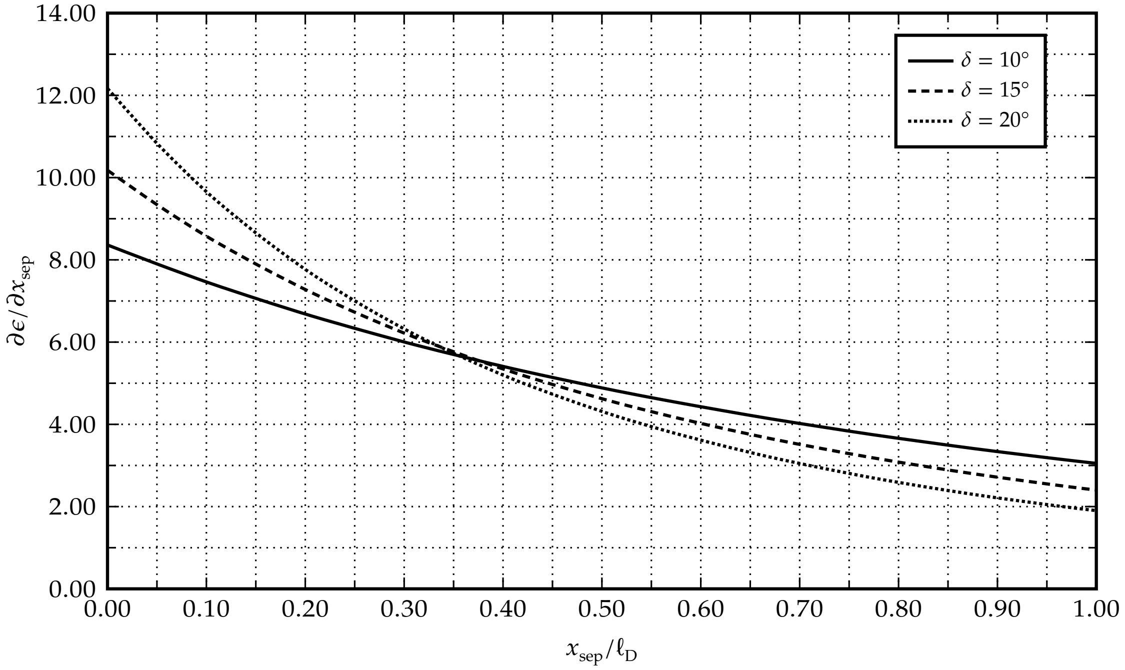

Figure 4.2.: Derivative of the diffuser effectiveness towards the location of separation onset versus non-dimensional location of separation onset according to *Eqn.* (4.5) for different diffuser half-opening angles

4.3. Vortex–boundary-layer interaction

A rigorous, yet accessible description of the interaction process between vortex and boundary layer proves to be distinctly more difficult than for the effect of boundary-layer induced blockage. To achieve this, viscous effects must be considered, as viscosity enables the vortex to exchange mass and momentum with the boundary layer.

As laid out in *Sec.* 3.3, incompressible boundary-layer flows are governed by the laws of conservation of mass and momentum. The one-dimensional representations of boundary layers given in *Secs* 3.3.3 and 3.3.4 connect the boundary layer to the free stream by defining an exchange of momentum and mass through the acceleration term in *Eqn.* (3.63) and the entrainment relationship in *Eqn.* (3.66). As mentioned initially, Bardina et al. (1982) developed a one-dimensional prediction method for attached and separated diffuser flows. The method provided accurate results for a wide range of test cases. However, the method of Bardina et al. (1982) has been devised to predict the behaviour of diffusers with homogeneous inflow. This raises the question:

Can this approach be used to predict the stabilising effect of tip-leakage vortices on boundary layers in diffusers?

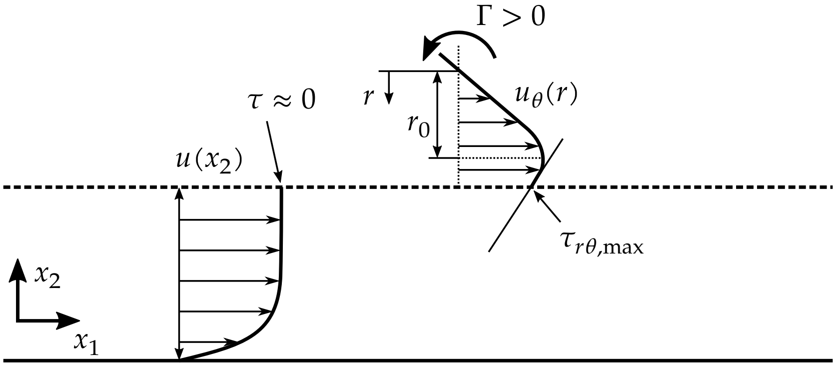

Figure 4.3.: Example of an interaction between a Lamb–Oseen vortex and a boundary layer

4.4. Vortex model

In order to gain some insight into this question, a simple vortex model is developed in this thesis and integrated into the diffuser prediction method of Bardina et al. (1982). The implementation is listed in in *Lst.* A.1 in *App.* A.

Again, the use of several assumptions and simplifications will be necessary. Still viewing the flow as two-dimensional, a Lamb–Oseen vortex (see *Sec.* 3.4.1) with the circulation Γ is considered, which is convected closely along the free-stream edge of a boundary layer: this thought experiment is visualised in *Fig.* 4.3.

Momentum

As a starting point, it is assumed that the vortex exchanges momentum with its environment by means of shear stresses. More precisely, it is assumed that the vortex exerts a shear stress upon the free-stream edge of the boundary layer which is proportional to its circulation, as can be inferred from *Eqn.* (3.83). Because the strain rate is, by definition, zero at the free-stream boundary of an undisturbed boundary layer, the shear stress is merely a function of the vortex. Consequently, the following can be hypothesised:

Hypothesis 4.2. The stabilisation of the boundary layer does not depend upon the momentum deficit of the boundary layer, but only upon the circulation of the vortex.

This is evidently tied to the presumption that the boundary layer remains in the same flow regime, i.e., that it either remains fully laminar or fully turbulent. The inclusion of transition would imply strong non-linearities in the behaviour of the boundary layer and is, therefore, not applicable to the following approach.

Furthermore, the above hypothesis may not be valid if the boundary layer is massively separated at the initial point of interaction, i.e., at the diffuser inlet. In this case the vortex would be partially or entirely submerged in the boundary layer, resulting in a significantly more complex interaction where the strain rate caused by the boundary layer would affect the vortex decay.

To transfer these rather general thoughts into a quantitative description, it is further assumed that the vortex trajectory is located just outside the boundary layer and that the vortex is in contact with the boundary layer at the radius of maximum shear stress. As can be derived from *Eqn.* (3.83), the strain rate and, therefore, shear stress reach their maximum at approximately $1.34\,\mathrm{r}_0$, which is assumed to be the distance between the vortex centre and the free-stream edge of the boundary layer. To calculate the shear stress, *Eqn.* (3.83) is—consistent with the method of BARDINA ET AL. (1982)—non-dimensionalised using the following transformations:

$$\Gamma_0{}^+ := \frac{\Gamma_0}{2\pi r_{\mathrm{Euler,in}}\,\mathcal{U}_{\infty,\mathrm{in}}} \tag{4.6}$$

for the circulation,

$$r^+ := \frac{r}{\mathcal{W}_{\mathrm{in}}} \tag{4.7}$$

for the radial coordinate,

$$t^+ := t\frac{\mathcal{U}_{\infty,\mathrm{in}}}{\mathcal{W}_{\mathrm{in}}} \tag{4.8}$$

for the time coordinate, and

$$\mathrm{Re}_{\ell_\mathrm{D}} = \frac{\mathcal{U}_{\infty,\mathrm{in}}\ell_\mathrm{D}}{\nu + \nu_{\mathrm{turb}}} \tag{4.9}$$

for the kinematic viscosity, where the molecular viscosity has been replaced by the sum of molecular and *turbulent viscosity* to express the effect of turbulence. According to HALL (1966), citing an unpublished analysis of literature data by OWEN (1964), the turbulent viscosity of trailing vortices correlates with their circulation:

$$\nu_{\mathrm{turb}} = C\sqrt{\Gamma\nu}, \tag{4.10}$$

where C is a non-dimensional constant with values reported between 0.21 and 0.63.

The resulting non-dimensional strain-rate distribution

$$S_{r\theta}{}^+ = \frac{\Gamma_0{}^+\mathrm{Re}_{\ell_\mathrm{D}}}{4\pi t^+}\left(1 + \frac{4t^+}{\mathrm{Re}_{\ell_\mathrm{D}} r^{+2}}\right)\mathrm{e}^{-\frac{\mathrm{Re}_{\ell_\mathrm{D}} r^{+2}}{4t^+}} - \frac{\Gamma_0{}^+}{\pi r^{+2}} \tag{4.11}$$

is used to calculate the non-dimensional shear-stress distribution, i.e.,

$$\tau_{r\theta}{}^+ = \frac{S_{r\theta}{}^+}{\mathrm{Re}_{\ell_\mathrm{D}}} \tag{4.12}$$

which is then expressed in terms of a non-dimensional shear velocity,

$$u_\tau{}^+ := -\,\mathrm{sgn}(\tau_{r\theta}{}^+)\,\sqrt{|\tau_{r\theta}{}^+|}, \tag{4.13}$$

where the density is omitted due to the assumption of incompressible flow and the use of non-dimensional quantities. The negative of the sign function is used in order to express the shear stress experienced from the boundary-layer reference frame. In analogy to *Eqn.* (3.69), a "vortex-friction" coefficient is defined as

$$C_{\mathrm{f},\Omega} := 2\kappa^2\left|u_\tau{}^+\right|u_\tau{}^+ \tag{4.14}$$

and subtracted from the right-hand side of *Eqn.* (3.71):

$$
\begin{aligned}
\frac{(1-h+C_2)+2B\,(2-2h+0.015/\Lambda)}{B\,(1-2B)}\frac{\mathrm{d}B}{\mathrm{d}{x_1}^+}-C_1\frac{\mathrm{d}\Lambda}{\mathrm{d}{x_1}^+}=\;&\frac{C_\mathrm{f}/2+\beta E^+}{B\,\mathcal{U}^+}\\
&+(2-2h+0.015/\Lambda)\,\frac{1}{\mathcal{U}^+}\frac{\mathrm{d}\mathcal{U}^+}{\mathrm{d}{x_1}^+}\\
&-(1-h)\,\frac{1}{{r_\mathrm{m}}^+}\frac{\mathrm{d}{r_\mathrm{m}}^+}{\mathrm{d}{x_1}^+}\\
&-c_\Omega C_{\mathrm{f},\Omega}\,,
\end{aligned}
\tag{4.15}
$$

where c_Ω is a calibration constant; the corresponding numerical value is given in *App.* A. Again, because the vortex-induced shear stresses appear as a constant inhomogeneous term in this ordinary differential equation, it can be inferred that the vortex circulation affects the stabilisation process linearly. Since the skin-friction term and vortex-stress term have opposite signs, it can be easily seen that the vortex acts in a stabilising manner:

Hypothesis 4.3. Shear stresses imposed by a vortex with a mathematically positive sense of rotation increase the boundary-layer stability in proportion to the vortex circulation.

Mass

Prompted by the entrainment mechanism drawing free-stream fluid into the boundary layer, the question arises whether similar processes occur on larger scales when macroscopic vortices are in play.

Cutler and Bradshaw (1993b) observed that a boundary layer in close proximity to longitudinal vortices experiences local separation of boundary-layer fluid in the upwash region with a subsequent increase in the boundary-layer thickness and a decrease in the skin-friction coefficient. The separated fluid is reported to be entrained into the vortex, thus reducing the vortex circulation. Cutler and Bradshaw (1993a) showed for a similar case—albeit with a greater distance between the vortex pair and boundary layer—an increase in the boundary-layer thickness in the upwash region without flow separation. The data provided for the skin-friction coefficient and momentum-thickness Reynolds number allow the estimation of a slight increase in the shape factor H in the upwash region using the following relationship by Ludwieg and Tillmann (1949):

$$
C_\mathrm{f}=0.246\cdot 10^{-0.678H}\mathrm{Re}_\vartheta^{-0.268}. \tag{4.16}
$$

The estimated increase in H would imply less resilience of the boundary layer against flow separation under a hypothetical adverse pressure gradient. Unfortunately, no such data are provided in the first case, where the vortices are convected more closely along the boundary layer.

The case presented by Cutler and Bradshaw (1993b) certainly differs significantly from the flows considered in this work, as the cited study considers a flow where the vortex axes and boundary-layer flow are aligned and the effects induced are oriented predominantly in the cross-wise direction. It does, however, suggest that the process of entrainment plays a role in vortex-induced changes in diffuser stability.

The effect of vortex-induced entrainment is assumed to be a function of the vortex-induced shear stress at the boundary-layer edge. It is added as an inhomogeneous term to the right-hand side of *Eqn.* (3.72), i.e.,

$$\frac{1}{B\,(1-2B)}\frac{\mathrm{d}B}{\mathrm{d}{x_1}^+} - \frac{1}{\Lambda\,(1-\Lambda)}\frac{\mathrm{d}\Lambda}{\mathrm{d}{x_1}^+} = E^+ - \frac{1}{{r_\mathrm{m}}^+}\frac{\mathrm{d}{r_\mathrm{m}}^+}{\mathrm{d}{x_1}^+} + c_E C_{\mathrm{f},\Omega}\,, \tag{4.17}$$

where c_E is a calibration constant; the corresponding numerical value is given in *App.* A. This leads to the following hypothesis:

Hypothesis 4.4. Entrainment of boundary-layer fluid into the vortex decreases the boundary-layer stability in proportion to the vortex circulation.

Again, this may not be valid in the case where a weak vortex encounters a massive boundary layer separation at the initial point of interaction.

Vortex decay
Beside the dissipation inherent to the LAMB–OSEEN vortex, it can be expected that the interaction with a boundary layer yields an intensified decay of the vortex. Thinking in terms of *Eqns* (4.15) and (4.17), this can be explained as follows:

Firstly, in order to transmit momentum to the boundary layer, the vortex must exert a force upon it. It follows from NEWTON's third law of motion that an equal and opposite force acts upon the vortex, thereby exerting a torque about its centre. Since this torque opposes the sense of rotation of the vortex, its circulation diminishes.

Secondly, the vortex entrains boundary-layer fluid if it passes closely enough. CUTLER AND BRADSHAW (1993b) explained that the boundary-layer vorticity is of the opposite sign compared to the vortex. As a result, the overall vorticity—and, *ergo,* circulation—of the vortex are reduced.

Since both forms of interaction are governed by shear stresses, it can be deduced that the vortex decay is also proportional to the shear stresses at the interface between the vortex and boundary layer. The shear stresses, in turn, are a function of the vortex circulation. Consequently, it is to be expected that the circulation decrease depends solely upon the circulation of the vortex. In the prediction method proposed, this is realised by reducing the vortex circulation at each solver step by

$$\mathrm{d}\Gamma = -2\pi r_{\tau=\max} c_{\mathrm{d}\Gamma} {u_\tau}^+ \tag{4.18}$$

where $c_{\mathrm{d}\Gamma}$ is, again, a calibration constant. The corresponding numerical value is given in *App.* A. This leads to the following statement:

Hypothesis 4.5. The vortex decay does not depend upon the momentum deficit of the boundary layer, but only upon the vortex circulation.

4.5. Vortex generation

The tip-leakage vortex, which was identified as the structure stabilising the boundary layer in previous works (see *Sec.* 2.1.4), is generated at the tip of a blade, akin to a trailing vortex generated at the tip of a wing (see *Sec.* 3.5). Its vorticity is a function of the span-wise decrease

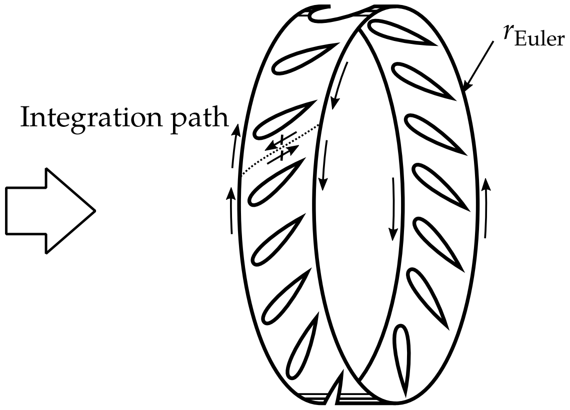

Figure 4.4.: Integration domain for blade-row circulation

in blade loading, i.e., in blade circulation (see *Sec.* 3.5); this reduces to a dependency upon the blade circulation if a constant aspect ratio and tip gap, as well as incompressible flow, are presumed. To relate the vortex generated to its stabilising influence on the boundary layer, three parameters can be identified which will be discussed below.

Vortex intensity
Using the non-dimensional circulation introduced in *Eqn.* (4.6), the following relationship is postulated:

$$\epsilon = f\left(\frac{\Gamma}{2\pi r_{\text{Euler}} u_x}\right). \tag{4.19}$$

Assuming constant density, the non-dimensional circulation may be understood as the ratio of the tangential momentum of the vortex to the axial momentum of the free stream and, by extension, the momentum deficit of the boundary layer of a given diffuser.

As indicated in *Fig.* 4.4, the circulation contained in the outflow from a blade row can be expressed purely as the difference between the absolute circumferential velocities at the inlet and outlet planes of the row (Schlichting and Truckenbrodt 2001) integrated along the entire circumference of the rotor. For the sake of simplicity, the circumference at the Euler radius is chosen here. This yields

$$\frac{\Gamma}{2\pi r_{\text{Euler}} u_x} = \frac{2\pi r_{\text{Euler}} \left(u_{\theta,1} - u_{\theta,2}\right)}{2\pi r_{\text{Euler}} u_x} = \frac{\Delta u_\theta}{u_x}. \tag{4.20}$$

By expanding *Eqn.* (4.20) with the rotor speed at the Euler radius, it follows that

$$\frac{\Delta u_\theta}{u_x} \cdot \frac{v_{\text{rot}}}{v_{\text{rot}}} = \frac{\Delta u_\theta}{v_{\text{rot}}} \cdot \frac{v_{\text{rot}}}{u_x} = \frac{\Psi}{\Phi} \tag{4.21}$$

where Ψ is the loading coefficient,

$$\Psi := \frac{\Delta u_\theta}{v_{\text{rot}}}, \tag{4.22}$$

and Φ is the flow coefficient,

$$\Phi := \frac{u_x}{v_{\text{rot}}}. \tag{4.23}$$

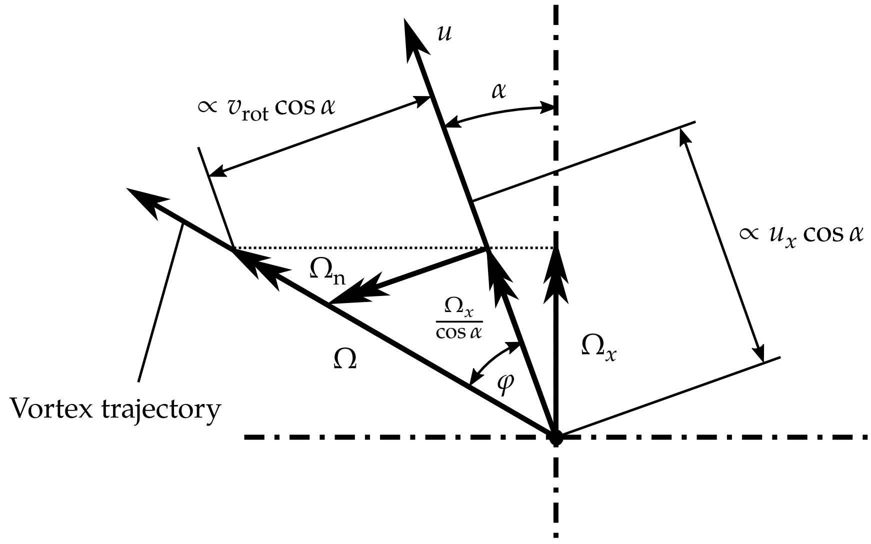

Figure 4.5.: Projection of axial vorticity onto the stream-normal direction

The posited relationship between the non-dimensional circulation and the non-dimensional term Ψ/Φ is strictly applicable to quantify the circulation of the tip-leakage vortices only if a highly idealised, inviscid flow is assumed where the vortices trail the blade tips as concentrated vortex lines. A proportionality between the blade circulation and the circulation of the tip-leakage vortex can, however, be expected as long as the span-wise aerodynamic blade-loading distribution remains unchanged. Certain circumstances, such as changes in the span-wise velocity distribution upstream of the blade row or partial flow separation on the blades at high incidence, may preclude this proportionality. Similarly, the effect of varying aspect ratios is not included in this relationship.

Vortex orientation

The above equation gives, by definition, the circulation in the outlet plane of the control volume shown in *Fig.* 4.4. It follows from Stokes' theorem that this circulation can be translated into a vorticity normal to the outlet plane. However, the vorticity component normal to the flow direction is relevant to the boundary-layer stabilisation.

Because the overall vorticity vector is presumably collinear with the vortex trajectory, two points on the vortex trajectory are considered which were generated with a time delay of Δt. The axial distance between the two points is evidently $\Delta_{\Omega,x} = u_x \Delta t$. The distance in the circumferential direction is $\Delta_{\Omega,\theta} = (|v_{\mathrm{rot}}| + |u_\theta|)\,\Delta t$. This is invariant with respect to the frame of reference.

A fluid element leaving the rotor, outside the vortex, for the same time span Δt, would still travel a distance of $\Delta_{\infty,x} = u_x \Delta t$ in the axial direction. The distance in the circumferential direction, however, would only be $\Delta_{\infty,\theta} = |u_\theta| \Delta t$. The ratio of $\Delta_{\infty,x}$ to $\Delta_{\infty,\theta}$, in turn, is determined by the absolute outflow angle α.

Figure 4.5 shows that the projection of the axial vorticity component Ω_x onto the absolute outflow angle is, therefore, $\Omega_x / \cos\alpha$. To obtain the vorticity component normal to the outflow, Ω_n, the angle φ between the vortex trajectory and the outflow direction must be determined:

$$\tan(\varphi) = \frac{v_\mathrm{rot}\cos\alpha}{u_x\cos\alpha} = \frac{v_\mathrm{rot}}{u_x} = \frac{1}{\Phi}. \tag{4.24}$$

It follows that

$$\Omega_\mathrm{n} = \frac{1}{\Phi\cos\alpha}\Omega_x. \tag{4.25}$$

The relationship between the flow coefficient and the vortex orientation assumes a constant circumferential angle of the vortex trajectory. In real diffuser flows, however, the streamwise deceleration of the flow will cause a certain amount of vortex bending, as expressed in *Eqn.* 3.85. Notwithstanding, it is assumed that the variation of this effect is rather small for a given diffuser and that the initial orientation dictates the subsequent trajectory, for the most part. Regarding the comparison of diffusers with different opening angles, the effect of vortex bending will be absorbed in the sensitivity of the diffuser effectiveness towards the diffuser opening angle.

Vortex duty cycle

Unlike posited in *Ass.* 1.1, the actual stabilisation process is not steady, since the boundary layer experiences stabilisation only when a vortex passes by. In this simplified model, however, the flow can be regarded as *quasi-steady* due to the periodic nature of the stabilising vortices. The stabilisation must then be related to parameters describing the periodicity of the stabilising vorticies.

The term *duty cycle* is adapted from the field of electrical engineering*, where a *duty cycle* or *duty factor* is understood as the fraction of a signal period during which a signal can be measured. Similarly, in the context of this work, the *vortex duty factor* refers to the fraction of a blade passing during which a vortex core passes by a stationary point in the diffuser boundary layer. It is, thus, equivalent to the ratio of the diameter of a vortex core to the blade pitch ℓ_p. Expressed in time scales, this gives

$$F := \frac{\mathcal{T}_\Omega}{\mathcal{T}_\mathrm{BP}} = \frac{v_\mathrm{rot}}{\ell_\mathrm{p}}\frac{\ell_\Omega}{u_x} = \frac{v_\mathrm{rot}n}{2\pi r_\mathrm{Euler}}\frac{\ell_\Omega}{u_x}. \tag{4.26}$$

In wind-tunnel experiments, McAlister and Takahashi (1991) measured that the trailing vortex of a NACA-0015 half wing increased almost quadratically with increasing chord length. Because the experiment was performed for a single, free-standing half wing and because the authors kept a constant thickness-to-chord ratio, it is questionable whether these results are quantitatively applicable to the case discussed here; they do however show that a positive relationship exists. Nevertheless, in the absence of more specific data, a linear dependency between the vortex-core diameter and the characteristic length is assumed, i.e.,

$$\ell_\Omega \propto \ell_\mathrm{ch}, \tag{4.27}$$

which yields

$$F = \frac{v_\mathrm{rot}n\ell_\mathrm{ch}}{2\pi r_\mathrm{Euler}u_x} \tag{4.28}$$

---

*The term is also used in the context of intermittent flow actuation, e.g., by means of pulsed jets.

where n is the blade count and where the chord was chosen as the characteristic length. This is equivalent to the definition of the non-dimensional blade-passing frequency,[*]

$$F = \frac{f_{\mathrm{BP}} \ell_{\mathrm{ch}}}{u_x} = \frac{n N \ell_{\mathrm{ch}}}{u_x}, \tag{4.29}$$

where N is the rotor speed.

The above derivations of the vortex duty factor require the assumption that the vortex-core diameter is independent from the blade pitch and the aspect ratio. The vortex-core diameter is, however, related to the aspect ratio and aerodynamic blade loading (see McAlister and Takahashi 1991), the latter of which changes with varying pitch-to-chord ratio (see Traupel 2001). While the impact of an altered blade loading is, at least partially, expressed by the loading coefficient, the impact of a variation in the aspect ratio is not. Because the data which will be used to evaluate the validity of the theory derived in this chapter were all collected for a constant aspect ratio, this parameter is not included here.

Vortex characterisation
By multiplying the vortex parameters derived in *Eqns* (4.21), (4.25), and (4.29), which express the respective contributions of the vortex intensity, orientation, and duty cycle to the boundary-layer stabilisation process, the following *stabilisation number* Σ is defined:

$$\boxed{\Sigma := \frac{\Psi F}{\Phi^2 \cos \alpha}.} \tag{4.30}$$

Due to the relationships between the individual events in the diffuser-stabilisation process, which are predicted to be linear, the following hypothesis can be proposed:

Hypothesis 4.6. The diffuser effectiveness ϵ increases linearly with the stabilisation number Σ.

The corresponding correlation is, therefore, expected to assume the following general form, where the subscript "ref" indicates values at the reference operating point, e.g., for $\Sigma_{\mathrm{ref}} = 0$:

$$\Delta\epsilon = \epsilon - \epsilon\left(\Sigma_{\mathrm{ref}}\right) = a_{\Sigma}\Sigma. \tag{4.31}$$

Several further parameters, beside the ones already named in the respective sections, will likely impact the relationship posited—the Reynolds and Mach number being the most prominent ones. The diffuser data presented later in this work, however, were all collected for a narrow range of both parameters, thus, precluding the assessment of this assertion.

4.6. Total-pressure losses

As stated initially, it is in the interest of turbomachinery designers to reduce the total-pressure losses generated in the diffuser. For a proper comparison of the losses generated in various test cases, it is necessary to include the influence of several phenomena which have not yet been considered in this work. These phenomena represent inflow inhomogeneities in

---

[*] This non-dimensional parameter is also often referred to as the Strouhal number.

general and wakes in particular. To achieve this, the overarching approach will be to use an aerodynamically unloaded reference—which does not exhibit secondary flow—and to *extrapolate* the total-pressure losses to the operational conditions of interest. It must be noted that the following derivations of the extrapolation function are likely to be highly rotor-specific and ignore the probable contributions of varying Reynolds and Mach numbers. The intention is, however, to demonstrate that such an approach towards loss prediction at the design stage of diffusers is possible.

The first, most obvious correction follows from the definition of the total-pressure loss coefficient (see *Eqn.* 1.27): the total-pressure losses scale with the dynamic pressure at the diffuser inlet, i.e.,

$$\Delta p_{\mathrm{tot}} \propto \frac{\rho}{2} u_{\mathrm{in}}^2. \tag{4.32}$$

The second correction expresses the presumably linear relationship between the wake losses and the characteristic length as well as the number of blades, here expressed as the chord-to-pitch ratio, i.e., the *solidity* of the rotor:

$$\Delta p_{\mathrm{tot}} \propto \frac{\ell_{\mathrm{ch}}}{\ell_{\mathrm{p}}}. \tag{4.33}$$

The third correction to be applied is related to the diffuser swirl angle α. It is intuitive that the dissipative processes occurring in the diffuser are likely to scale linearly with the flow-path length travelled by the fluid. Any deviation from an axial inflow leads to an increase in flow-path length, as expressed by

$$\Delta p_{\mathrm{tot}} \propto \frac{1}{\cos\alpha}. \tag{4.34}$$

Of course, this relationship is bound to flatten for very long diffusers where a homogeneous, mixed-out flow is achieved.

The fourth and final correction is somewhat less self-evident; it is also perhaps the most rotor-specific relationship proposed in this section and attempts to predict the breadth and depth of the wakes from design parameters. For most aerofoils, a change in the rotor incidence increases the area obstructed by the blades and is, at the same time, likely to yield thicker boundary layers (Mimic et al. 2018b). A change in incidence is indicated by a change in the flow coefficient for a given rotor geometry. It follows that

$$\Delta p_{\mathrm{tot}} \propto \left|\Phi - \Phi_{\mathrm{design}}\right|. \tag{4.35}$$

The above relationships are used to define the following *extrapolation factor* Ξ:

$$\boxed{\Xi := \frac{\frac{\rho}{2} u_{\mathrm{in}}^2}{\frac{\rho_{\mathrm{ref}}}{2} u_{\mathrm{in,ref}}^2} \frac{\ell_{\mathrm{ch}}/\ell_{\mathrm{p}}}{\ell_{\mathrm{ch,ref}}/\ell_{\mathrm{p,ref}}} \frac{\cos\alpha_{\mathrm{ref}}}{\cos\alpha} \left[1 + \frac{\left|\Phi - \Phi_{\mathrm{design}}\right|}{\Phi_{\mathrm{ref}}}\right].} \tag{4.36}$$

If the tip-leakage vortices are able to stabilise the boundary layer, it is to be expected that the losses related to the boundary-layer will decrease. An increase in the stabilisation number, however, is in most cases tied to an increased intensity of the tip-leakage vortices. Consequently, the vortex-induced losses should increase. At this point, it is not predictable whether the reduction in the boundary-layer losses or the increase in vortex losses will prevail. For now, however, the more optimistic hypothesis is chosen:

Hypothesis 4.7. The total-pressure loss coefficient ζ of the diffuser decreases linearly with an increasing product of the extrapolation factor and the stabilisation number, i.e., $\Xi\Sigma$ with regard to an extrapolated reference $\Xi\zeta_{\mathrm{ref}}$.

The expected correlation can be given the following general form:

$$\Delta_{\Xi}\zeta = \zeta - \Xi\zeta_{\mathrm{ref}} = a_{\Xi\Sigma}\Xi\Sigma. \tag{4.37}$$

For the sake of convenience, $\Delta_{\Xi}\zeta$ and $\Xi\Sigma$ will be referred to as the *extrapolated change in total-pressure losses* and *extrapolated stabilisation number,* respectively.

Chapter 5.

Method

5.1. Validation approach

The data-acquisition process for the validation of the theory proposed can be subdivided into several key steps. Generally speaking, *Hyps* 4.6 and 4.7 are to be tested using experimental data. Additionally, partially scale-resolving simulations using the scale-adaptive simulation (SAS) method by MENTER AND EGOROV (2010) were conducted and validated with the same experimental data (MIMIC ET AL. 2018a). The numerical model was then adapted to suit different diffuser half-opening angles in order to test the theory beyond the experimental data available. A chronological enumeration of the steps is given below.

1. MIMIC ET AL. (2018a): Experimental data were collected from experiments conducted previously on the *low-speed axial-diffuser test rig* of the INSTITUTE OF TURBOMACHINERY AND FLUID DYNAMICS at LEIBNIZ UNIVERSITÄT HANNOVER by KUSCHEL (2014)* for a diffuser with a half-opening angle of 15°. These published data contain information about the mass-flow rate, rotor speed, flow coefficient of the rotor, and swirl angle at the diffuser inlet as well as static-pressure recovery in the diffuser control domain. The input quantities mass-flow rate, rotor speed, flow coefficient, and swirl angle were used to estimate the loading coefficient and non-dimensional blade-passing frequency of the rotor. The stabilisation number was determined from the loading coefficient, flow coefficient, and non-dimensional blade-passing frequency. Additionally, the ideal static-pressure recovery coefficients and corresponding values of the diffuser effectiveness were calculated for each data point using the diffuser opening angle and inlet swirl angle. A correlation between the values of the stabilisation number and effectiveness was derived.

2. MIMIC ET AL. (2018a): Numerical flow simulations were conducted within a range of the stabilisation number comparable to the experiments using the partially scale-resolving scale-adaptive simulation (SAS) approach to validate the numerical flow prediction and confirm the correlation derived from experimental data.

3. MIMIC ET AL. (2018a): Supplemental experimental data were provided to further increase the validity of the correlation.

4. MIMIC ET AL. (2018b): A correlation between the stabilisation number and extrapolated total-pressure loss coefficient† was derived for experimental and numerical data.

---

*see also KUSCHEL ET AL. (2015)

†MIMIC ET AL. (2018b) referred to this as the *rectified total-pressure loss coefficient*.

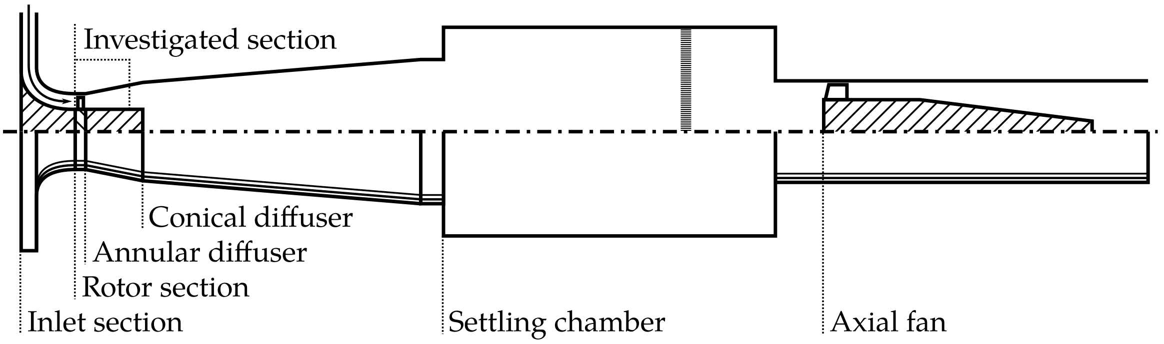

Figure 5.1.: Low-speed axial-diffuser test rig at the Institute of Turbomachinery and Fluid Dynamics (simplified)

The measurements were taken during the same experiments as the supplemental experimental data mentioned previously and presented by Mimic et al. (2018a).

5. Mimic et al. (2018c): Older experimental data from Sieker (2010)* were used to further validate the correlation for a half-opening angle of 15° and expand the correlation to a half-opening angle of 20°.

6. Mimic et al. (2018c): Numerical flow simulations were conducted for half-opening angles of 5°, 10°, and 12°. All diffusers simulated exhibit a less severe aerodynamic loading than the 15° diffuser. Their behaviour is, therefore, less critical to predict numerically than for the validated 15° simulations. Simulations of the 20° diffuser did not reach satisfying convergence due to full separation at the casing.

7. Mimic et al. (2019): The numerical data set used in Mimic et al. (2018c) was evaluated further together with some additional simulation results and correlations between the stabilisation number and extrapolated total-pressure loss coefficient† were derived for the half-opening angles 5°, 10°, and 12°.

8. Present work: The present work uses solely the experimental data collected by Sieker (2010)*, Kuschel (2014)‡, Mimic et al. (2018a), and Mimic et al. (2018b) as well as the numerical data set generated successively by Mimic et al. (2018a), Mimic et al. (2018b), Mimic et al. (2018c), and Mimic et al. (2019). Because the numerical data set was expanded gradually, the simulations will be referred to in the following simply as numerical data or simulation data. All data have been reassessed. Several smaller inaccuracies present in prior publications regarding the chord length and positions of measurement planes have been corrected. The data have been correlated using the improved formulations of Σ and $\Xi\Sigma$ given in *Eqns* (4.30) and (4.36).

---

[*] see also Sieker and Seume (2008a)

[†] Mimic et al. (2019) referred to this as the *rectified total-pressure loss coefficient*.

[‡] see also Kuschel et al. (2015)

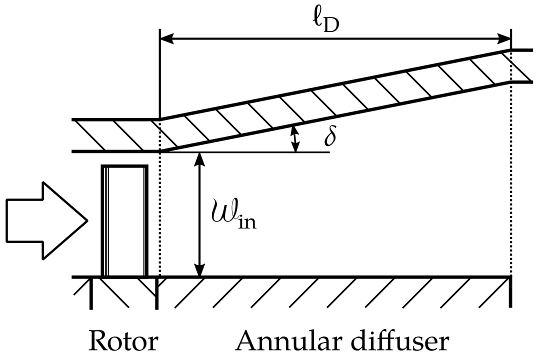

Figure 5.2.: Test section comprising the rotor and annular diffuser

5.2. Experimental setup

All experiments were conducted on the *low-speed axial-diffuser test rig* at the Institute of Turbomachinery and Fluid Dynamics at Leibniz Universität Hannover. The test rig was initially designed by Fleige (2002)* and represents a model of a typical exhaust diffuser of a heavy-duty gas turbine at a scale of approximately 1:10. Sieker (2010)† upgraded the test rig for a rotor upstream of the diffuser in order to generate turbine-like wake and secondary-flow structures at the diffuser inlet. A schematic of the test rig in its present configuration, which is the one investigated in this work, is shown in *Fig.* 5.1. It comprises the following sub-assemblies.

Inlet section
Ambient air enters the intake in a radially inward direction, where it passes an array of 30 adjustable sheet-metal swirl generators. The swirl generators were used in past studies. In the experiments used in this work, however, all swirl generators were in the neutral position to ensure swirl-free inflow. The flow is subsequently redirected into the axial direction before entering the rotor.

Rotor section
The rotor section features constant radii for the hub and casing. The rotor used in this work is equipped with either 15 or 30 blades with a span of 99.3 % of the channel height and an aspect ratio of approximately 4. The blades are unshrouded and consist of NACA-0020 aerofoils. The stagger angle varies across the blade span in order to satisfy incidence-free inflow at the aerodynamic design point. Together with the symmetric shape of the NACA-0020 aerofoil, this means that the blades exhibit no aerodynamic loading—and consequently no considerable secondary flow—under design conditions. The rotor shaft is coupled to an electric motor-generator with a maximum power of 4 kW, which operates between 100 RPM and 3000 RPM. Together with the symmetric blades, this allows the generation of both compressor and turbine-like outflow. In this work, only turbine-specific operating points are considered. The rotor section is described in greater detail by Sieker (2010).†

---

*see also Fleige and Riess (2001)

†see also Sieker and Seume (2008a)

Annular diffuser
Upon exiting the rotor section, the flow enters an annular diffuser. The annular diffuser is the component investigated in this work and has an area ratio of 1.78. Note that the control domain, over which static-pressure recovery and total-pressure losses are evaluated, ranges from $0.085\ell_{\mathrm{D}}$ to $0.96\ell_{\mathrm{D}}$. Diffusers with half-opening angles of 15° and 20° were used. Due to the fixed area ratio, the 15° diffuser has a non-dimensional length of 2.13, whereas the 20° diffuser has a non-dimensional length of 1.55. The investigated section, comprising the rotor and annular diffuser is shown in *Fig.* 5.2. More detailed information is given by KUSCHEL (2014).*

Conical Diffuser
The annular diffuser is followed by a conical diffuser with a half-opening angle of 5°. The abrupt end of the hub at the outlet of the annular diffuser causes a jump in cross-sectional area. The area ratio of the conical diffuser is, therefore, 2.88 and its non-dimensional length is 10.5. The conical diffuser is not considered in this work. However, more detailed information is given by KUSCHEL (2014).*

Settling chamber
A settling chamber with a flow straightener is located downstream of the conical diffuser. This eliminates any residual swirl before the flow reaches the subsequent axial fan.

Axial fan
The mass flow is provided by an axial fan located in the outflow section of the test rig. The fan has a power of 37 kW. It reaches a volume-flow rate of $8\,{}^{\mathrm{m}^3}/_{\mathrm{s}}$ and a total-pressure rise of approximately 2800 Pa near the point of peak efficiency.

Pneumatic measurements
Pneumatic measurements were conducted at the respective inlet and outlet planes of the annular-diffuser control domain ($0.085\ell_{\mathrm{D}}$ and $0.96\ell_{\mathrm{D}}$) using radial probe traverses in order to determine the swirl angle, static-pressure recovery, and total-pressure loss coefficient. SIEKER (2010)† and KUSCHEL (2014)* used three-hole probes, whereas MIMIC ET AL. (2018a) and MIMIC ET AL. (2018b) used five-hole probes.

5.3. Numerical model

The simulations used in this work were conducted using the flow solver TRACE 8.2.417 (Turbomachinery Research Aerodynamic Computational Environment), which is an ongoing development by the German Aerospace Center (DLR, *Deutsches Zentrum für Luft- und Raumfahrt*). The details of the numerical model shall be covered below.

5.3.1. Governing equations

TRACE solves the fully three-dimensional, compressible continuity equation, NAVIER–STOKES equations, and the energy equation (see *Sec.* 3.1.6) together with additional scalar transport

---

[*] see also KUSCHEL ET AL. (2015)

[†] see also SIEKER AND SEUME (2008a)

equations for, e.g., turbulent quantities in a rotating frame of reference. In their strong conservative form, the governing equations may be formulated as

$$\frac{\partial \mathbf{U}_{\text{rel}}}{\partial t} + \boldsymbol{\nabla} \cdot \mathbf{F}_{\text{rel}} = \mathbf{Q}_{\text{rel}}, \tag{5.1}$$

where $\mathbf{U}_{\text{rel}}$, $\mathbf{F}_{\text{rel}}$, and $\mathbf{Q}_{\text{rel}}$ represent the respective vectors of the state variables, fluxes, and source terms in the rotating frame of reference. For the transport of mass, momentum and energy, they are defined as

$$\mathbf{U}_{\text{rel}} := \begin{pmatrix} \rho \\ \rho \mathbf{u}_{\text{rel}} \\ \rho e_{\text{tot,rel}} \end{pmatrix}, \tag{5.2}$$

$$\mathbf{F}_{\text{rel}} := \begin{pmatrix} \rho \mathbf{u}_{\text{rel}} \\ \rho \mathbf{u}_{\text{rel}} \otimes \mathbf{u}_{\text{rel}} + p\mathbf{I} - \boldsymbol{\tau} \\ \mathbf{u}_{\text{rel}} \left(\rho e_{\text{tot,rel}} + p \right) - \boldsymbol{\tau} \mathbf{u}_{\text{rel}} + \lambda \boldsymbol{\nabla} T \end{pmatrix}, \tag{5.3}$$

$$\mathbf{Q}_{\text{rel}} := \begin{pmatrix} 0 \\ \mathbf{f}_{\text{c}} + \mathbf{f}_{\text{C}} \\ 0 \end{pmatrix}. \tag{5.4}$$

Here, $e_{\text{tot,rel}}$ is the total specific energy relative to the rotating reference frame,

$$e_{\text{tot,rel}} = e + \frac{1}{2} \mathbf{u} \cdot \mathbf{u} - \frac{1}{2} \mathbf{R}_{\text{sys}} \cdot \mathbf{R}_{\text{sys}} \cdot \mathbf{r} \cdot \mathbf{r}, \tag{5.5}$$

where e is the specific internal energy of the fluid. The source term $\mathbf{f}_{\text{c}}$ denotes the volume-specific centrifugal force,

$$\mathbf{f}_{\text{c}} = -\rho \, \mathbf{R}_{\text{sys}} \times \left(\mathbf{R}_{\text{sys}} \times \mathbf{r} \right), \tag{5.6}$$

where the vector $\mathbf{R}_{\text{sys}}$ represents the angular velocity of the reference frame and $\mathbf{r}$ a radial vector. Likewise, $\mathbf{f}_{\text{C}}$ denotes the volume-specific CORIOLIS force,

$$\mathbf{f}_{\text{C}} = -2\rho \, \mathbf{R}_{\text{sys}} \times \mathbf{u}_{\text{rel}}, \tag{5.7}$$

which expresses the conservation of angular momentum as a fictitious force in the rotating frame of reference. A detailed discussion of the numerical intricacies of TRACE is given by MORSBACH (2016).

The gas is assumed to be calorically perfect (see *Sec.* 3.1.4). Its molecular viscosity μ_{mol} is calculated from SUTHERLAND's law (see *Eqn.* 3.39).

5.3.2. Favre decomposition

Equation (5.1) would, if solved using a sufficiently fine mesh, resolve all scales of turbulence. While this approach, termed *direct numerical simulation* (*DNS*), represents the closest approximation to the actual flow physics, it is also computationally highly expensive due to the fine spatial and temporal resolution required.

To reduce computational cost, any dependent flow variable ϕ can be decomposed into a mean and fluctuating component,

$$\phi \equiv \widetilde{\phi} + \phi'', \tag{5.8}$$

where $\widetilde{\phi}$ represents a density-weighted time average, i.e.,

$$\widetilde{\phi} := \frac{\int_{\Delta t} \rho\phi \mathrm{d}t}{\int_{\Delta t} \rho \mathrm{d}t}. \tag{5.9}$$

This so-called Favre decomposition can be applied to the governing equations. The Favre-averaged continuity equation, i.e.,

$$\frac{\partial\overline{\rho}}{\partial t} + \boldsymbol{\nabla}\cdot\left(\overline{\rho}\widetilde{\mathbf{u}}\right), \tag{5.10}$$

can be expressed purely in terms of average quantities, where the overline denotes a time average. In the case of the Favre-averaged Navier–Stokes equations, shown here in vector notation for a resting reference frame for better readability, i.e.,

$$\frac{\partial(\overline{\rho}\widetilde{\mathbf{u}})}{\partial t} + \boldsymbol{\nabla}\cdot\left(\overline{\rho}\widetilde{\mathbf{u}}\otimes\widetilde{\mathbf{u}}\right) = -\boldsymbol{\nabla}\overline{p} + \boldsymbol{\nabla}\cdot\left[\overline{\boldsymbol{\tau}} - \overline{\rho\mathbf{u}''\otimes\mathbf{u}''}\right], \tag{5.11}$$

the decomposition gives rise to an the additional term, $-\overline{\rho\left(\mathbf{u}''\otimes\mathbf{u}''\right)}$, on the right-hand side of the equation, where the velocity fluctuations act as an *apparent-stress tensor*. This will be discussed in the following section. The energy equation is not shown here, because its contribution is negligible at the low Mach numbers investigated in this work. However, similar terms arise there due to the contribution of the velocity fluctuations.

Technically, the terms Reynolds decomposition and unsteady Reynolds-averaged Navier–Stokes (URANS) equations are used when constant density is assumed. Nevertheless, approaches using both the unsteady Favre-averaged and unsteady Reynolds-averaged Navier–Stokes equations are commonly referred to as URANS approaches.

5.3.3. Turbulence model

The Favre decomposition yields the term $-\overline{\rho\left(\mathbf{u}''\otimes\mathbf{u}''\right)}$ on the right-hand side of *Eqn.* (5.11). These *apparent stresses* are a result of the correlation between the different components of the velocity fluctuations and represent the contribution of turbulence. They are commonly referred to as Reynolds stresses with the Reynolds-stress tensor

$$\boldsymbol{\tau}' := -\overline{\rho\left(\mathbf{u}''\otimes\mathbf{u}''\right)}. \tag{5.12}$$

Due to the Reynolds-stress tensor, *Eqn.* (5.11) contains more dependent variables than equations, which means that the system is not *closed.* Hence, a *closure* is required in order to solve the system.

Boussinesq

Boussinesq (1903) assumed an analogy between the momentum exchange in turbulent motion and the momentum exchange on molecular scales (see *Sec.* 3.1.5). Therefore, he hypothesised the existence of a *turbulent viscosity,* often called the *eddy viscosity,* which can be used to construct the Reynolds-stress tensor in a similar manner to *Eqn.* 3.16:

$$\boldsymbol{\tau}' = \mu_{\mathrm{turb}}\left[\left(\mathbf{u}\otimes\boldsymbol{\nabla}\right) + \left(\boldsymbol{\nabla}\otimes\mathbf{u}\right) - \frac{2}{3}\boldsymbol{\nabla}\cdot\mathbf{u}\mathbf{I}\right] + \frac{2}{3}\rho k\mathbf{I}. \tag{5.13}$$

Shear-stress–transport model

The use of Boussinesq's assumption shifts the problem of determining the Reynolds-stress tensor to that of determining the turbulent viscosity. Several approaches to predicting the turbulent viscosity, so-called *turbulence models*, of varying complexity are found in the literature. In an industrial context, two-equation linear eddy-viscosity turbulence models represent the most widely used class of these approaches. This is because they combine low additional computational effort and high numerical stability with predictions which are often sufficiently precise for technical applications.

The *k-ω shear-stress–transport* (*SST*) turbulence model by Menter et al. (2003)* is probably the most popular among these two-equation models. It comprises two partial differential transport equations:

$$\frac{\partial(\rho k)}{\partial t} + \nabla\cdot(\rho k\mathbf{u}) = \tilde{\mathscr{P}}_k - \beta^*\rho\omega k + \nabla\cdot\left[(\mu + \sigma_k\mu_{\mathrm{turb}})\,\nabla k\right], \tag{5.14}$$

$$\begin{aligned}\frac{\partial(\rho\omega)}{\partial t} + \nabla\cdot(\rho\omega\mathbf{u}) = {} & \frac{\rho\alpha}{\mu_{\mathrm{turb}}}\tilde{\mathscr{P}}_k - \beta^*\rho\omega^2 + \nabla\cdot\left[(\mu + \sigma_\omega\mu_{\mathrm{turb}})\,\nabla\omega\right] \\ & + 2\,(1 - F_1)\,\frac{\rho\sigma_{\omega,2}}{\omega}\left[\nabla k\cdot\nabla\omega\right].\end{aligned} \tag{5.15}$$

Equation (5.14) describes the transport of the turbulent kinetic energy k in terms of production, destruction, and diffusion, whereas *Eqn.* (5.15) transports the specific turbulence-dissipation rate ω. The *cross-diffusion term,* i.e., the last term on the right-hand side of *Eqn.* (5.15), enhances the prediction capabilities in the free stream. The turbulent viscosity is then approximately determined by

$$\mu_{\mathrm{turb}} \approx \frac{\rho k}{\omega}; \tag{5.16}$$

the exact calculation procedure including limiters and further details of the model and its calibration are given in *App.* B.

Scale-adaptive simulations

Drechsel et al. (2015) showed that, for the same test case used in the present work, a simple RANS or URANS approach using the k-ω SST model does not predict the diffuser flow accurately. Likewise, Drechsel et al. (2016) demonstrated that the same approach does not capture the apparent stresses produced in the tip-leakage vortex sufficiently well. They showed, however, that in both cases the *scale-adaptive simulation* (*SAS*) method by Menter and Egorov (2010) produced satisfactory results.

The SAS method is not a stand-alone turbulence model, but rather modifies existing turbulence models. It is usually applied in addition to the k-ω SST model, in which case it is referred to as the SST-SAS model. The SST-SAS model is classified by Fröhlich and von Terzi (2008) as a second-generation URANS (2G-URANS) model, as it allows the partial resolution of turbulent structures. In order to achieve this, the following source term is added to the right-hand side of the ω equation (*Eqn.* 5.15) of the k-ω SST model:

$$\mathscr{P}_{\mathrm{SAS}} := \max\left\{\rho\zeta_2 S^2\left(\frac{\ell_{\mathrm{turb}}}{\ell_{\mathrm{vK}}}\right)^2 - C_{\mathrm{SAS}}\frac{2\rho k}{\sigma_\Phi}\max\left[\frac{1}{k^2}\,(\nabla k\cdot\nabla k)\,;\frac{1}{\omega^2}\,(\nabla\omega\cdot\nabla\omega)\right];0\right\} \tag{5.17}$$

---

*The model was first published by Menter (1994).

where

$$S := \sqrt{2}\,\|\mathbf{S}\|_{\mathrm{F}} = \sqrt{2\mathbf{S} : \mathbf{S}}. \tag{5.18}$$

The essential term in *Eqn.* (5.17) is

$$\left(\frac{\ell_{\mathrm{turb}}}{\ell_{\mathrm{vK}}}\right)^2$$

where

$$\ell_{\mathrm{vK}} \approx \kappa \frac{\|(\mathbf{u} \otimes \boldsymbol{\nabla})\|_{\mathrm{F}}}{\|\boldsymbol{\nabla}^2 \mathbf{u}\|_2} \tag{5.19}$$

is a three-dimensional formulation of the von Kármán length scale, with κ being the von Kármán constant, and where

$$\ell_{\mathrm{turb}} \propto \frac{\sqrt{k}}{\omega} \tag{5.20}$$

represents the turbulence length scale. The exact definitions including limiters and calibration constants are given in *App.* C.

The von Kármán length scale quantifies the ratio of the gradient to the vector Laplacian of a velocity field and gives a local estimate of the characteristic length of inhomogeneous flow features. Menter and Egorov (2010) recognised these inhomogeneous flow features as potentially unsteady and argued that they should not be suppressed by an increase in the turbulent viscosity, as would be the case with conventional RANS or URANS models.

An increase in the ratio of ℓ_{turb} to ℓ_{vK} generally causes an increase in the SAS source term $\mathscr{P}_{\mathrm{SAS}}$. This, in turn, increases the specific turbulence dissipation rate ω and, per *Eqn.* (5.16), reduces the turbulent viscosity. This facilitates the development of tip-leakage vortices and massive flow separations, among other features.

5.3.4. Discretisation

In order to solve the governing equations numerically, it is necessary that they undergo a temporal and spatial discretisation. All simulations were conducted using a *finite-volume method,* which is facilitated by the strong conservative form of the governing equations used in TRACE: the integrated divergence of the flux-vector field, $\boldsymbol{\nabla} \cdot \mathbf{F}$, for a given cell, with the volume $\mathcal{V}$ enclosed by the surface $\partial\mathcal{V}$, can be expressed as the summation of all fluxes across the cell boundaries by applying the *divergence theorem:*

$$\iiint_{\mathcal{V}} \boldsymbol{\nabla} \cdot \mathbf{F} \,\mathrm{d}V = \oiint_{\partial\mathcal{V}} \mathbf{F} \cdot \mathbf{n} \,\mathrm{d}A. \tag{5.21}$$

The time derivative was discretised using a *second-order accuracy Euler backward scheme.* The inviscid fluxes were evaluated using a blended *implicit second-order accuracy differencing scheme;* they were calculated as a weighted sum of a central and upwind differencing scheme using the blending procedure developed by Strelets (2001):

$$\mathbf{F}_{\mathrm{inviscid}} = (1 - \sigma)\,\mathbf{F}_{\mathrm{central}} + \sigma \mathbf{F}_{\mathrm{upwind}} \tag{5.22}$$

where the blending function σ is essentially determined by the ratio of the local cell size to another characteristic turbulence length scale. As a result, the solver assumes a predominantly central differencing scheme in typically SAS-dominated regions in order to reduce

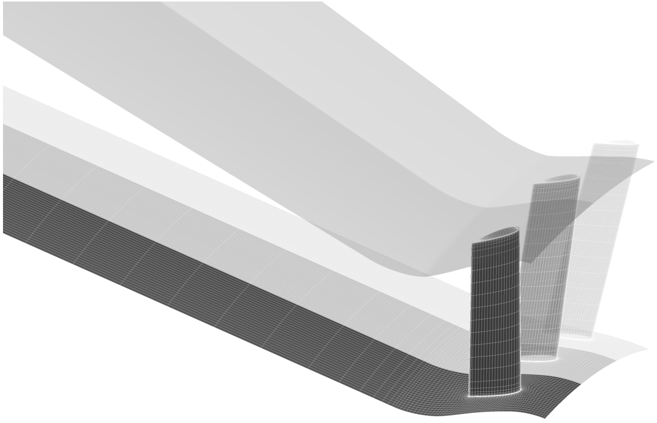

Figure 5.3.: Computational domain: example 15°; with additional passages for better orientation (Mimic et al. 2018c)

numerical diffusivity, whereas it employs a mostly upwind differencing scheme in other flow regions. Further details of the blending procedure are given in *App.* D.

The state variables were calculated using a *third-order accuracy monotonic upstream-centered scheme for conservation laws* (*MUSCL*) with a *van Albada square limiter* to increase numerical robustness. The discretised governing equations were solved using an *incomplete lower-upper* (*ILU*) *factorisation* method.

5.3.5. Computational domain

The numerical domain comprises a single rotor pitch with a NACA-0020 blade and a subsequent annular diffuser. *Figure* 5.3 shows the computational domain of the 15° diffuser with two additional passages for better orientation. The domain inlet is located approximately one axial chord length upstream of the blade leading edge; the resulting circumferential inhomogeneity of the inlet flow field is negligible for this choice of upstream extent of the computational domain. The blade pitch was varied to emulate blade counts of 25, 30, and 40 blades. Diffusers with half-opening angles of 5°, 10°, 12°, and 15° were simulated. The diffuser section is slightly longer than in the experimental set-up and extends into a coarsened straight outlet section. The coarse mesh in the outlet section acts as a buffer layer and prevents oscillations from reaching the outlet to increase numerical stability. Further improvements in the numerical stability were achieved by simulating the entire domain in a rotating frame of reference, thereby avoiding an interface between the rotor and diffuser.

The meshes consist of between 1.7×10^6 and 2.5×10^6 cells, depending upon the pitch and diffuser opening angle. Drechsel et al. (2015) presented a detailed grid-convergence study for the 15° test case using the k-ω SST model. Compared to Drechsel et al. (2015), the meshes were refined in the casing region to ensure better capturing of the tip-leakage vortex and flow separation. The significantly less severe—or even non-existent—flow separation with shallower opening angles leads to the conclusion that all meshes used satisfy the grid-quality requirements.

The numerical evaluation planes correspond to the measurement planes used in the experiment ($0.085\ell_D$ and $0.96\ell_D$). The position of the outlet plane was varied in a separate study.

Chapter 6.

Evidence

In this chapter, several pieces of evidence for the hypotheses stated in the previous chapter will be reviewed. The aim is to test the validity of the theory proposed. The validation approach shall be introduced in the following section.

6.1. Validation

The hypotheses derived in *Chap.* 4 will be tested in this section using the experimental and numerical data introduced in *Sec.* 5.1. The hypotheses will be approached in the predominantly reverse order, starting with the most general statements.

6.1.1. Diffuser effectiveness

Hypothesis 4.6 postulates the existence of a linear relationship between the stabilisation number Σ (see *Eqn.* 4.30) and the diffuser effectiveness.

Fifteen degrees
The diffuser effectiveness and stabilisation number were evaluated for one numerical and three experimental diffuser test cases with a half-opening angle of 15°. The results are plotted in *Fig.* 6.1, showing the absolute increase in diffuser effectiveness $\Delta\epsilon$ compared to the reference case with an aerodynamically unloaded rotor, i.e., $\Sigma = 0$ (see *Eqn.* 4.31). As can be seen, both the experimental and numerical data are represented well by the linear correlation

$$\Delta\epsilon = 1.90\Sigma, \qquad R^2 = 0.92 \tag{6.1}$$

where $R^2 = 0.92$ is the *coefficient of determination* achieved by the linear regression. This means that 92 % of the variability in the data is explained by the correlation.

Twenty degrees
The same procedure was repeated for the experimental data from an annular diffuser with a 20° half-opening angle to obtain further corroborating evidence; the results are shown in *Fig.* 6.1.

The circled data point does not exhibit any static-pressure recovery—on the contrary, the static-pressure recovery is slightly negative. Further inspection of the work of KUSCHEL (2014)* did not yield any satisfactory explanation for this behaviour as the analysis provided was not decisive about whether any tip-leakage vortices had been measured at this operating point. The non-negligible aerodynamic loading of the rotor, however, implies the presence

---

*see also KUSCHEL ET AL. (2015)

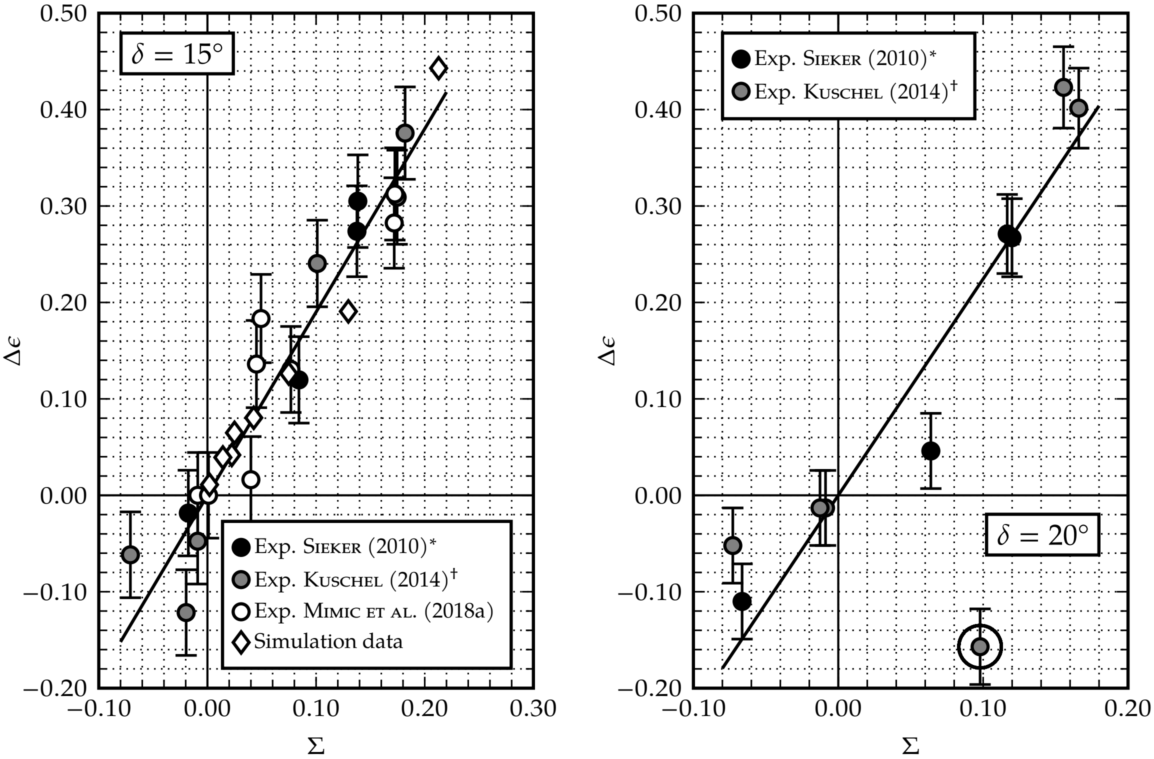

Figure 6.1.: Validation of the effectiveness correlations for 15° (left) and 20° (right)

of such vortex structures. In any case—be it undetected flow phenomena, such as flow separation on the blades, large-scale unsteadiness in the interaction between rotor outflow and diffuser separation or merely erroneous measurement—this point is discarded as an outlier with regard to the correlation formulated here.

Again, it follows that there is a linear correlation between Σ and $\Delta\epsilon$, i.e.,

$$\Delta\epsilon = 2.24\Sigma, \qquad R^2 = 0.91. \tag{6.2}$$

It can already be inferred from these two correlations that the sensitivity of the diffuser effectiveness to the vortex-induced stabilisation increases with the opening angle (see *Hyp.* 4.1). This will be discussed further in *Sec.* 6.1.5.

see *Hyp.* 4.6 **Conclusion 6.1.** The data confirm *Hyp.* 4.6: the effectiveness ϵ increases linearly with the stabilisation number Σ.

6.1.2. Total-pressure losses

Hypothesis 4.7 posits a linear relationship between the product of the extrapolated stabilisation number $\Xi\Sigma$ (see *Eqn.* 4.36) and the total-pressure loss coefficient ζ of the diffuser. The experimental data of the 15° diffuser from Mimic et al. (2018a) were analysed together

---

[*] see also Sieker and Seume (2008a)

[†] see also Kuschel et al. (2015)

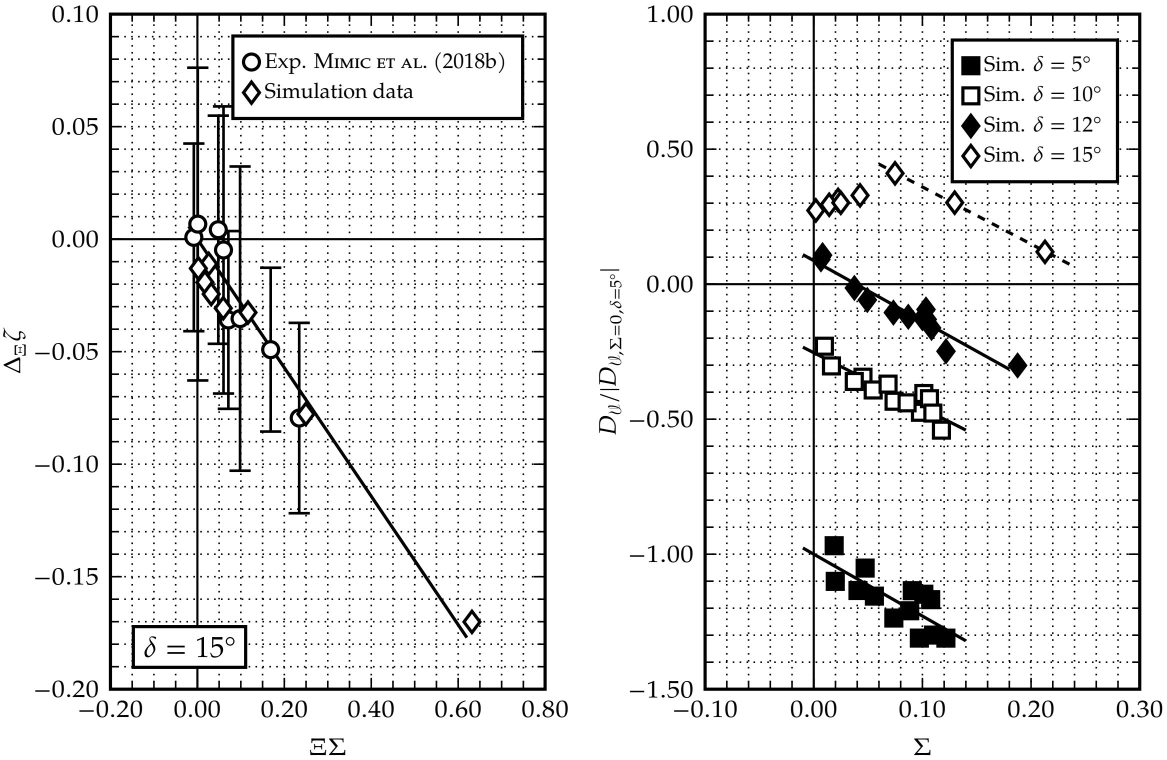

Figure 6.2.: Validation of the total-pressure loss correlations for 15° (left) and radial diffusion of circumferential vorticity (right)

with the corresponding numerical simulations with regard to these characteristic numbers. Because no information on the density encountered in the experiments was available, $\rho = 1\,\mathrm{kg/m^3}$ was assumed for both numerical and experimental samples. The resulting distribution is shown on the left-hand side of *Fig.* 6.2. The data can be approximated by means of linear regression and yield the following correlation:

$$\Delta_\Xi \zeta = -0.29\Xi\Sigma, \qquad R^2 = 0.93. \tag{6.3}$$

The following can be concluded:

Conclusion 6.2. The data confirm *Hyp.* 4.7: the total-pressure loss coefficient decreases linearly with an increasing extrapolated stabilisation number ΞΣ with regard to an extrapolated reference $\Xi\zeta_{\mathrm{ref}}$.

see *Hyp.* 4.7

The stabilisation of the boundary layer and the resulting increased deceleration of the free stream yield lower velocity gradients within the boundary layer (see Mimic et al. 2018a), thereby reducing the losses produced by momentum diffusion as supported by a loss-decomposition study conducted by Mimic et al. (2019).

6.1.3. Vortex decay

Is the vortex decay simply a function of the vortex circulation or is it also determined by the momentum deficit of the boundary layer? *Hypothesis* 4.5 contends that the former is the case.

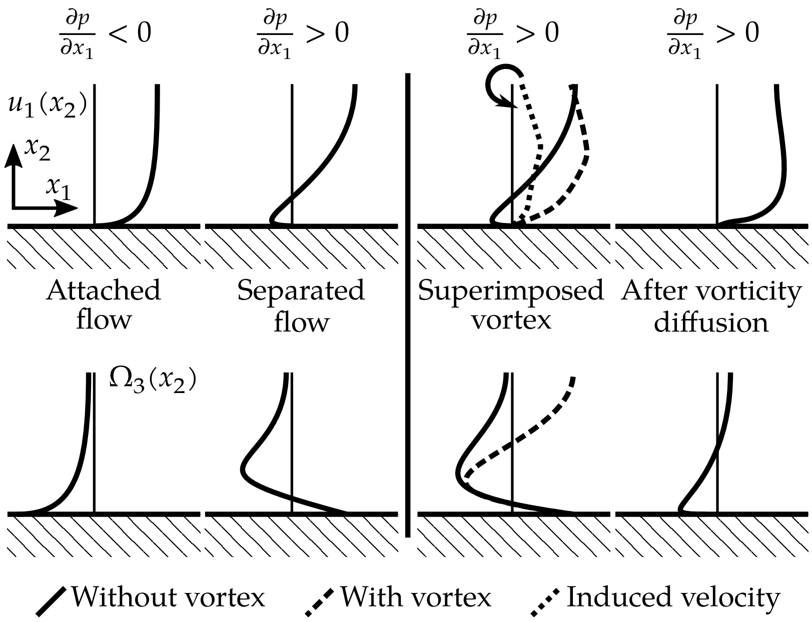

Figure 6.3.: Boundary-layer stabilisation by means of wall-normal vorticity diffusion (adapted from Mimic et al. 2018c)

To assess the substance of this hypothesis, numerical simulations of diffusers with half-opening angles of 5°, 10°, and 12° were analysed in addition to the 15° diffuser. While no experimental data were available for these cases, the simulation results from the 15° diffuser have been shown to be sufficiently accurate in comparison with their experimental counterparts. Since the shallower opening angles exhibit significantly "simpler" flow fields with limited or no flow separation, it can be argued that their numerical predictability at least matches, or even surpasses, that of the 15° diffuser.

Due to the relationship between circulation and vorticity, which is established per Stokes' theorem, the vorticity is used for the analysis in this section, as it can be calculated purely from local velocity gradients. As shown in *Fig.* 6.3, an attached boundary layer is characterised by a negative vorticity whereas the recirculation zone in a separated boundary layer exhibits positive vorticity.

Following the reasoning detailed by Mimic et al. (2018c), a steady, axisymmetric flow is assumed where only the circumferential vorticity component Ω_θ is considered. The vorticity equation (see *Eqn.* 3.85) may then be expressed in cylindrical coordinates which yields (see Panton 2013):

$$\rho u_{x_1}\frac{\partial \Omega_\theta}{\partial x_1} + \rho u_r \frac{\partial \Omega_\theta}{\partial r} = \rho \frac{\Omega_\theta u_r}{r} + \mu_{\text{eff}} \frac{\partial}{\partial r}\left[\frac{1}{r}\frac{\partial (r\Omega_\theta)}{\partial r}\right] + \mu_{\text{eff}} \frac{\partial^2 \Omega_\theta}{\partial x_1 \partial x_1}, \tag{6.4}$$

where the *effective viscosity* represents the sum of the molecular and turbulent viscosity, i.e.,

$$\mu_{\text{eff}} := \mu + \mu_{\text{turb}} \tag{6.5}$$

where the turbulent viscosity accounts for the effect of turbulence.

As explained by Mimic et al. (2018c), the stream-wise transport and radial advection of vorticity may be neglected in *Eqn.* (6.4), because the relevant transport mechanism is the wall-normal diffusion of vorticity (see also *Fig.* 6.3). The first term on the right-hand side of *Eqn.* (6.4), which results from the stretching of a circumferential vortex line at different radii, is between one and three orders of magnitude lower than the radial diffusion for the simulations presented in this work (results not shown) and is, thus, neglected in the following analysis.

To evaluate the overall vorticity diffusion flux, the volumetric average of the diffusion term is formulated:

$$D_{\mathcal{V}} = -\frac{1}{\mathcal{V}} \iiint_{\mathcal{V}} \mu_{\mathrm{eff}} \frac{\partial}{\partial r} \left[\frac{1}{r} \frac{\partial (r \Omega_\theta)}{\partial r} \right] \mathrm{d}V. \tag{6.6}$$

The negative sign is introduced to conserve the proper direction of the vorticity flux when expressed in a wall-normal coordinate system. The integration volume $\mathcal{V}$ ranges from the diffuser inlet plane to its outlet plane and from the Euler radius at the diffuser inlet to the casing to exclude the hub boundary layer.

The resulting volumetric average represents the average radial transport of circumferential vorticity, i.e., the vorticity transferred between vortex and boundary layer and, therefore, how much vorticity the vortex loses. The expectation derived from *Hyp.* 4.5 is that a given change in Σ will correlate with a constant change in $D_{\mathcal{V}}$ for any of the diffuser half-opening angles, which represent different degrees of momentum deficit in the boundary layer. However, because $D_{\mathcal{V}}$ contains information not only about the transport process between the vortices and boundary layer, but also about transport processes within the boundary layer, it is to be expected that the different half-opening angles will yield different values of $D_{\mathcal{V}}$.

The right-hand side of *Fig.* 6.2 confirms this notion for the most part: The diffusion increases with the opening angle, and, therefore, the momentum deficit of the boundary layer, being negative for the cases with predominantly attached boundary layers and positive in the case of massive flow separation, i.e. for $\delta = 15°$. Likewise, the 5°, 10°, and 12° diffusers exhibit virtually the same slope. This indicates that the same variation in the circulation of the stabilising vortices yields the same variation in the stabilising vorticity diffusion across different diffusers. The 15° diffuser, however, behaves differently in the case of low stabilisation numbers: the anomalous test cases are characterised by a weak aerodynamic loading of the rotor and massive flow separation just downstream of the diffuser inlet which likely violates the assumptions of the theory presented (see *Sec.* 4.4). Nevertheless, beyond a certain value of the stabilisation number, this diffuser assumes the same behaviour as observed for shallower half-opening angles, as indicated by the dashed line. This anomaly was not evident in the work of Mimic et al. (2018c), where the particular test cases seemed to merely exhibit scattering. The improved definition of the stabilisation number presented in this work, however, appears to be more sensitive towards changes in the rotor operating point, especially in the case of low aerodynamic loading of the rotor.

Conclusion 6.3. The numerical results partially support *Hyp.* 4.5: the vortex decay is mostly dependent upon the vortex circulation and not upon the momentum deficit of the boundary layer. This conclusion is, however, not applicable to the case of low stabilisation numbers together with strong flow separation just downstream of the diffuser inlet. see *Hyp.* 4.5

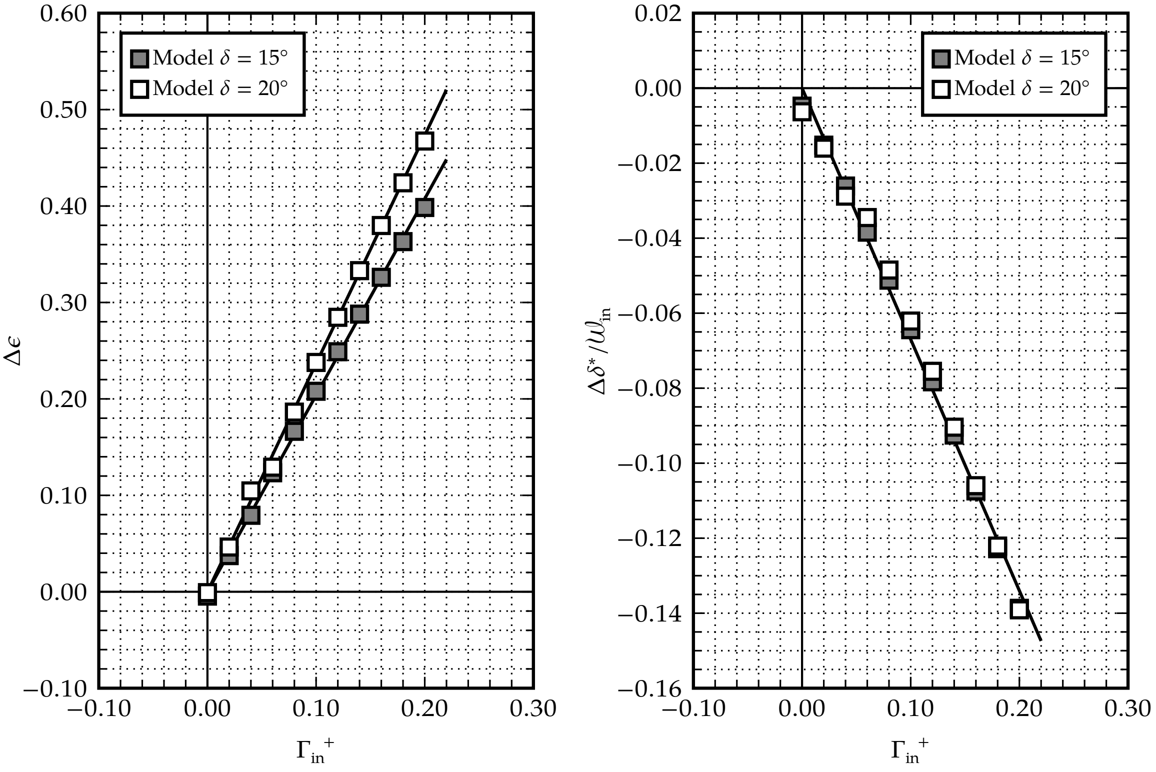

Figure 6.4.: Model predictions: changes in effectiveness (left) and displacement thickness (right) versus non-dimensional circulation

6.1.4. Boundary-layer stabilisation

Conclusion 6.3 leads to the question whether the sensitivity of the boundary layer towards vortex-induced stabilisation is influenced by the momentum deficit of the boundary layer, i.e., whether a more pronounced momentum deficit of the boundary layer implies an increased sensitivity.

To give a tentative answer to this question, the boundary-layer prediction model of Bardina et al. (1982) was implemented as described in *Sec.* 3.3.5. Its functionality was verified successfully by reproducing the computation results listed by the authors (results not shown). Deviations from the data published were negligible and can be attributed to differences in the numerical scheme employed for solving the model equations (see *App.* A). Because the original implementations of Bardina et al. (1982) were tailored to planar and equiangular annular diffusers, the transverse-curvature term in *Eqns* (3.71) and (3.72) was adapted in this work for the calculation of the behaviour of annular diffusers with diverging external walls and constant hub diameter. Finally, the vortex model detailed in *Sec.* 4.4 was implemented as described in *Lst.* A.1 in *App.* A.

The use of such a lower-order model has several advantages over the higher-order simulations presented so far. *Firstly,* boundary layers, their thickness parameters as well as the involved momentum exchange and entrainment are *concepts*; they describe features and events, which are extracted from measurements or flow simulations. The inherently arbitrary character of the quantities by which these features and events are described, however, can pose some difficulties. This becomes especially apparent when boundary-layer parameters and transport processes are to be evaluated in highly perturbed flow regions. An accurate calculation of these quantities in the interaction zone between boundary layer and vortex can, therefore, lead to inconclusive results. A prediction method with a higher degree of abstraction can circumvent some of these difficulties. *Secondly,* a lower-order model where individual objects, processes, or features are modelled individually and interact via predefined interfaces allows the deliberate and independent variation of various parameters in a way that is hardly feasible in higher-order simulations or experiments. *Exempli gratia,* the shear stress and entrainment imposed by the vortex can be varied separately and their individual contributions to the stabilisation process assessed.

Model calibration

Before activating the vortex model, the boundary-layer parameters at the diffuser inlet were selected so as to reproduce the diffuser effectiveness obtained from a linear regression of the experimental data from Kuschel (2014)[*] at $\Sigma = 0$. This was done for the 15° and 20° diffusers. The vortex model was then activated and the model constants for the vortex decay, vortex-induced shear-stress, and entrainment terms in *Eqns* (4.15) and (4.17) were varied until similar behaviour to the correlations given in *Sec.* 6.1.1 was achieved. The result is shown in *Fig.* 6.4. As can be seen, both relationships could be reproduced to an accuracy well within the measurement uncertainties.

The corresponding decreases in the displacement thickness calculated at the diffuser outlet for various Σ are shown in *Fig.* 6.4: both the 15° and 20° diffusers exhibit the same decrease in displacement thickness, which supports *Hyp.* 4.2.

Conclusion 6.4. The modelling results agree with *Hyp.* 4.2: the sensitivity of the boundary layer towards vortex-induced stabilisation does not depend upon the momentum deficit of the boundary layer, but on the circulation of the vortex. see *Hyp.* 4.2

Momentum and mass exchange

The calibration of the model yielded positive values for the model constants which control the shear-stress and entrainment terms. With the formulations used here, this equates not only to a shear stress acting upon the boundary layer in the free-stream direction, but also to an increased mass transfer *into* the boundary layer. In order to separate the contributions of the momentum transfer via shear stresses and the mass transfer via entrainment, the constants c_Ω and c_E were varied one at a time in a small separate study for the 15° diffuser. The variations are expressed as fractions of the respective values of c_Ω and c_E obtained from the model calibration. As can be seen from *Fig.* 6.5, the displacement thickness δ^* and shape factor H exhibit a distinctly higher sensitivity towards the entrainment term than they do towards the shear-stress term. Nevertheless, the displacement thickness decreases in both cases.

Conclusion 6.5. The modelling results show a linear dependency of the boundary-layer parameters displacement thickness and shape factor upon the vortex shear stresses. The results are, thus, consistent with the theory presented. see *Hyp.* 4.3

---

[*] see also Kuschel et al. (2015)

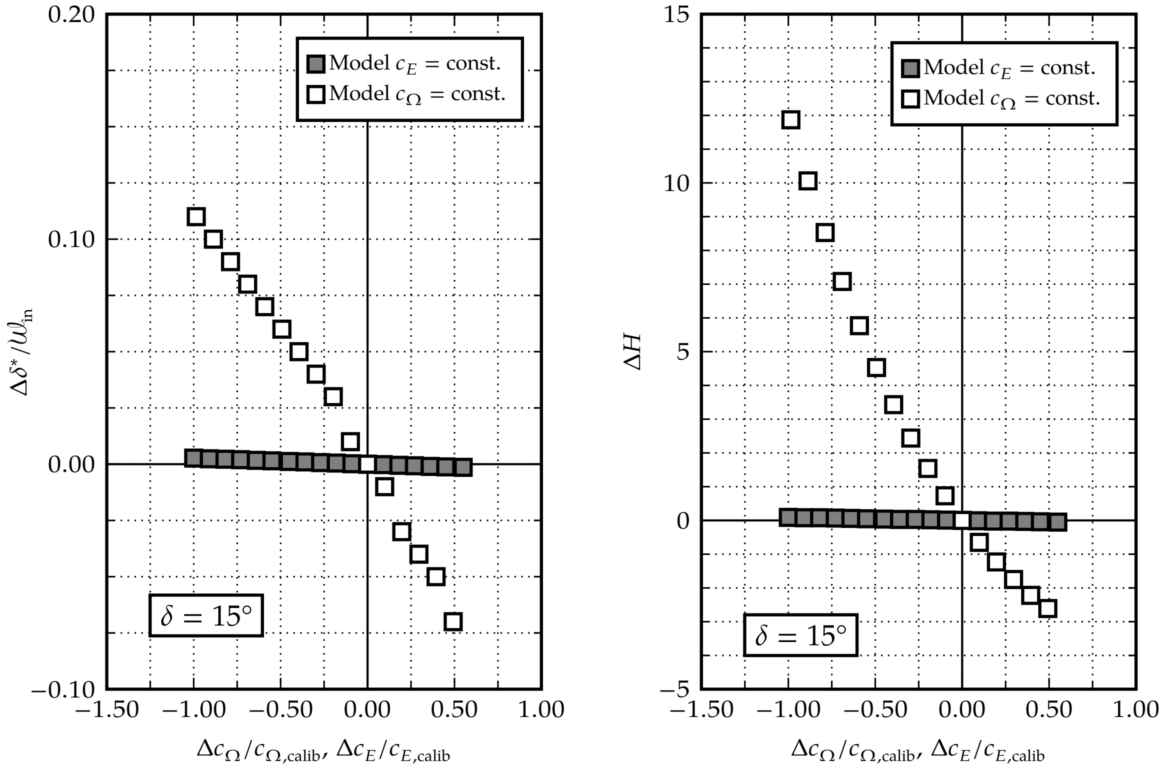

Figure 6.5.: Sensitivity analysis: changes in displacement thickness (left) and shape factor (right) versus calibration constants c_Ω and c_E for the 15° diffuser

see *Hyp.* 4.4 **Conclusion 6.6.** The modelling results show a strictly monotone dependency of the boundary-layer parameters displacement thickness and shape factor upon the vortex entrainment. The results are, thus, consistent with the theory presented.

The latter conclusion is consistent with the observations of CUTLER AND BRADSHAW (1993b): the displacement thickness increases after fluid is entrained into the vortex and *out of* the boundary layer. In the present case, the displacement decreases for a net entrainment of fluid *into* the boundary layer.

It must be kept in mind, however, that these data were merely calibrated postdictively using integral diffuser-performance parameters. Even though they agree with the theory presented, further calibration based upon boundary-layer measurements and extensive testing with experimental data are required in order to substantiate these results.

6.1.5. Diffuser opening angle

Hypothesis 4.1 predicts an increasing sensitivity of the diffuser towards the stabilising tip-leakage vortices—i.e., an increase in the slope expressed by the general relationship in *Eqn.* (4.31)—for increasing diffuser half-opening angles. To gain an insight into this matter, the effectiveness was evaluated from numerical simulations of the diffusers with half-opening angles of 5°, 10°, 12°, and 15°.

The results are shown in *Fig.* 6.6: in addition to the results presented for the 15° and 20° diffusers in *Fig.* 6.1, they confirm the conjecture that the slope of the correlation increases

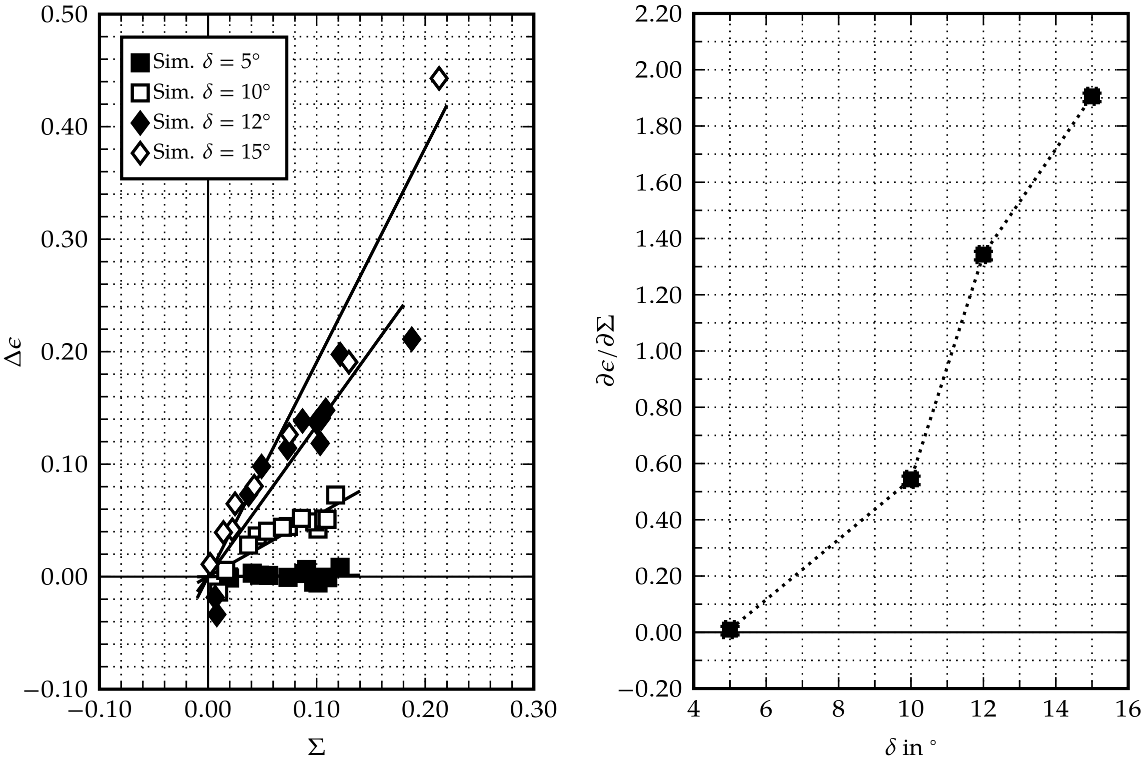

Figure 6.6.: Changes in effectiveness versus stabilisation number for different half-opening angles (left); sensitivities (right)

with the half-opening angle. The resulting correlations are given below.

$$5°: \quad \Delta\epsilon = 0.01\Sigma, \quad R^2 = 0.01, \tag{6.7}$$

$$10°: \quad \Delta\epsilon = 0.54\Sigma, \quad R^2 = 0.80, \tag{6.8}$$

$$12°: \quad \Delta\epsilon = 1.34\Sigma, \quad R^2 = 0.86, \tag{6.9}$$

$$15°: \quad \Delta\epsilon = 1.91\Sigma, \quad R^2 = 0.96. \tag{6.10}$$

The changes in the sensitivity are visualised in *Fig.* 6.6. The dotted line indicates that the increase in sensitivity of the diffuser effectiveness towards the stabilisation number is close to linear for half-opening angles upwards of 10°. This was the lowest half-opening angle for which flow separation could be observed in the simulations. This subdivision into attached and separated flow regimes roughly matches the values given by TRAUPEL (2001). Notably, the lowest half-opening angle, 5°, exhibits virtually no sensitivity. This is, however, not surprising because the diffuser operates without any flow separation.

Conclusion 6.7. The simulation results support *Hyp.* 4.1: the sensitivity of the effectiveness towards vortex-induced stabilisation increases with the diffuser opening angle.

see *Hyp.* 4.1

If a change in sensitivity is observed for the effectiveness, a change in sensitivity is to be expected for the total-pressure losses, too. In this study, the actual values of the density were used to calculate Ξ. *Figure* 6.7 shows the behaviour of the total-pressure loss correlation for varying half-opening angles. Consistent with the increasing sensitivity of the effectiveness,

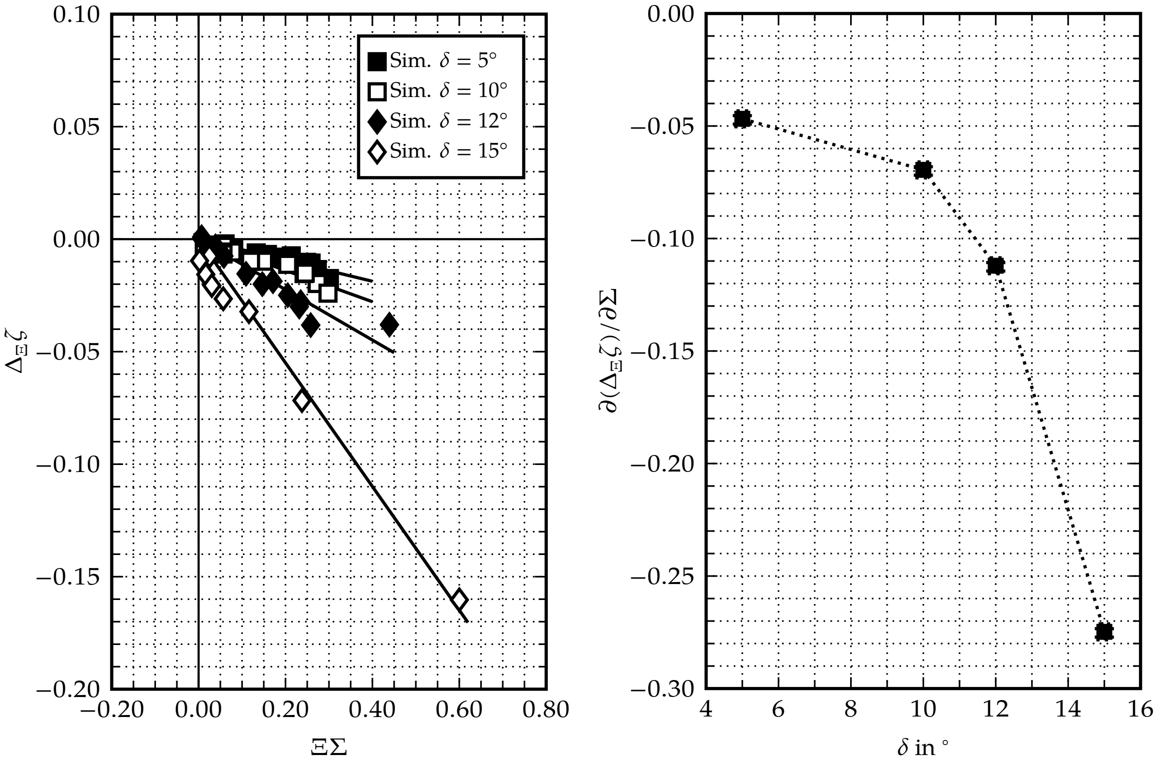

Figure 6.7.: Extrapolated changes in the total-pressure losses versus extrapolated stabilisation number for different half-opening angles (left); sensitivities (right)

the sensitivities of the total-pressure loss coefficient increase, too. Or, in other words: the same value of Σ yields a more significant loss reduction for steeper half-opening angles. This is especially apparent in the case of the 15° diffuser: the reduction of the massive flow separation yields a considerable decline in the total-pressure losses. The corresponding correlations are given below.

$$5^\circ: \quad \Delta_\Xi\zeta = -0.05\Xi\Sigma, \quad R^2 = 0.85, \tag{6.11}$$

$$10^\circ: \quad \Delta_\Xi\zeta = -0.07\Xi\Sigma, \quad R^2 = 0.92, \tag{6.12}$$

$$12^\circ: \quad \Delta_\Xi\zeta = -0.11\Xi\Sigma, \quad R^2 = 0.87, \tag{6.13}$$

$$15^\circ: \quad \Delta_\Xi\zeta = -0.27\Xi\Sigma, \quad R^2 = 0.97. \tag{6.14}$$

Conclusion 6.8. The simulation results show that the sensitivity of the extrapolated changes in the total-pressure loss coefficient towards the vortex-induced stabilisation increases with the diffuser opening angle.

6.1.6. Diffuser length

An additional study was conducted to determine the impact of the diffuser length. The outlet evaluation plane was varied in order to obtain non-dimensional diffuser lengths of approximately $x/\mathcal{W}_{\mathrm{in}} = 0.5, 1.0, 1.5,$ and 2.0. The effectiveness was calculated for all cases. *Figure* 6.8 shows that, for the massively separated 15° diffuser, lower sensitivities can be observed for greater non-dimensional diffuser lengths. This can be attributed to the fact that

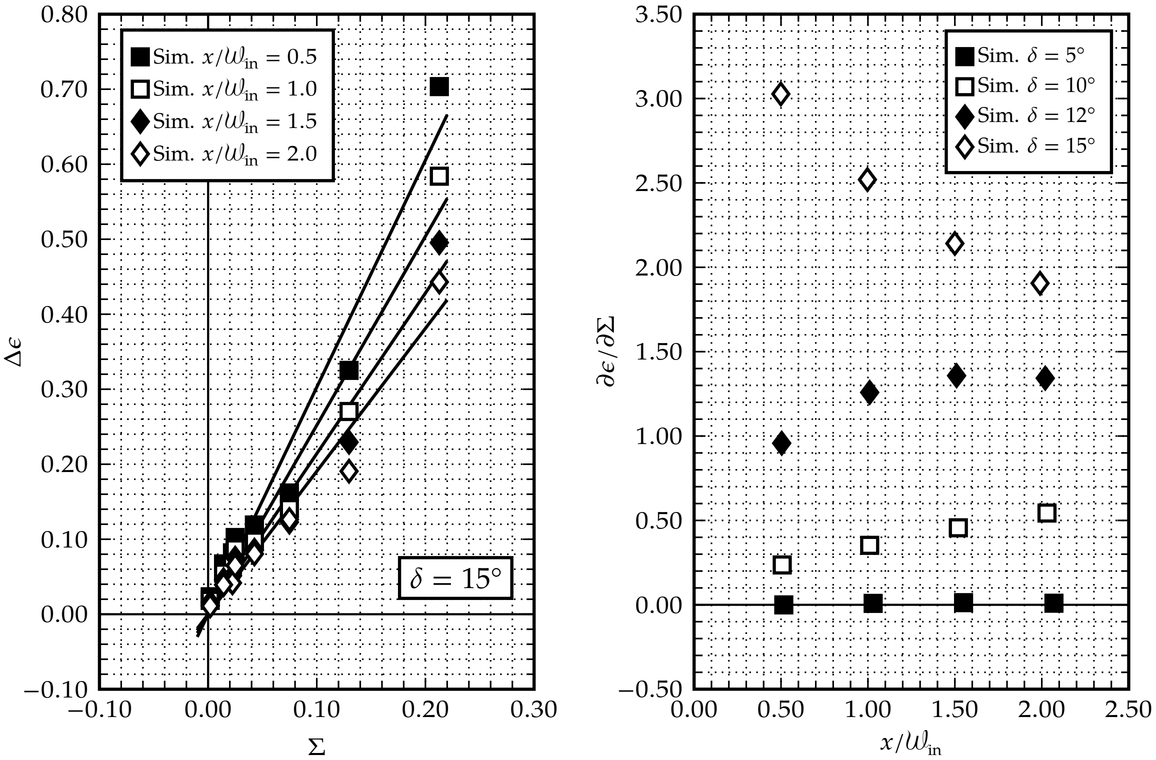

Figure 6.8.: Changes in effectiveness versus stabilisation number for different diffuser lengths (left); sensitivities (right)

flow separation occurs very early in this diffuser. The greatest benefit is, therefore, obtained just downstream of the location of separation onset.

Figure 6.8 shows the sensitivity distributions of other diffuser opening angles for comparison. Interestingly, the sensitivity decreases only at the steepest opening angle where massive flow separation occcurs. The 10° diffuser, which remains mostly attached (Mimic et al. 2018c), exhibits an increasing sensitivity with increasing diffuser length. It is likely that the benefit of vortex-induced boundary-layer stabilisation acts evenly upon the entire length of the boundary layer.

The 10° diffuser presents an interesting borderline case. Its casing boundary layer separates roughly between $x/\mathcal{W}_{\text{in}} = 1.0$ and $x/\mathcal{W}_{\text{in}} = 1.5$, as shown by Mimic et al. (2018c). This is also where a flattening of the sensitivity can be seen in *Fig.* 6.8. It may be speculated that a longer diffuser would experience a decline in sensitivity.

Conclusion 6.9. The simulation results show that the sensitivity of the diffuser effectiveness towards the vortex-induced stabilisation decreases gradually downstream of the separation location in the case of massive flow separation. It increases, however, in the case of attached boundary layers.

An equivalent study was conducted to determine the impact of the diffuser length on the reduction in total-pressure losses. As shown in *Fig.* 6.9, all cases exhibit an increase in sensitivity as the outlet plane is moved downstream. This is likely a result of a cumulative total-pressure loss reduction, even downstream of the separation.

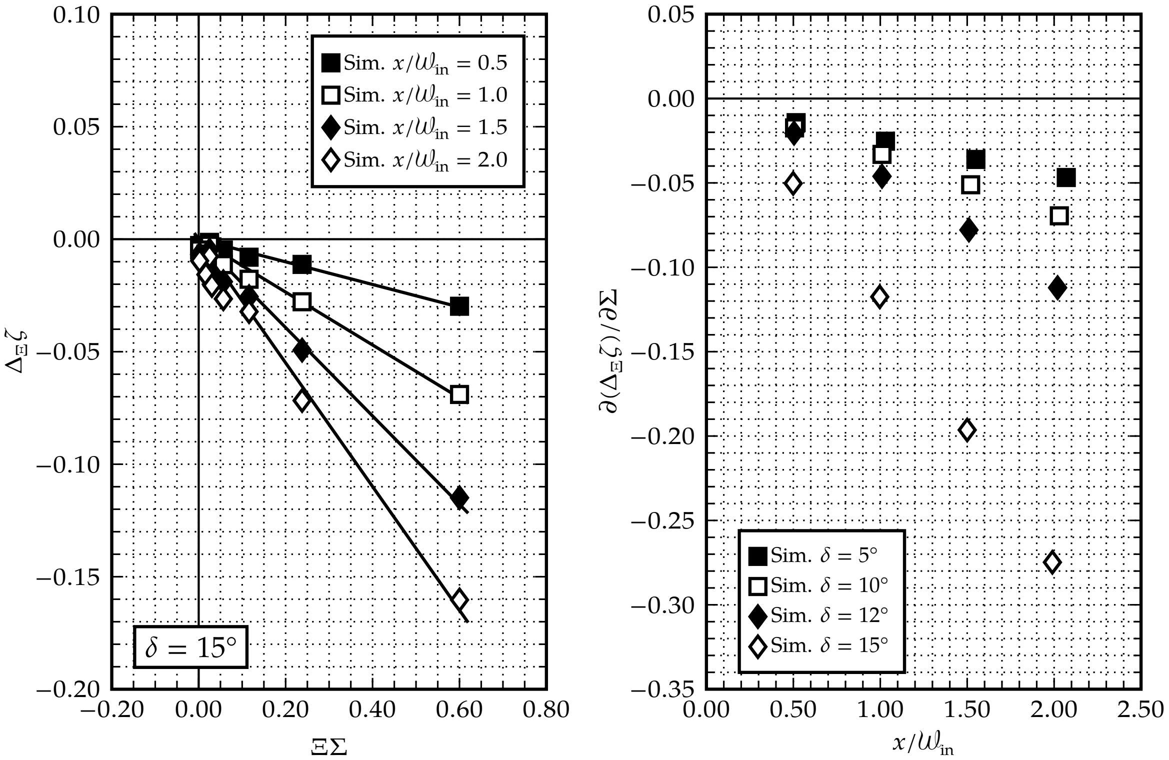

Figure 6.9.: Extrapolated changes in the total-pressure losses versus extrapolated stabilisation number for different diffuser lengths (left); sensitivities (right)

Conclusion 6.10. The simulation results show that the sensitivity of the extrapolated changes in the total-pressure loss coefficient towards the vortex-induced stabilisation increases linearly with the diffuser length.

6.2. Summary of the results

see *Hyp.* 4.7, *Hyp.* 4.6

The hypotheses and respective conclusions summarised in this section are listed verbatim in *Tab.* E.1 in *App.* E. The data presented confirm, or at least support, all predictions derived from the theory proposed. Distinct linear correlations between the improved stabilisation number Σ and the changes in diffuser effectiveness $\Delta\epsilon$, as well as between the extrapolated stabilisation number $\Xi\Sigma$ and the changes in the total-pressure loss coefficient $\Delta_\Xi\zeta$, could be substantiated using both extensive numerical and experimental data.

see *Hyp.* 4.5, *Hyp.* 4.4, *Hyp.* 4.3, *Hyp.* 4.2

It was shown that both the numerical simulations and the diffuser-prediction model proposed provide corroborating evidence for the dominance of the vortex intensity in determining the boundary-layer stabilisation process and the vortex decay in the face of changes in the momentum deficit of the boundary layer. The model suggests that the boundary-layer stabilisation can be explained by a transfer of momentum and mass between the vortex and boundary layer via shear stresses and fluid entrainment; the entrainment appears to be the dominant contributor. Thorough experimental studies are, however, required to further substantiate these provisional conclusions.

Moreover, the numerical data confirm the hypothesised positive influence of the diffuser opening angle on the sensitivity of the vortex-induced effectiveness increase. Additional studies revealed that these sensitivities decrease with increasing diffuser length in the case of massive flow separation; they do, however, increase with the diffuser length in the case of attached boundary layers. The sensitivity of the changes in the total-pressure loss coefficient $\Delta_{\Xi}\zeta$ was shown to increase with the opening angle and diffuser length. ■ see *Hyp.* 4.1

Chapter 7.

Applicability

The results presented in the previous chapter can be further condensed into design charts to facilitate their application in a turbomachinery design process. Due to the multidimensionality of the problem at hand, it is most accessible to aggregate the sensitivities of the diffuser effectiveness (see the right-hand side of *Figs* 6.6 and 6.8) and the extrapolated total-pressure loss coefficient (see the right-hand side of *Figs* 6.7 and 6.9). The resulting sensitivity maps are shown in *Figs* 7.1 and 7.2. Following the majority of well-established diffuser design charts, the area ratio and non-dimensional diffuser length were chosen as the independent variables in this representation. The contour lines indicate interpolated lines of constant sensitivity. These sensitivity maps, or design charts, can be used in several stages of a turbomachinery design process to determine the static-pressure recovery coefficient and total-pressure loss coefficient of an annular diffuser downstream of a turbine at various operating points.

7.1. Static-pressure recovery

The general procedure for the calculation of the static-pressure recovery coefficient is equivalent to the one described in Mimic et al. (2018a) and can be summarised in seven steps.

1. Determine the reference stabilisation number Σ_{ref} and the stabilisation number Σ at the operating point of interest using *Eqn.* (4.30):

   $$\Sigma = \frac{\Psi F}{\Phi^2 \cos \alpha}.$$

   In most cases, the reference will likely be the aerodynamically non-stabilised diffuser, i.e., $\Sigma_{\mathrm{ref}} = 0$. It is, however, also possible to use other available diffuser operating points.

2. Estimate a reference static-pressure recovery coefficient $c_{p,\mathrm{ref}}$ for the reference stabilisation number Σ_{ref}. Possible ways to obtain an accurate estimate will be expounded following the description of this procedure.

3. Calculate the swirl-based ideal static-pressure recovery coefficient using *Eqn.* (1.21):

   $$c_{p,\mathrm{id}} := 1 - \frac{1/\mathfrak{A}^2 + \tan^2(\alpha)\left(\frac{r_{\mathrm{Euler,in}}}{r_{\mathrm{Euler,out}}}\right)^2}{1 + \tan^2(\alpha)}.$$

4. Use the results from the two previous steps to calculate the reference effectiveness ϵ_{ref} for the non-stabilised diffuser using *Eqn.* (1.35):

   $$\epsilon_{\text{ref}} = \frac{c_{p,\text{ref}}}{c_{p,\text{id}}}.$$

5. Obtain the sensitivity of the diffuser effectiveness $\partial\epsilon/\partial\Sigma$ from *Fig.* 7.1.

6. Calculate the diffuser effectiveness at the operating point of interest using

   $$\epsilon = \epsilon_{\text{ref}} + \frac{\partial\epsilon}{\partial\Sigma}\left(\Sigma - \Sigma_{\text{ref}}\right),$$

   which is adapted from the general formulation given in *Eqn.* (4.31).

7. Finally, calculate the static-pressure recovery coefficient by rearranging *Eqn.* (1.35):

   $$c_p = c_{p,\text{id}}\epsilon.$$

The point in the design process at which the above procedure is employed dictates how the reference static-pressure recovery is determined. Two possible scenarios are given for reference.

Early design stages: In the earliest design stages, the reference static-pressure recovery coefficient can be obtained from empirical diffuser design charts, e.g., by Sovran and Klomp (1967) or ESDU (1977). Because the rotor blades introduce additional blockage to the diffuser inflow, this approach will likely lead to a slight over-estimation of the resulting static-pressure recovery. If additional empirical data exist for the relationship between the rotor-induced blockage and decrease in static-pressure recovery, then these can be used for a more accurate estimate.

Later design stages: As soon as designs exist for the rotor and diffuser, a high-fidelity simulation of the system can be performed for the reference operating point; the correlations can then be used to estimate the static-pressure recovery across the operating range of the system.

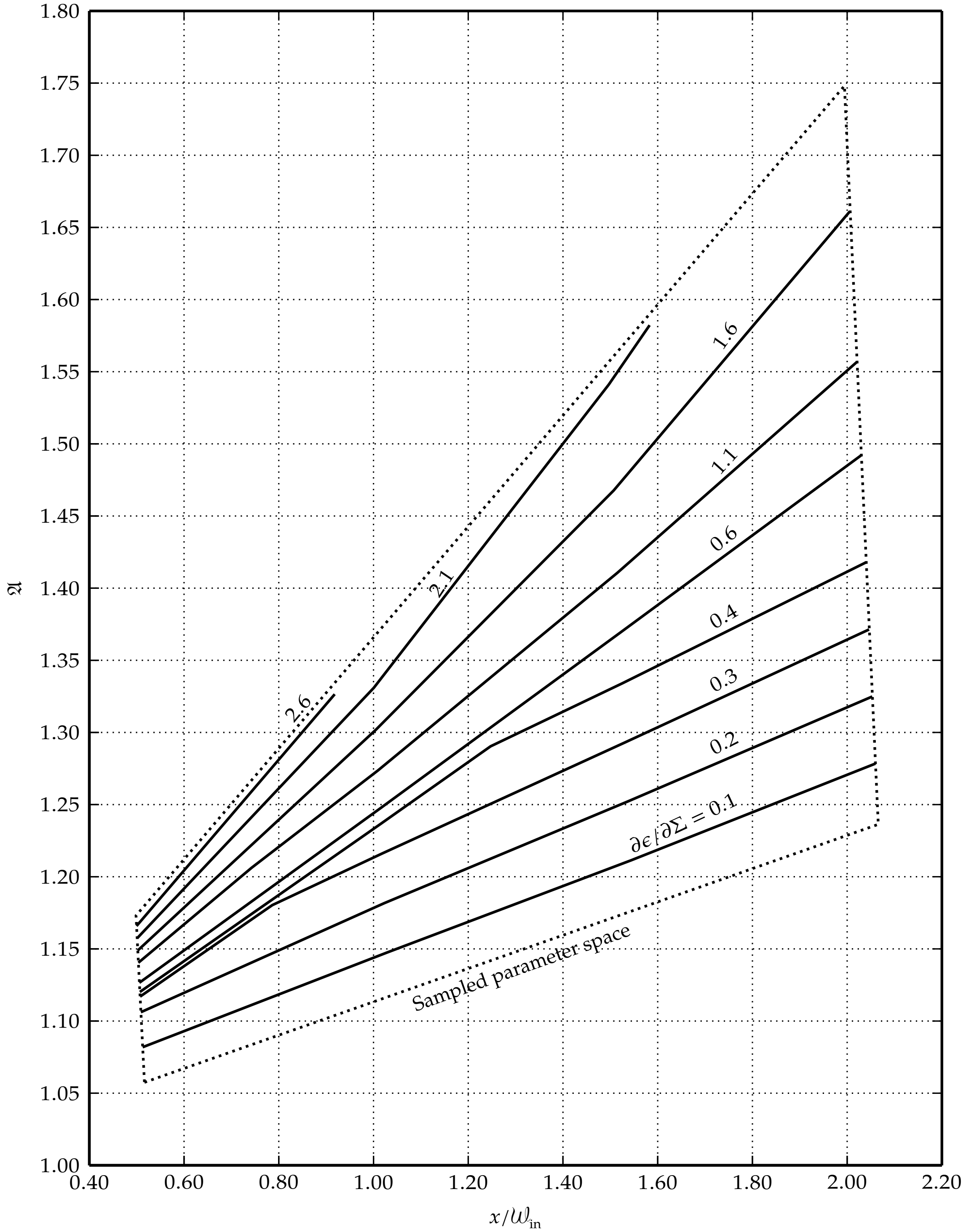

Figure 7.1.: Diffuser design chart showing the sensitivity distribution of the diffuser effectiveness towards the stabilisation number as a function of the non-dimensional diffuser length and the diffuser area ratio

7.2. Total-pressure losses

The total-pressure loss coefficient can be calculated for various operating points of interest in a similar manner to the static-pressure recovery coefficient. If the corresponding stabilisation numbers Σ_{ref} and Σ have already been calculated, this requires three additional steps which are summarised below.

1. Determine the extrapolation factor between the reference and the operating point of interest using *Eqn.* (4.36):

$$\Xi := \frac{\frac{\rho}{2}u_{\text{in}}^2}{\frac{\rho_{\text{ref}}}{2}u_{\text{in,ref}}^2}\frac{\ell_{\text{ch}}/\ell_{\text{p}}}{\ell_{\text{ch,ref}}/\ell_{\text{p,ref}}}\frac{\cos\alpha_{\text{ref}}}{\cos\alpha}\left[1+\frac{\left|\Phi-\Phi_{\text{design}}\right|}{\Phi_{\text{ref}}}\right].$$

2. Obtain the sensitivity of the extrapolated total-pressure loss coefficient $\partial(\Delta_\Xi\zeta)/\partial(\Xi\Sigma)$ from *Fig.* 7.2.

3. Calculate the total-pressure loss coefficient at the operating point of interest by rearranging *Eqn.* (4.37):

$$\zeta = \Xi\zeta_{\text{ref}} + \frac{\partial(\Delta_\Xi\zeta)}{\partial(\Xi\Sigma)}\Xi\Sigma.$$

Again, in the early design stages, these values can be estimated from empirical data, eg., by ESDU (1977) or using a diffuser simulation procedure similar to the method devised by Bardina et al. (1982). Later in the design process, simulation results can be used.

7.3. Parameter space

The dotted lines in *Figs* 7.1 and 7.2 indicate the envelope of the parameter space sampled. In any case, the sensitivities of the effectivess are supported by numerical data for values of Σ between 0 and 0.12—and up to 0.21 for the steepest half-opening angle (see the left-hand side of *Fig.* 6.6). Likewise, the sensitivities of the total-pressure losses are supported by numerical data in any case for values of $\Xi\Sigma$ between 0 and 0.3—and up to 0.6 for the steepest half-opening angle (see the left-hand side of *Fig.* 6.7). Extrapolations beyond the limits of the parameter space should be avoided, especially towards higher aerodynamic loading, i.e., higher area ratios.

As mentioned in the introduction of this chapter, the contour lines were obtained from interpolations between the sampling points. This step was necessary due to the high degree of data consolidation and the resulting sparseness of the sixteen available sampling points. Beyond a mere increase in sampling density, it is advisable to conduct variations of the ratio between the hub and casing radii in future investigations to further corroborate the validity of the design charts.

Likewise, it is advisable to expand the parameter space, both by expanding the limits of the envelope shown in *Figs* 7.1 and 7.2 and by exploring new independent variables. Such investigations should comprise variations of the blade geometry, aspect ratio, and tip gap to induce variations in the chord-wise and span-wise loading distributions. Furthermore, they should include different flow conditions, e.g., by variation of the inflow turbulence as well as the Reynolds and Mach number.

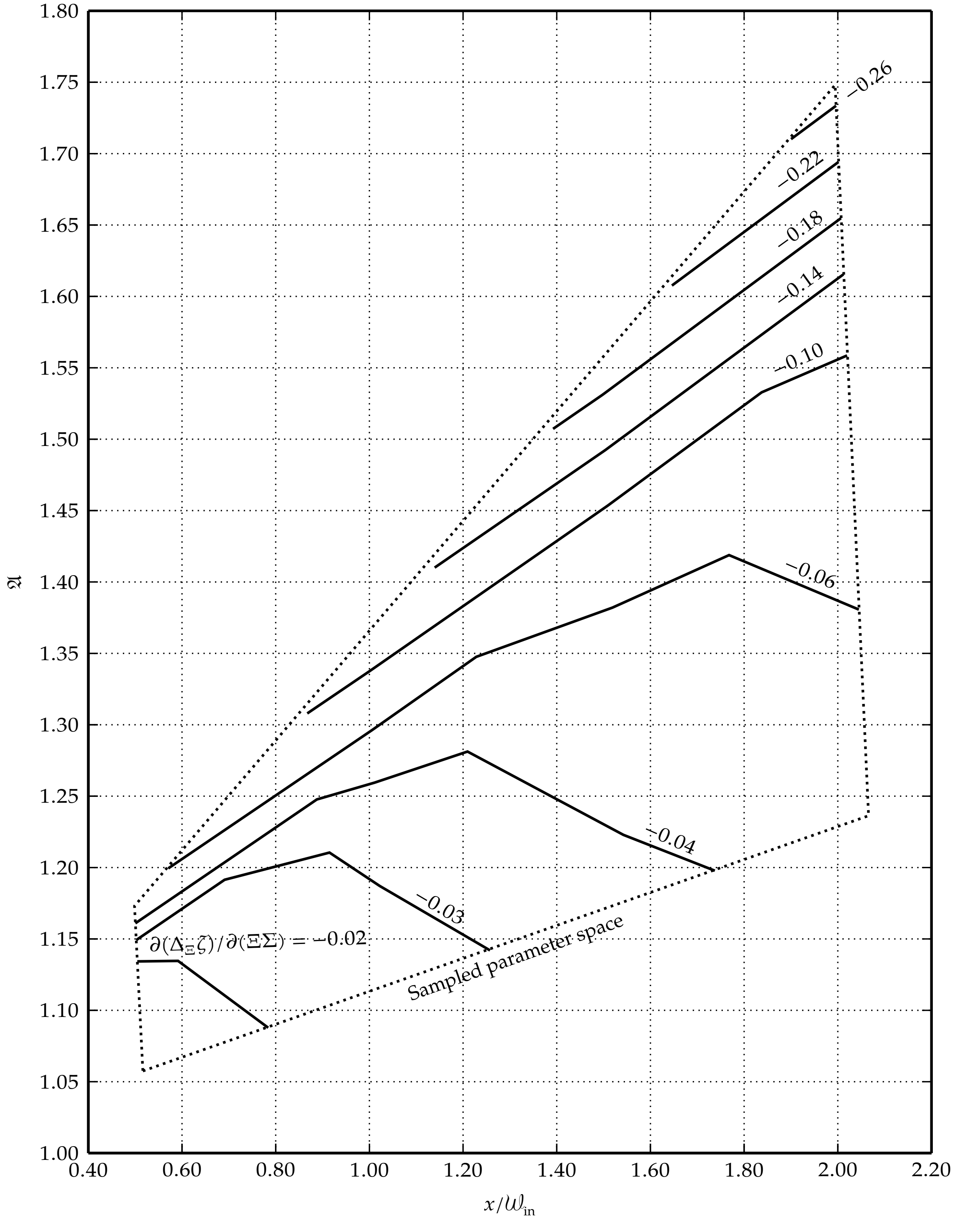

Figure 7.2.: Diffuser design chart showing the sensitivity distribution of the extrapolated total-pressure loss coefficient towards the extrapolated stabilisation number as a function of the non-dimensional diffuser length and the diffuser area ratio

Chapter 8.

Conclusions

This work presents a novel theory of turbine–diffuser interaction. More specifically, this theory addresses the stabilisation of diffuser boundary layers induced by tip-leakage vortices from an upstream rotor.

The theory provides a framework to characterise tip-leakage vortices based upon integral stage-design parameters. The stage parameters loading coefficient Ψ, flow coefficient Φ, swirl angle α, and non-dimensional blade-passing frequency F have been identified as the determinants for the intensity, orientation, and duty cycle of the tip-leakage vortices. These parameters have been condensed into the stabilisation number Σ as a predictor for the inflow-dependent diffuser performance.

Compared to the publications preceding this thesis, the significance of all four determinants and their nexus to the stage-design parameters has been derived with greater rigour. This has led to an improved formulation of the stabilisation number.

Effectiveness

It has been demonstrated, on the basis of experimental data and partially scale-resolving simulations, that the stabilisation number is a valid predictor for the turbine-induced increase in diffuser effectiveness. The changes in diffuser effectiveness correlate linearly with the stabilisation number across a wide range of rotor operating points and diffuser opening angles. The sensitivity of the effectiveness towards the vortex-induced stabilisation increases with the diffuser opening angle. The data suggest that this is likely not primarily due to a varying momentum deficit of the boundary layer. The stabilising vorticity transport between vortices and boundary layer rather seems to be predominantly determined by the circulation of the vortices, unless the stabilising vortices are weak and massive flow separation occurs just downstream of the initial point of interaction, at which point the underlying assumptions of the theory seem to break down. This anomalous behaviour is, however, restricted to operating points with virtually no aerodynamic loading of the rotor.

Overall, the dominant cause for the increase in sensitivity is rather to be found in the diffuser geometry itself: a given shift in the location of separation onset causes a greater change in diffuser blockage if the opening angle is steeper. The relationship between the sensitivity and diffuser length has been shown to depend upon the boundary-layer state: it decreases with increasing diffuser length in the case of massive flow separation and increases for predominantly attached boundary layers. As shown in the chapter *Applicability*, the results of the studies regarding the diffuser effectiveness have been mapped to the non-dimensional diffuser length and area ratio to provide a novel diffuser design chart.

Total-pressure losses
An additional parameter, the extrapolation factor Ξ, has been devised in order to predict the influence of the turbine outflow on the total-pressure losses generated in the diffuser. This factor expresses the influence of the flow coefficient, rotor solidity, dynamic pressure and diffuser inlet swirl on the wake deficit, wake duty cycle, wake mixing losses, and the increase in stream-path length, respectively. Multiplied by the stabilisation number and the reference total-pressure loss coefficient at $\Sigma = 0$, the extrapolation factor allows a prediction of the total-pressure losses.

Here, too, a distinctly linear correlation could be identified between the extrapolated stabilisation number, i.e., $\Xi\Sigma$ and the total pressure losses: the losses decrease with increasing $\Xi\Sigma$. The sensitivity, that is, the proportionality factor of the correlation, increases for steeper diffuser opening angles. This becomes especially apparent for the diffuser with the highest aerodynamic loading and, hence, the strongest flow separation. The cumulative effect of the vortex-induced boundary-layer stabilisation leads to an increasing sensitivity towards the extrapolated stabilisation number with increasing diffuser length. Again, as shown in the chapter *Applicability*, the results of the studies regarding the total-pressure loss coefficient have been mapped to the non-dimensional diffuser length and area ratio to provide another novel diffuser design chart.

Boundary-layer calculation
In order to obtain more insight into the boundary-layer mechanics, but also with prospective developments in mind, a one-dimensional prediction method for the behaviour of boundary layers in diffusers from the literature was implemented. The method solves a system of two ordinary differential equations describing conservation of momentum and mass in the boundary layer. The method was adapted to predict the behaviour of annular diffusers with a constant hub diameter and diverging casing.

The method was upgraded to feature the calculation of vortex-induced boundary-layer stabilisation in a way consistent with the derivations of the stabilisation number. This was achieved by the use of the Lamb–Oseen vortex: an analytical solution of the Navier–Stokes equations, which describes the decay of an initially irrotational vortex in a viscous fluid. The shear stresses imposed by the vortex onto the boundary-layer edge were used to model the transfer of momentum and the impact on fluid entrainment into the boundary layer. The model was successfully calibrated to postdict the changes in diffuser effectiveness for two opening angles. The result suggest that, even more than the momentum transfer between vortex and boundary layer, the entrainment of fluid into the boundary layer could play a significant role in the understanding of the exact stabilisation mechanism.

8.1. Limitations

Any attempt to explain nature is inherently subject to limitations. It is, therefore, highly desirable to be aware of the specific limitations of a particular model or theory. Several of the limitations of the theory proposed have already been stated as explicit assumptions: *exempli gratia,* incompressible flow, a vortex trajectory close to the boundary-layer edge and a negligible change in the hub boundary layer.

Other limitations arise from parameters which were deliberately kept constant, e.g., the aspect ratio of the blade, shape of the aerofoil, and tip gap. This means that the validity of the correlation parameters derived is yet to be demonstrated for a wider range of stage-design parameters, Reynolds and Mach numbers, and a greater variety of blade profiles and additional phenomena, such as flow separation on the blades.

Likewise, it is yet to be investigated how different types of diffuser geometries, such as conical diffusers or annular diffusers with a varying hub diameter, impact the interaction. The influence of different diffuser types is tied closely to a deeper understanding of the exact flow mechanisms driving processes such as the momentum transfer or vortex decay.

The turbine–diffuser prediction method was developed to take the first step in the direction of a deeper understanding. So far, however, the method could only be postdictively calibrated using rather limited and non-specific data, i.e., the diffuser effectiveness. This only implies that the prediction of one integral performance parameter of the cases investigated is located in the solution space predictable by the method. Nevertheless, the mere feasibility is a promising step and a potential guidepost for prospective research topics.

8.2. Prospects

The limitations mentioned above suggest three classes into which prospective research topics can be subdivided: research which fortifies the existing foundation of the theory proposed, research which aims to expand the boundaries of the theory and possible applications of the research.

The first class comprises further and more fine-grained experimental investigations *within* the existing parameter space. This means the measurement of a greater variety of diffuser opening angles across a wider range of operating points. To some extent, the variation of profile geometry and tip gap can be counted towards this category, as well. Their influence will most likely be attributable to changes in the radial aerodynamic-loading distribution and can be explained by modifying the present approach slightly, i.e., by including radially weighted distributions of the stabilisation number.

The second class is closely related to the physical exchange process between vortex and boundary layer. The exact role which momentum transfer and entrainment play in this process, is, at present, corroborated speculation. Precise measurements of the unsteady small-scale interactions and fully scale-resolving simulations will be necessary to further substantiate the assumptions made and conclusions drawn from these. The data obtained through such experiments could validate the predictive performance of the calculation method proposed and allow its application as a diffuser-design tool. Likewise, the potential insight gained could be transferred to different diffuser types and other components of turbomachines where vortices and boundary layers interact.

The third class, which is about possible applications of the theory proposed, can be reduced to the question of how the correlations and calculation methods presented could be integrated into cycle simulations on a system level. These simulations would, in tandem with an empirical data base for various diffuser types, facilitate not only cycle optimisations but also the optimisation of the individual contributions of the annular and conical diffuser to the overall pressure recovery.

The theory proposed, by virtue of its validity and simplicity, appears to be a
promising framework for improving the understanding and predictability of
turbine–diffuser interactions.

Bibliography

Andres, K. (1909): Versuche über die Umsetzung von Wassergeschwindigkeit in Druck. Verein deutscher Ingenieure. In German.

Babu, M.; Bhatia, D.; Shukla, R. K.; Pradeep, A. M. and Roy, B. (2011): Effect of Turbine Tip Leakage Flows on Exhaust Diffuser Performance. In: Proc. ASME Turbo Expo. pp. 609–618. doi:10.1115/GT2011-45457. Paper No. GT2011-45457.

Bardili, W.; Notter, O.; Betz, B. and Ibel, G. (1939): Wirkungsgrad von Diffusoren. In: Bericht des Flugtechnischen Instituts an der Technischen Hochschule Stuttgart, pp. 691–697. In German.

Bardina, J.; Kline, S. J. and Ferziger, J. (1982): Computation of Straight Diffusers at Low Mach Number Incorporating an Improved Correlation for Turbulent Detachment and Reattachment. Heat Transfer and Turbulence Mechanics Group/Thermosciences Division, Stanford University.

Bardina, J.; Lyrio, A.; Kline, S. J.; Ferziger, J. H. and Jonston, J. P. (1981): A Prediction Method for Planar Diffuser Flows. In: ASME J. Fluids Eng., Vol. 103(2):pp. 315–321. doi:10.1115/1.3241739.

Boussinesq, J. (1903): Théorie analytique de la chaleur mise en harmonie avec la thermodynamique et avec la théorie mécanique de la lumière. Gauthier-Villars, Paris, France. In French.

Brown, A. C.; Nawrocki, H. F. and Paley, P. N. (1968): Subsonic Diffusers Designed Integrally with Vortex Generators. In: J. Aircraft, Vol. 5(3):pp. 221–229. doi:10.2514/3.43931.

Childs, R. (1981): A Prediction Method for Planar Compressible Diffusers. Ph.D. Thesis, Stanford University, US.

Cochran, D. L. and Kline, S. J. (1958): Use of Short Flat Vanes for Producing Efficient Wide-angle Two-dimensional Subsonic Diffusers. National Advisory Committee for Aeronautics.

Coles, D. E. (1956): The Law of the Wake in the Turbulent Boundary Layer. In: J. Fluid Mech., Vol. 1(2):pp. 191–226. doi:10.1017/S0022112056000135.

Coles, D. E. (1962): The Turbulent Boundary Layer in a Compressible Fluid. RAND Corp.

Crocco, L. (1937): Eine neue Stromfunktion für die Erforschung der Bewegung der Gase mit Rotation. In: Z. angew. Math. Mech., Vol. 17(1):pp. 1–7. doi:10.1002/zamm.19370170103. In German.

Cutler, A. D. and Bradshaw, P. (1993a): Strong vortex/boundary layer interactions – Part I. Vortices high. In: Experiments in Fluids, Vol. 14:pp. 321–332. doi:10.1007/BF00189490.

Cutler, A. D. and Bradshaw, P. (1993b): Strong vortex/boundary layer interactions – Part II. Vortices low. In: Experiments in Fluids, Vol. 14:pp. 393–401. doi:10.1007/BF00190193.

Drechsel, B.; Müller, C.; Herbst, F. and Seume, J. R. (2015): Influence of Turbulent Flow Characteristics and Coherent Vortices on the Pressure Recovery of Annular Diffusers Part B: Scale-Resolving Simulations. In: Proc. ASME. 56635. Vol. 2A, pp. V02AT38A010:1–13. doi:10.1115/GT2015-42477. Paper No. GT2015-42477.

Drechsel, B.; Seume, J. R. and Herbst, F. (2016): On the Numerical Prediction of the Influence of Tip Flow on Diffuser Stability. In: International Journal of Gas Turbine, Propulsion and Power Systems (JGPP), Vol. 8(3):pp. 29–38.

Egorov, Y. and Menter, F. (2008): Development and Application of SST-SAS Turbulence Model in the DESIDER Project. doi:10.1007/978-3-540-77815-8. Papers contributed to the 2007 Symposium of Hybrid RANS-LES Methods, Corfu, Greece, 17-18 June 2007.

ESDU (1977): Performance of circular annular diffusers in incompressible flow. Engineering Sciences Data Unit, London, UK. ISBN 0 85679 130 X. No. 75026.

Farokhi, S. (1987): A Trade-Off Study of the Rotor Tip Clearance Flow in a Turbine/Exhaust Diffuser System. In: Proceedings of ASME 1987 International Gas Turbine Conference and Exhibition. Anaheim, California, USA. doi:10.1115/87-GT-229. Paper No. 87-GT-229.

Feynman, R. P.; Leighton, R. B. and Sands, M. (1965): The Feynman Lectures on Physics, Vol. 3. Addison-Wesley.

Fleige, H.-U. (2002): Experimentelle und numerische Untersuchungen am Modell eines Turbinenaustrittsdiffusors. Ph.D. Thesis, Leibniz Universität Hannover, Germany. In German.

Fleige, H.-U. and Riess, W. (2001): Investigations of Gas Turbine Exhaust Diffuser Flows. In: 4th European Conference on Turbomachinery. pp. 665–674. Paper No. ATI-CST-057/01.

Fröhlich, J. and von Terzi, D. (2008): Hybrid LES/RANS methods for the simulation of turbulent flows. In: Prog. Aerosp. Sci., Vol. 44(5):pp. 349–377. doi:10.1016/j.paerosci.2008.05.001.

Gibson, A. H. (1910): On the Flow of Water through Pipes and Passages having Converging or Diverging Boundaries. In: Proc. R. Soc. Lond. A, Vol. 83(563):pp. 366–378. doi:10.1098/rspa.1910.0025.

Gruschwitz, E. (1931): Die turbulente Reibungsschicht in ebener Strömung bei Druckabfall und Druckanstieg. In: Ingenieur-Archiv, Vol. 2:pp. 321–348. doi:10.1007/978-3-662-41363-0. In German.

Hall, M. G. (1966): The structure of concentrated vortex cores. In: Progress in Aerospace Sciences, Vol. 7:pp. 53–110. doi:10.1016/0376-0421(66)90006-6.

Hamel, G. (1917): Spiralförmige Bewegungen zäher Flüssigkeiten. In: Jahresbericht Deutsche Mathematiker-Vereinigung, Vol. 25:pp. 34–60. In German.

Hamel, G. (1941): Über die Potentialströmung zäher Flüssigkeiten. In: Z. angew. Math. Mech., Vol. 21:pp. 129–139. doi:10.1002/zamm.19410210301. In German.

Head, M. R. (1958): Entrainment in the Turbulent Boundary Layer. Aeronautics Research Council.

Hoadley, D. (1970): Three-Dimensional Turbulent Boundary Layers in an Annular Diffuser. Ph.D. Thesis, Cambridge University, UK.

Hoffmann, J. A. (1981): Effects of Free-Stream Turbulence on Diffuser Performance. In: ASME J. Fluids Eng., Vol. 103(3):pp. 385–390. doi:10.1115/1.3240795.

Hoffmann, J. A. and Gonzalez, G. (1984): Effects of Small-Scale, High Intensity Inlet Turbulence on Flow in a Two-Dimensional Diffuser. In: ASME J. Fluids Eng., Vol. 106(2):pp. 121–124. doi:10.1115/1.3243087.

Howard, J. H. G.; Henseler, J. H. and Thornton-Trump, A. B. (1967): Performance and Flow Regimes for Annular Diffusers. In: ASME Winter Annual Meeting. Paper No. 67-WA/FE-21.

Johnston, J. P. (1998): Review: Diffuser Design and Performance Analysis by a Unified Integral Method. In: ASME J. Fluids Eng., Vol. 120(1):pp. 6–18. doi:10.1115/1.2819663.

Kline, S. J. (1978): Diffuser - Flow Phenomena and Design. Darthmouth College.

Kluss, D.; Stoff, H. and Wiedermann, A. (2009): Effect of Wakes and Secondary Flow on Re-attachment of Turbine Exit Annular Diffuser Flow. In: ASME J. Turbomach., Vol. 131(4):pp. 041012:1–12. doi:10.1115/1.3070577.

Kožulović, D. and Röber, T. (2006): Modelling the Streamline Curvature Effects in Turbomachinery Flows. In: Proc. ASME Turbo Expo. pp. 1239–1248. doi:10.1115/GT2006-90265. Paper No. GT2006-90265.

Kuschel, M. (2014): Einfluss von Sekundärströmungen auf den Druckrückgewinn in Axialdiffusoren. Ph.D. Thesis, Leibniz Universität Hannover, Germany. In German.

Kuschel, M.; Drechsel, B.; Kluss, D. and Seume, J. R. (2015): Influence of Turbulent Flow Characteristics and Coherent Vortices on the Pressure Recovery of Annular Diffusers Part A: Experimental Results. In: Proc. ASME. 56635. Vol. 2A, pp. V02AT38A009:1–13. doi:10.1115/GT2015-42476. Paper No. GT2015-42476.

Lamb, H. (1932): Hydrodynamics. Cambridge University Press, Cambridge, UK.

Langston, L. S. (2001): Secondary Flows in Axial Turbines–A Review. In: Annals of the New York Academy of Sciences, Vol. 934:pp. 11–26. doi:10.1111/j.1749-6632.2001.tb05839.x.

Lohmann, R. P.; Markowski, S. J. and Brookmann, E. T. (1979): Swirling Flow Through Annular Diffusers with Conical Walls. In: ASME J. Fluids Eng., Vol. 101(2):pp. 224–229. doi:10.1115/1.3448939.

Ludwieg, H. and Tillmann, W. (1949): Untersuchungen über die Wandschubspannung in turbulenten Reibungsschichten. In: Ingenieur-Archiv, Vol. 17:pp. 288–299. In German.

Lyrio, A. A.; Ferziger, J. H. and Kline, S. J. (1981): An Integral Method for the Computation of Steady and Unsteady Turbulent Boundary Layer Flows, Including the Transitory Stall Regime in Diffusers. Heat Transfer and Turbulence Mechanics Group/Thermosciences Division, Stanford University.

McAlister, K. W. and Takahashi, R. K. (1991): NACA 0015 Wing Pressure and Trailing Vortex Measurements. National Aeronautics and Space Administration.

Menter, F. R. (1994): Two-Equation Eddy-Viscosity Turbulence Models for Engineering Applications. In: AIAA Journal, Vol. 32(8):pp. 1598–1605. doi:10.2514/3.12149.

Menter, F R and Egorov, Y (2010): The Scale-Adaptive Simulation Method for Unsteady Turbulent Flow Predictions. Part 1: Theory and Model Description. In: Flow Turbulence Combust., Vol. 85(1):pp. 113–138. doi:10.1007/s10494-010-9264-5.

Menter, F. R.; Kuntz, M. and Langtry, R. (2003): Ten years of industrial experience with the SST model. In: Turbulence, Heat and Mass Transfer, Vol. 4.

Mihailowitsch, M.; Schatz, M. and Vogt, D. M. (2018): Numerical Investigations of an Axial Exhaust Diffuser Coupling the Last Stage of a Generic Gas Turbine. In: ASME J. Eng. Gas Turbines Power, Vol. 141(3). doi:10.1115/1.4040769. Paper No. GTP-18-1305.

Mimic, D.; Drechsel, B. and Herbst, F. (2018a): Correlation between Pressure Recovery of Highly Loaded Annular Diffusers and Integral Stage Design Parameters. In: ASME J. Turbomach., Vol. 140(7):p. 071002. doi:10.1115/1.4039821. Under license CC-BY 4.0.

Mimic, D.; Jätz, C. and Herbst, F. (2018b): Correlation between total pressure losses of highly loaded annular diffusers and integral stage design parameters. In: Journal of the Global Power and Propulsion Society, Vol. 2:pp. 388–401. doi:10.22261/JGPPS.I9AB30.

Mimic, D.; Jätz, C.; Sauer, P. and Herbst, F. (2018c): Increasing Boundary Layer Stability for Varying Degrees of Diffuser Loading. In: Proc. GPPS. doi:10.5281/zenodo.1345494. Paper No. GPPS-2018-0006.

Mimic, D.; Jätz, C.; Sauer, P. and Herbst, F. (2019): Total Pressure Loss Reduction in Annular Diffusers. In: International Journal of Gas Turbine, Propulsion and Power Systems (JGPP), Vol. 10(2).

Moore, C. A. and Kline, S. J. (1958): Some Effects of Vanes and of Turbulence in Two-Dimensional Wide-Angle Subsonic Diffusers. National Advisory Committee for Aeronautics.

Morsbach, C. (2016): Reynolds Stress Modelling for Turbomachinery Flow Applications. Ph.D. Thesis, Technische Universität Darmstadt, Germany.

Oliphant, T. E. (2006): A guide to NumPy, Vol. 1. Trelgol Publishing USA.

Oseen, C. W. (1911): Über Wirbelbewegung in einer reibenden Flüssigkeit. In: Arkiv för Matematik, Astronomi och Fysik, Vol. 7(14). In German.

Owen, P. R. (1964): The decay of a turbulent trailing vortex. Unpublished report.

Panton, R. L. (2013): Incompressible Flow. John Wiley & Sons, Inc.

Patterson, G. N. (1938): Modern Diffuser Design: The Efficient Transformation of Kinetic Energy to Pressure. In: Aircraft Engineering and Aerospace Technology. doi:10.1108/eb030365.

Pöhler, T. (2013): Aerodynamische Auslegung und Analyse wirkungsgradoptimierter 3D-Gestaltungen für die Leit- und Laufbeschaufelung einer subsonischen Axialturbine. Ph.D. Thesis, RWTH Aachen University, Germany. In German.

Pohlhausen, K. (1921): Zur Näherungsweisen Integration der Differentialgleichung der laminaren Grenzschicht. In: Z. angew. Math. Mech., Vol. 1(4):pp. 252–290. doi:10.1002/zamm.19210010402. In German.

Popper, K. R. (1994): Alles Leben ist Problemlösen. Piper, München, Germany. 1996 reprint. In German.

Prandtl, L. (1904): Über Flüssigkeitsbewegungen bei sehr kleiner Reibung. In: Verhandlungen des III. Internationalen Mathematiker-Kongresses zu Heidelberg. In German.

Quest, J. and Scholz, N. (1980): Experimentelle Untersuchungen von Nabendiffusoren hinter Turbinen. Deutsche Forschungs- und Versuchsanstalt für Luft- und Raumfahrt e. V. In German.

Reneau, L. R.; Johnston, J. P. and Kline, S. J. (1967): Performance and Design of Straight, Two-Dimensional Diffusers. In: ASME J. Basic Eng. doi:10.1115/1.3609544.

Schlichting, H. and Gersten, K. (2006): Grenzschicht-Theorie. Springer, Berlin Heidelberg, Germany. In German.

Schlichting, H. and Truckenbrodt, E. (2001): Aerodynamik des Flugzeuges, Vol. 1. Springer, Berlin Heidelberg, Germany. In German.

Senoo, Y. and Nishi, M. (1974): Improvement of the Performance of Conical Diffusers by Vortex Generators. In: ASME J. Fluids Eng., Vol. 96(1):pp. 4–10. doi:10.1115/1.3447097.

Senoo, Y. and Nishi, M. (1977a): Deceleration Rate Parameter and Algebraic Prediction of Turbulent Boundary Layer. In: ASME J. Fluids Eng., Vol. 99(2):pp. 390–394. doi:10.1115/1.3448771.

Senoo, Y. and Nishi, M. (1977b): Prediction of Flow Separation in a Diffuser by a Boundary Layer Calculation. In: ASME J. Fluids Eng., Vol. 99(2):pp. 379–386. doi:10.1115/1.3448767.

Sieker, O. (2010): Einfluss von Drall und Nachlaufdellen auf das Strömungsverhalten und den Druckrückgewinn in axialen Turbinenaustrittsdiffusoren. Ph.D. Thesis, Leibniz Universität Hannover, Germany. In German.

SIEKER, O. AND SEUME, J. R. (2008a): Effects of Rotating Blade Wakes on Separation and Pressure Recovery in Turbine Exhaust Diffusers. In: Proc. ASME Turbo Expo. doi:10.1115/GT2008-50788. Paper No. GT2008-50788.

SIEKER, O. AND SEUME, J. R. (2008b): Influence of rotating wakes on separation in turbine exhaust diffusers. In: J. Therm. Sci., Vol. 17(1):pp. 42–49. doi:10.1007/s11630-008-0042-9.

SIEVERDING, C. H. (1985): Recent Progress in the Understanding of Basic Aspects of Secondary Flows in Turbine Blade Passages. In: J. Eng. Gas Turbines Power, Vol. 107(2):pp. 248–257. doi:10.1115/1.3239704.

SOVRAN, G. AND KLOMP, D. (1967): Experimentally determined Optimum Geometries for Rectilinear Diffusers with Rectangular Conical or Annular Cross-Section. In: Fluid Mech. Int. Flow, pp. 270–319.

STRELETS, M. (2001): Detached Eddy Simulation of Massively Separated Flows. In: 39th AIAA Aerospace Sciences Meeting and Exhibit. Reno, NV. Paper No. AIAA 2001-0879.

SUTHERLAND, W. (1893): LII. The viscosity of gases and molecular force. In: Philosophical Magazine Series 5, Vol. 36(223):pp. 507–531. doi:10.1080/14786449308620508.

THOMAS, R.; SCHATZ, M.; KUSCHEL, B.; BROUWER, S.; PRADEEP, A. M.; VOGT, D. AND ROY, B. (2015): Influence of Tip Jet Mass Flow and Blowing Rate on the Performance of an Axial Diffuser at Different Inlet Total Pressure Profiles. In: Proc. ASME Turbo Expo. doi:10.1115/GT2015-43427. Paper No. GT2015-43427.

TRAUPEL, W. (2001): Thermische Turbomaschinen, Vol. 1. Springer-Verlag. In German.

VAN DER WALT, S.; COLBERT, S. C. AND VAROQUAUX, G. (2011): The NumPy array: a structure for efficient numerical computation. In: Computing in Science & Engineering, Vol. 13(2):p. 22.

VAN ROSSUM, G. (2020): The Python Library Reference, release 3.8.2. Python Software Foundation.

VAN ROSSUM, G. AND DRAKE, F. L. (2009): Python 3 Reference Manual. CreateSpace, Scotts Valley, CA. ISBN 1441412697.

VASSILIEV, V.; IRMISCH, S.; CLARIDGE, M. AND RICHARDSON, M. (2003): Experimental and Numerical Investigation of the Impact of Swirl on the Performance of Industrial Gas Turbines Exhaust Diffusers. In: Proc. ASME 36894. Vol. 6, pp. 19–29. doi:10.1115/GT2003-38424. Paper No. GT2003-38424.

VASSILIEV, VLADIMIR; IRMISCH, STEFAN; ABDEL-WAHAB, SAMER AND GRANOVSKIY, ANDREY (2011): Impact of the Inflow Conditions on the Heavy-Duty Gas Turbine Exhaust Diffuser Performance. In: ASME J. Turbomach., Vol. 134(3). doi:10.1115/1.4003714.

VELDMAN, A. E. P. (2017): Entrainment and boundary-layer separation: a modeling history. In: J. Eng. Math., Vol. 107:pp. 5–17. doi:10.1007/s10665-017-9930-x.

VENTURI, J. B. (1797): Recherches experiméntales sur le principe de la communication latèrale du mouvement dans les fluides appliqué à l'explication de différens phenomènes hydrauliques. Houel et Ducros, Paris, France. In French.

Virtanen, P.; Gommers, R.; Oliphant, T. E.; Haberland, M.; Reddy, T.; Cournapeau, D.; Burovski, E.; Peterson, P.; Weckesser, W.; Bright, J.; van der Walt, S. J.; Brett, M.; Wilson, J.; Millman, K. J.; Mayorov, N.; Nelson, A. R. J.; Jones, E.; Kern, R.; Larson, E.; Carey, C. J.; Polat, İ.; Feng, Y.; Moore, E. W.; VanderPlas, J.; Laxalde, D.; Perktold, J.; Cimrman, R.; Henriksen, I.; Quintero, E. A.; Harris, C. R.; Archibald, A. M.; Ribeiro, A. H.; Pedregosa, F.; van Mulbregt, P. and SciPy 1.0 Contributors (2020): SciPy 1.0: Fundamental Algorithms for Scientific Computing in Python. In: Nature Methods, Vol. 17:pp. 261–272. doi:10.1038/s41592-019-0686-2.

von Doehnhoff, A. E. and Tetervin, N. (1943): Determination of General Relations for the Behavior of Turbulent Boundary Layers. National Advisory Committee for Aeronautics.

von Helmholtz, H. (1858): Über Integrale der hydrodynamischen Gleichungen, welche den Wirbelbewegungen entsprechen. In: Journal für die reine und angewandte Mathematik, Vol. 55:pp. 25–55. doi:10.1515/crll.1858.55.25. In German.

von Kármán, T. (1921): Über laminare und turbulente Reibung. In: Z. angew. Math. Mech., Vol. 1(4):pp. 233–252. doi:10.1002/zamm.19210010401. In German.

Willinger, R. and Haselbacher, H. (1998): The Role of Rotor Tip Clearance on the Aerodynamic Interaction of a Last Gas Turbine Stage and an Exhaust Diffuser. In: Proc. ASME Turbo Expo. doi:10.1115/98-GT-094. Paper No. 98-GT-94.

Zimmerman, C. and Stetter, H. (1993): Einfluß der Radialspiele auf die Diffusorströmung und den Wirkungsgrad einer ND-Modellturbine. In: VGB Kraftwerkstechnik, Vol. 73(8):pp. 690–695. In German.

Appendix A.

Diffuser-prediction program

The program GammaDiff was implemented in Python 3.8.3rc1 to predict the performance of planar diffusers and annular diffusers under the influence of a circumferentially oriented Lamb-Oseen vortex which can be imposed at the inlet. The program was adapted from Bardina et al. (1982) where a detailed discussion of most procedures can be found.

The calibration constants for the vortex model and its interaction with the boundary-layer model were chosen as $c_\Omega = 1.1$ (`C_VORT` in the program), $c_E = 2.03$ (`C_ENTR` in the program), and $c_{\mathrm{d}\Gamma} = 22$ (`C_DGAM` in the program). Additionally, for the analyses presented in *Sec.* 6.1.4, the inlet blockage factor and boundary-layer blockage factor were chosen as $B = 0.05$ and $\Lambda = 0.215$ for the 15° diffuser and $B = 0.06$ and $\Lambda = 0.36$ for the 20° diffuser in order to reproduce the experimentally observed variations in the effectiveness in both test cases. The displacement-thickness Reynolds number, $\mathrm{Re}_{\delta^*} := \mathcal{U}_{\mathrm{in}}\delta^*/\nu$, was set to 3000; the kinematic viscosity used to determine the vortex Reynolds number, which in turn determines the vortex decay, was set to $1.5 \times 10^{-5}\,\mathrm{m^2/s}$. The position of the centreline of the prescribed vortex was assumed at 99.3 % of the diffuser channel height to mimic the tip gap of the rotor used in this work. A few other input parameters together with their numerical values are commented in the code.

The fourth/fifth-order Runge–Kutta solver RK45, included in the Python library SciPy (see Virtanen et al. 2020), is used to numerically integrate the set of ordinary differential equations. Further information regarding other libraries used in the program can be found in Oliphant (2006), Van Der Walt et al. (2011), and Van Rossum and Drake (2009); information regarding Python is given in Van Rossum (2020). *Listing* A.1 shows the complete program code, including detailed comments.

Listing A.1: Diffuser-prediction program GammaDiff

```
#!/usr/bin/env python3
# -*- coding: utf-8 -*-
"""
gammadiff.py: This program predicts the performance of planar diffusers
and annular diffusers under the influence of a circumferentially oriented
vortex at the inlet.

@version: 1.0

@author:        Dajan Mimic
@organization:  Institute of Turbomachinery and Fluid Mechanics,
                Leibniz Universitaet Hannover
@contact:       mimic@tfd.uni-hannover.de,
                An der Universitaet 1, 30823 Garbsen, Germany
```

```
@note: This program is issued as part of the doctoral thesis:
       Mimic, D. (2020): Turbine-Diffuser Interaction. Ph.D. Thesis,
       Leibniz Universitaet Hannover, Germany.

@note: This program is represents an adapted implementation of the programs
       PLANDIFF and AXIDIFF by Juan Bardina (1978), originally written in
       Fortran and issued together with the report:
       Bardina, J.; Kline, S.J.; Ferziger, J. (1982): Computation of Straight
       Diffusers at Low Mach Number Incorporating an Improved Correlation for
       Turbulent Detachment and Reattachment. Report PD-22. Heat Transfer and
       Turbulence Mechanics Group/Thermosciences Division, Stanford University.

@note: The adaptations comprise (ordered from general to specific):
       - Implementation in Python
       - Functional programming
       - General adaptations to the data input/output interfaces
       - A 4th/5th-order accuracy Runge-Kutta from the scipy library (rk45) is
         used instead of the 4th/5th-order accuracy Runge-Kutta-Fehlberg
         implementation in Fortran.
       - Adaptations of the model equations to predict the behaviour of annular
         diffusers with constant hub and diverging casing in the functions
         - calc_ODE_coeff_LHS_RHS1(...),
         - calc_ODE_coeff_RHS2(...), and
         - limit_entrainment(...).
       - A method is implemented which imposes a Lamb-Oseen vortex with
         circumferentially oriented rotational axis at the inlet. The vortex
         interacts with the other model equations in order to influence the
         boundary-layer behaviour. The vortex model is implemented in the
         functions
         - update_circulation(...),
         - convect_vortex(...),
         - calc_vortex_strainrate(...), and
         - calc_vortex_shear(...).

@note: The code is organised in the following sections:
       - input data
       - numerical and solver settings
       - constants
       - boundary and initial conditions
       - model parameters
       - function definitions
         - general tasks
         - diffuser model
         - vortex model
         - solver
       - execution
         - solver call
         - output
"""

#-----------------------------------------------------------------------------
#%% imports
import math
import numpy as np
```

```
from types import SimpleNamespace as sns
from scipy.integrate import solve_ivp

#------------------------------------------------------------------------------
#%% input data
## geometric boundary conditions of the diffuser
# diffuser type: 'planar' or 'annular'
diffuserType                      = 'annular'
# half-opening angle in deg:
halfOpeningAngleDeg               = 15
# diffuser length / inlet width:
nonDimDiffuserLength              = 1.9944
# length of straight inlet pipe / inlet width:
nonDimInletLength                 = 0
# length of straight tailpipe / inlet width:
nonDimTailPipeLength              = 0.0
# inlet radius at the midspan / inlet width:
nonDimInletMidspanRadius          = 1.8448

# initial conditions of the boundary layer
# 2 * inlet displacement thickness / inlet width:
inletDiffuserBlockage             = 0.05
# inletDisplacementThickness / inletBoundaryLayerThickness:
inletBoundaryLayerBlockage        = 0.215
# inletVelocity * inletDisplacementThickness / kinematicViscosity:
inletDisplacementReynoldsNumber = 3000.0

## initial conditions of the vortex
# non-dimensional circulation of Lamb-Oseen vortex:
inletCirculation                  = 0.0
# relative spanwise position of vortex (decimal value)
# of half width for 'planar',
# of width for 'annular':
nonDimSpanwisePosition            = 0.993
# kinematic molecular viscosity for vortex reynolds number
kinViscosityMol                   = 1.5e-5

#------------------------------------------------------------------------------
#%% DO NOT CHANGE PART BELOW!

#------------------------------------------------------------------------------
#%% numerical and solver settings
RES       = 11                            # spatial resolution for rk45 solver
ABS_ERROR = [1e-7, 1e-7, 1e-7, 1e-7]  # abs. error for rk45 solver
REL_ERROR = 1e-2                          # rel. error for rk45 solver
MAX_STEP  = 1e-1                          # max. integration step size

INT_START = -nonDimInletLength                            # integration start
INT_END   = nonDimDiffuserLength + nonDimTailPipeLength  # integration end
X_EVAL = np.linspace(INT_START, INT_END, RES)            # evaluated points

#------------------------------------------------------------------------------
#%% constants
PI             = math.pi
VON_KARMAN     = 0.41  # von-Karman constant
VON_KARMAN_SQR = VON_KARMAN * VON_KARMAN
```

```
LAMBDA_VORT    = 0.35  # relates turbulent kinematic viscosity in vortex to
                       # circulation and molecular viscosity,
                       # see Hall, M.G. (1966): The structre of concentrated
                       # vortex cores. In: Progress in Aerospace Sciences.

#-------------------------------------------------------------------------------
#%% boundary and initial conditions
# assign input parameters to variables for convenience in program

# geometric boundary conditions
D_TYPE  = diffuserType
THETA   = math.radians(halfOpeningAngleDeg)
W_IN    = 1.0                 # non-dimensional inlet width; 1 by definition
N_IN    = nonDimInletLength
N_D     = nonDimDiffuserLength
N_OUT   = nonDimTailPipeLength
RM_IN   = nonDimInletMidspanRadius

# initial flow conditions
B_IN    = inletDiffuserBlockage / 2.0
L_IN    = inletBoundaryLayerBlockage
U_IN    = 1.0          # non-dimensional inlet flow velocity; 1 by definition
RE_D_IN = inletDisplacementReynoldsNumber

# initial vortex conditions
G_IN    = inletCirculation
WV_IN   = nonDimSpanwisePosition

# general properties
NUM     = kinViscosityMol                          # kin. molecular viscosity
NUT     = LAMBDA_VORT * math.sqrt(abs(G_IN) * NUM)  # kin. turbulent viscosity
NU      = NUM + NUT                                # effective kin. viscosity
RE_V    = U_IN * (N_IN + N_D + N_OUT) / NU         # vortex Reynolds number

#-------------------------------------------------------------------------------
#%% model parameters
V_ONOFF = 1      # vortex model: 1 = on, 0 = off
C_VORT  = 1.1    # momentum exchange between vortex and boundary layer: 1.1
C_ENTR  = 2.03   # mass exchange between vortex and boundary layer: 2.03
C_DGAM  = 22     # circulation decrease due to interaction between vortex and
                 # boundary layer: 22
T_IN    = 0.001  # initial vortex time: this gives an initial amount of vortex
                 # diffusion and ensures a smooth velocity distribution

#-------------------------------------------------------------------------------
#%% function definitions
npi  = lambda   x: x * PI
sign = lambda   x: math.copysign(1, x)
sqr  = lambda   x: (x * x)

sqrt = lambda   x: math.sqrt(x)
exp  = lambda   x: math.exp(x)
ln   = lambda   x: math.log(x)

sin  = lambda rad: math.sin(rad)
cos  = lambda rad: math.cos(rad)
```

```
tan  = lambda rad: math.tan(rad)
atan = lambda   x: math.atan(x)

#-------------------------------------------------------------------------------
#%% general tasks
def unpack_solution_vector(y):
    """Unpack the solution vector"""

    #dependent variables:
    y = {#boundary layer
         'B' : y[0],  # (half) blockage:
                      # B = displacement thickness / diffuser width
         'L' : y[1],  # boundary-layer blockage:
                      # L(ambda) = displacement thickness / bl thickness
         #vortex
         'G' : y[2],
         't' : y[3],  # solution time: SUM(dx_i/U_i); see def convect_vortex()
         }

    return y


def init_output():
    """Initialise output vector as dictionary"""

    # define dictionary with output arrays
    output = {'x'     : [],
              #
              'B'     : [],
              'L'     : [],
              'G'     : [],
              #
              'cpi'   : [],
              'cp'    : [],
              'eff'   : [],
              #
              'Cf'    : [],
              'H'     : [],
              #
              'blt'   : [],  # boundary-layer thickness
              'blt_d' : [],  # displacement thickness
              'blt_m' : [],  # momentum thickness
              }

    return output


def gen_output(output, x, y, geom, flow, bounlay):
    """Add new output to dictionary"""

    out = sns(**output)

    out.x.append(x)

    out.B.append(y['B'])
    out.L.append(y['L'])
```

```
    out.G.append(y['G'])

    out.cpi.append(geom['cpi'])
    out.cp.append(flow['cp'])
    out.eff.append(flow['cp'] / geom['cpi'])

    out.Cf.append(bounlay['Cf'])
    out.H.append(bounlay['H'])

    out.blt.append(y['L'] * y['B'] * geom['W'])
    out.blt_d.append(y['B'] * geom['W'])
    out.blt_m.append(y['B'] * geom['W'] / bounlay['H'])

    pass


def eval_output(output):
    """Evaluate the output vector"""

    output_eval = {}

    for key in output:
        key_eval = np.interp(X_EVAL, output['x'], output[key])
        output_eval.update({key: key_eval})

    return output_eval

#-----------------------------------------------------------------------------
#%% diffuser model
def calc_geom(x):
    """Calculate diffuser width 'W', change in width 'dW', and ideal
       static-pressure recovery coefficient 'cpi' as a function of the
       stream-wise coordinate 'x'; return as dictionary 'geom'"""

    Wr = 1.0 + 2.0 * N_D * tan(THETA)  # width ratio of diffuser

    if x >= N_D / cos(THETA):
        W = Wr
        dW = 0.0
    elif x > 0.0:
        W = THETA * (2.0 * x + 1.0 / sin(THETA))
        dW = 2.0 * THETA
        if W >= Wr:
            W = Wr
            dW = 0.0
    else:
        W = 1.0
        dW = 0.0

    # ideal pressure-recovery coefficient
    if D_TYPE == 'planar':
        cpi = 1 - sqr(W_IN / W)
    elif D_TYPE == 'annular':
        cpi = 1 - sqr((W_IN * RM_IN) / ((W_IN + 1.0 * x * sin(THETA)) * \
              (RM_IN + x * sin(THETA/2) )))
```

```
    geom = {'W': W,
            'dW': dW,
            'cpi': cpi,
            }

    return geom


def calc_flow(x, y, geom):
    """Calculate non-dimensional flow velocity U, displacement-thickness
       Reynolds number ReD, and static-pressure recovery coefficient cp;
       return as dictionary 'flow'"""

    y = sns(**y)
    g = sns(**geom)

    U = (1.0 - 2.0 * B_IN) / (1.0 - 2.0 * y.B) / g.W
    ReD = RE_D_IN * U * g.W * y.B / B_IN
    cp = 1.0 - sqr(U)

    flow = {'U': U,
            'ReD': ReD,
            'cp': cp
            }

    return flow

#-------------------------------------------------------------------------------
#%% boundary-layer model
def calc_bl_state(y, flow):
    """Calculate the boundary-layer state in terms of shear-stress velocity
       'VT', boundary-layer shape parameter 'Sh', skin-friction coefficient
       'Cf', and shape factor 'H'; return as dictionary 'bounlay'"""

    y = sns(**y)
    f = sns(**flow)

    c1 = 0.885
    c2 = 0.115
    c3 = 1.5894898556

    VT = 0.44 * sign(1.0 - 2.0 * y.L) * pow(abs(1.0 - 2.0 * y.L), c1) * \
         pow(y.L / f.ReD, c2)
    Sh = 1.5 * y.L + (2.0 * c3 - 3.0) * VT + (3.5 - 2.0 * c3) * sqr(VT) / y.L

    Cf = 2.0 * VON_KARMAN_SQR * VT * abs(VT)
    H = 1.0 / (1.0 - Sh)

    bounlay = {'VT': VT,
               'Sh': Sh,
               'Cf': Cf,
               'H': H
               }

    return bounlay
```

```
def calc_max_shearstress_position(y, bounlay):
    """Calculate and return the non-dimensional wall-normal position of maximum
       shear stress in the boundary layer"""

    y = sns(**y)
    b = sns(**bounlay)

    if y.L >= 0.5: c1 = 1.3 * y.L - 0.4
    else: c1 = 0.24

    if b.VT >= 5.3212 * y.L - 3.117086 * c1:
        eta = 0.25
    else:
        eta = 2.0 * atan(sqrt(2.0 * y.L / c1 -1.0)) / PI - \
              0.006 * (1.0 / y.L - 2.0) / y.L

        # Newton's method
        while True:
            func = b.VT * ln(eta) - 2.0 * (y.L - b.VT) * \
                   sqr(cos(PI * eta / 2.0)) + c1
            d_func = b.VT / eta + PI * (y.L - b.VT) * sin(PI * eta)
            delta = func / d_func
            eta = eta - delta
            if abs(delta) < 1e-4: break
        # end Newton's method

    return eta


def calc_curvature_correction_AUX(B, L, W, dW):
    """Calculate the curvature-correction term"""

    if D_TYPE == 'planar' and dW > 0.0 and L < 0.5 and \
       THETA > 0.12: curv = 0.006 / W / B
    elif D_TYPE == 'annular' and dW > 0.0 and L < 0.5: curv = 0.006 / W /B
    else: curv = 0.0

    return curv


def calc_ODE_coeff_LHS_RHS1(y, geom, flow, bounlay, shear_coeff_v):
    """Calculate the coefficients 'a11', 'a12', 'a21', and 'a22' on the
       left-hand side of the ODE system; calculate the first coefficient 'b1'
       on the right-hand side of the ODE system"""

    y = sns(**y)
    g = sns(**geom)
    f = sns(**flow)
    b = sns(**bounlay)

    c1   = 1.5894898556
    c1_1 = 3.5 - 2.0 * c1
    c1_2 = 2.0 * c1 - 3.0
    c1_3 = 7.0 - 4.0 * c1
```

```
    curv = calc_curvature_correction_AUX(y.B, y.L, g.W, g.dW)

    coeff1 = 1.5 - c1_1 * sqr(b.VT / y.L) + (0.115 - 2.0 * y.L) / y.L * \
             (c1_2 + c1_3 * b.VT / y.L) * (0.3 + 0.4 * y.L) / pow(f.ReD, 0.115)
    coeff2 = 0.115 * (c1_2 * b.VT + c1_3 * sqr(b.VT) / y.L)

    a11 = (coeff2 + 1.0 - b.Sh) / y.B / (1.0 - 2.0 * y.B) + \
          (2.0 - b.Sh + curv / y.L) / (0.5 - y.B)
    a12 = coeff1
    a21 = 1.0 / (1.0 - 2 * y.B)
    a22 = y.B / y.L / (1.0 - y.L)

    b1 = VON_KARMAN_SQR * b.VT * abs(b.VT) / g.W / y.B + g.dW * \
         (2.0 - b.Sh + curv / y.L) / g.W

    if D_TYPE == 'annular':
        b1 -= (1.0 - b.Sh) * sin(THETA) /2 / RM_IN

    b1 -= shear_coeff_v

    ode_coeff = {'a11': a11,
                 'a12': a12,
                 'a21': a21,
                 'a22': a22,
                 'b1' : b1
                 }

    return ode_coeff


def calc_beta_coeff(B, dB, W, dW, VT):
    """Calculate coefficient beta"""

    beta = W * B * (2.0 * dB / (1.0 - 2.0 * B) - dW / W) / 15.0 / \
           VON_KARMAN_SQR / sqr(VT)
    beta = max(min(beta, 0), -30)

    return beta


def calc_ODE_coeff_RHS2(y, W, tau, entrain_coeff_v):
    y = sns(**y)

    b2 = 10.0 * tau * y.L / W / (1.0 - y.L)

    if D_TYPE == 'annular':
        b2 -= y.B * sin(THETA) /2 / RM_IN

    b2 += entrain_coeff_v

    return b2


def calc_dB(y, geom, ode_coeff, b2, flag):
    """Calculate the derivative of the blockage factor 'dB'"""
```

```
    y = sns(**y)
    g = sns(**geom)
    o = sns(**ode_coeff)

    if flag == 0:
        dB = (b2 * o.a12 - o.b1 * o.a22) / (o.a12 * o.a21 - o.a11 * o.a22)
    elif flag == 1:
        dB = g.dW * (1.0 -2.0 * y.B) / g.W / 2.0
    elif flag == 2:
        dB = o.b1 / o.a11

    return dB


def calc_dL(ode_coeff, b2, dB, flag):
    """Calculate the derivative of the boundary-layer blockage factor 'dL'"""

    o = sns(**ode_coeff)

    if flag == 0:
        dL = (b2 * o.a11 - o.b1 * o.a21) / (o.a12 * o.a21 - o.a11 * o.a22)
    elif flag == 1:
        dL = (o.a11 * dB - o.b1) / o.a12
    elif flag == 2:
        dL = 0.0

    return dL


def calc_shear_lag_equations(x, yy, geom, flow, bounlay, eta, ode_coeff,
                             entrain_coeff_v, state_prev):
    """Calculate the shear-lag equations"""

    y = sns(**yy)
    g = sns(**geom)
    f = sns(**flow)
    b = sns(**bounlay)
    prev = sns(**state_prev)


    dB = prev.dB
    tau0 = prev.tau
    funct0 = prev.funct
    dx = abs(x - prev.x)

    limiterFlag = 0  # no limiter active here

    tauEQ = 0.0168 * y.L * (b.VT / eta + PI * (y.L - b.VT) * sin(PI * eta))
    tauEQ /= 1.0 + 9.0 * pow(eta, 6.0)

    if x == -N_IN: tau0 = tauEQ

    if y.L >= 0.48:
        tauEQ = 0.13 * tauEQ / 0.168
        if g.dW == 0.0: tauEQ = tauEQ * (1.0 - y.L) / y.L
        tau = tauEQ
```

```
        b2 = calc_ODE_coeff_RHS2(yy, g.W, tau, entrain_coeff_v)
        dB = calc_dB(yy, geom, ode_coeff, b2, limiterFlag)
    elif g.dW == 0.0:
        tau = tauEQ * y.L * dx / (80.0 * g.W * y.B + dx * y.L)
        tau += (tau0 + dx * funct0 / 80.0) / \
               (1 + dx * y.L / 80.0 / g.W / y.B) * sqr(prev.U/f.U)
        b2 = calc_ODE_coeff_RHS2(yy, g.W, tau, entrain_coeff_v)
        dB = calc_dB(yy, geom, ode_coeff, b2, limiterFlag)
    else:
        tau1 = tauEQ
        while True:
            beta = calc_beta_coeff(y.B, dB, g.W, g.dW, b.VT)

            tau = tau1 * (0.013 + 0.0038 * exp(beta)) / 0.0168
            tau = tauEQ * y.L * dx / (80.0 * g.W * y.B + dx * y.L)
            tau += (tau0 + dx * funct0 / 80.0) / \
                   (1 + dx * y.L / 80.0 / g.W / y.B) * sqr(prev.U / f.U)

            if y.L <= 0.5 and y.B >= y.L / 2.0: tau = 0.0

            b2 = calc_ODE_coeff_RHS2(yy, g.W, tau, entrain_coeff_v)

            dB0 = dB
            dB = calc_dB(yy, geom, ode_coeff, b2, limiterFlag)

            if abs(dB0 - dB) < 1e-6: break

    funct0 = y.L * (tauEQ - tau) / g.W / y.B

    state_prev = {'x': x,
                  'U': f.U,
                  'tau': tau,
                  'funct': funct0,
                  'dB': dB
                  }

    dL = calc_dL(ode_coeff, b2, dB, limiterFlag)

    dy = {'dB': dB,
          'dL': dL,
          }

    return dy, b2, state_prev


def limit_entrainment(yy, geom, ode_coeff, b2, dy, state_prev):
    """Limit the entrainment rate"""

    y = sns(**yy)
    g = sns(**geom)
    o = sns(**ode_coeff)
    dy = sns(**dy)


    if y.L <= 0.42265 or g.dW == 0:
        limiterFlag = 0
```

```
        dB = dy.dB
        dL = dy.dL
    elif dy.dL > 0.0:
        if dy.dB <= g.dW * (1.0 - 2.0 * y.B) / 2.0 / g.W:
            dB = dy.dB
            dL = dy.dL
        else:
            limiterFlag = 1
            dB = calc_dB(yy, geom, ode_coeff, b2, limiterFlag)
            dL = calc_dL(ode_coeff, b2, dB, limiterFlag)
            if D_TYPE == 'planar':
                state_prev['tau'] = (o.a21 * dB - o.a22 * dL) * g.W * (1.0 -
                                    y.L) / 10.0 / y.L
            elif D_TYPE == 'annular':
                state_prev['tau'] = (o.a21 * dB - o.a22 * dL + y.B *
                                     sin(THETA) / 2 / RM_IN) * \
                                     g.W * (1.0 - y.L) / 10.0 / y.L
    else:
        limiterFlag = 2
        dB = calc_dB(yy, geom, ode_coeff, b2, limiterFlag)
        dL = calc_dL(ode_coeff, b2, dB, limiterFlag)
        if D_TYPE == 'planar':
            state_prev['tau'] = (o.a21 * dB) * g.W * (1.0 - y.L) / 10.0 / y.L
        elif D_TYPE == 'annular':
            state_prev['tau'] = (o.a21 * dB + y.B * sin(THETA) /2 / RM_IN) * \
                                g.W * (1.0 - y.L) / 10.0 / y.L

    dy = {'dB': dB,
          'dL': dL,
          }

    return dy, state_prev

#------------------------------------------------------------------------------
#%% vortex model
# G = Circulation
def update_circulation(u_tv, r, G):
    """Reduce the vortex circulation due to viscous interaction with the
       boundary layer"""

    if G >= 0:
        dG = - C_DGAM * u_tv * npi(2) * r
        print('DG', dG)
    else:
        dG = 0

    return dG


def convect_vortex(x, flow):
    """Convect the vortex, determine physical time step to calculate vortex
       decay"""

    f = sns(**flow)

    dt = 1 / f.U
```

```
    return dt


def calc_vortex_strainrate(t, r, G):
    """Calculate the strain rate induced by the vortex"""

    pot = G / npi(1) / np.square(r)
    gam = G * RE_V / npi(4) / t
    decay = np.exp(- sqr(r) * RE_V / 4.0 / t)

    strainrate_v = pot * (decay - 1.0) + gam * decay

    return strainrate_v


def calc_vortex_shear(y, geom):
    """Calculate the shear stress induced by the vortex at the location of
       maximum shear stress"""

    y = sns(**y)
    g = sns(**geom)
    r_rel_max_strainrate = 1.33913087

    if V_ONOFF != 0 and y.B >= ABS_ERROR[-2] and y.L >= ABS_ERROR[-2] and \
       y.G > 0:
        r_eval = (1 - WV_IN) * g.W / 2 - y.B
        r_max_strainrate = 2 * sqrt(y.t / RE_V) * r_rel_max_strainrate
        r = max(r_eval, r_max_strainrate)

        strainrate_v = calc_vortex_strainrate(y.t, r, y.G)
        shearstress_v = strainrate_v / RE_V # negative sign transforms from
                                            # vortex reference frame to
                                            # boundary-layer reference frame

        u_tv = - sign(shearstress_v) * sqrt(abs(shearstress_v))
        shear_coeff_v = C_VORT * 2 * VON_KARMAN_SQR * abs(u_tv) * u_tv
        entrain_coeff_v = C_ENTR * 2 * VON_KARMAN_SQR * abs(u_tv) * u_tv

        dG = update_circulation(u_tv, r, y.G)
    else:
        u_tv, shear_coeff_v, entrain_coeff_v, dG = 0, 0, 0, 0

    return u_tv, shear_coeff_v, entrain_coeff_v, dG

#------------------------------------------------------------------------------
#%% solver
def solver():
    """Call functions in appropriate order; call solver"""

    output = init_output()

    # init storage structure for state from previous iteration
    state_prev_stored = {# position
                         'x'    : INT_START,
                         # flow
```

```
                         'U'     : U_IN,
                         'tau'   : 0.0,
                         'funct': 0.0,
                         'dB'    : 0.0,
                         }

    # evaluate derivatives of dependent variables (y[])
    # for given independent variable (x)
    def eval_func(x, y):
        # read stored state from previous iteration
        # contains initial values of x, U, G
        nonlocal state_prev_stored
        state_prev = state_prev_stored

        # initialise and unpack data structures
        y = unpack_solution_vector(y)

        # all following functions are performed step-wise at each iteration

        # set up diffuser geometry
        geom = calc_geom(x)
        # compute free-stream and boundary-layer flow
        flow = calc_flow(x, y, geom)
        bounlay = calc_bl_state(y, flow)
        eta = calc_max_shearstress_position(y, bounlay)

        # compute vortex velocity gradient
        u_tv, shear_coeff_v, entrain_coeff_v, dG = calc_vortex_shear(y, geom)
        dt = convect_vortex(x, flow)

        # compute coefficients for ODE system
        # LHS: a11, a12, a21, a22;
        # RHS: b1; b2 will be computed in next function
        ode_coeff = calc_ODE_coeff_LHS_RHS1(y, geom, flow, bounlay,
                                            shear_coeff_v)

        # compute gradients of independent variables,
        # ODE coefficient b2 and previous state
        # for boundary layer
        dy, b2, state_prev = calc_shear_lag_equations(x, y, geom, flow,
                                                      bounlay, eta, ode_coeff,
                                                      entrain_coeff_v,
                                                      state_prev)
        # re-compute gradients and previous state
        # if required by entrainment limiter
        dy, state_prev = limit_entrainment(y, geom, ode_coeff, b2, dy,
                                           state_prev)

        # pack and store state for next iteration (nonlocal)
        state_prev_stored = state_prev

        # store output in output arrays (global)
        gen_output(output, x, y, geom, flow, bounlay)

        # pack gradients for output
        dy_tuple = dy['dB'] , dy['dL'], dG, dt
```

```
        return dy_tuple

    # call solver with 4th/5th order accuracy Runge-Kutta method
    sol = solve_ivp(fun      = eval_func,
                t_span   = [INT_START, INT_END],
                y0       = [B_IN, L_IN, G_IN, T_IN],
                method   = 'RK45',
                t_eval   = X_EVAL,
                atol     = ABS_ERROR,
                rtol     = REL_ERROR,
                max_step = MAX_STEP
                )

    print ("Solver success") if sol.success else print ("Solver error")

    return output

#-------------------------------------------------------------------------------
#%% execution
#%% solver call
output = solver()

#-------------------------------------------------------------------------------
#%% output
output_eval = eval_output(output)

#-------------------------------------------------------------------------------
#%% end of file
```

Appendix B.

Shear-stress–transport turbulence model

The model equations of the *k-ω shear-stress–transport* (*SST*) turbulence model by Menter et al. (2003), which was first published in Menter (1994), are given below in the notation of this thesis. The respective transport equations for the turbulent kinetic energy k and the specific turbulence-dissipation rate ω are (see also *Eqns* 5.14 and 5.15):

$$
\begin{aligned}
\frac{\partial(\rho k)}{\partial t} + \boldsymbol{\nabla} \cdot (\rho k \mathbf{u}) &= \tilde{\mathcal{P}}_k - \beta^* \rho \omega k + \boldsymbol{\nabla} \cdot \left[(\mu + \sigma_k \mu_{\mathrm{turb}}) \, \boldsymbol{\nabla} k \right], \\
\frac{\partial(\rho \omega)}{\partial t} + \boldsymbol{\nabla} \cdot (\rho \omega \mathbf{u}) &= \frac{\rho \alpha}{\mu_{\mathrm{turb}}} \tilde{\mathcal{P}}_k - \beta^* \rho \omega^2 + \boldsymbol{\nabla} \cdot \left[(\mu + \sigma_\omega \mu_{\mathrm{turb}}) \, \boldsymbol{\nabla} \omega \right] \\
&\qquad + 2 \, (1 - F_1) \, \frac{\rho \sigma_{\omega,2}}{\omega} \left[\boldsymbol{\nabla} k \cdot \boldsymbol{\nabla} \omega \right],
\end{aligned}
$$

where the limiter

$$\tilde{\mathcal{P}}_k := \min \left(\mathcal{P}_k ; 10 \beta^* \rho \omega k \right) \tag{B.1}$$

limits the production of turbulent kinetic energy, i.e.,

$$\mathcal{P}_k := \left[\boldsymbol{\tau}' : (\mathbf{u} \otimes \boldsymbol{\nabla}) \right]. \tag{B.2}$$

The turbulent viscosity is then

$$\mu_{\mathrm{turb}} := \frac{\rho a_1 k}{\max \left(a_1 \omega ; S F_2 \right)}. \tag{B.3}$$

Calibration
The cross-diffusion term in the transport equation of the specific turbulence-dissipation rate, i.e., the last term on the right-hand side is controlled by the *blending function*

$$F_1 := \tanh \left(\arg_1^4 \right), \tag{B.4}$$

where

$$\arg_1 := \min \left[\max \left(\frac{\sqrt{k}}{\beta^* \omega d} ; \frac{500 \nu}{d^2 \omega} \right) ; \frac{4 \rho \sigma_{\omega,2} k}{\mathcal{D}_{k\omega} d^2} \right], \tag{B.5}$$

where d is the wall distance and

$$\mathcal{D}_{k\omega} := \max \left\{ \frac{2 \rho \sigma_{\omega,2}}{\omega} \left[\boldsymbol{\nabla} k \cdot \boldsymbol{\nabla} \omega \right] ; 10^{-10} \right\} \tag{B.6}$$

is the limited cross-diffusion term. As a result, the cross-diffusion term is activated when the wall distance becomes sufficiently large.

The second blending function,

$$F_2 := \tanh\left(\arg_2^2\right), \tag{B.7}$$

with

$$\arg_2 := \max\left(\frac{2\sqrt{k}}{\beta^* \omega d}; \frac{500\nu}{d^2\omega}\right) \tag{B.8}$$

limits the turbulent viscosity in near-wall regions.

Model calibration
The model has two sets of calibration constants, i.e.,

$$\begin{aligned} \sigma_{k,1} &:= 0.85, & \sigma_{\omega,1} &:= 0.5, & \alpha_1 &:= 5/9, & \beta_1 &:= 0.075, & \beta^* &:= 0.09, \\ \sigma_{k,2} &:= 1.0, & \sigma_{\omega,2} &:= 0.856, & \alpha_2 &:= 0.44, & \beta_2 &:= 0.082, & a_1 &:= 0.31 \end{aligned} \tag{B.9}$$

which are interpolated linearly using the F_1 blending function:

$$\boxtimes = F_1 \boxtimes_1 + (1 - F_1) \boxtimes_2, \tag{B.10}$$

where $\boxtimes$ is a generic placeholder.

Boundary conditions
The boundary conditions are defined as follows:

$$\frac{\mathcal{U}_\infty}{\ell_{\text{domain}}} < \omega_\infty < 10 \frac{\mathcal{U}_\infty}{\ell_{\text{domain}}}, \qquad \omega_0 = 10 \frac{6\nu}{\beta_1 (\Delta d_1)^2}, \tag{B.11}$$

$$10^{-5} \frac{\mathcal{U}_\infty^2}{\mathrm{Re}_{\ell_{\text{domain}}}} < k_\infty < 0.1 \frac{\mathcal{U}_\infty^2}{\mathrm{Re}_{\ell_{\text{domain}}}}, \qquad k_\infty = 0. \tag{B.12}$$

Appendix C.

Scale-adaptive simulation approach

The model equations of the scale-adaptive simulation (SAS) method by Menter and Egorov (2010) are given below in the notation of this thesis. The source term (see also *Eqn.* 5.17)

$$\mathcal{P}_{\mathrm{SAS}} := \max\left\{\rho\zeta_2 S^2\left(\frac{\ell_{\mathrm{turb}}}{\ell_{\mathrm{vK}}}\right)^2 - C_{\mathrm{SAS}}\frac{2\rho k}{\sigma_\Phi}\max\left[\frac{1}{k^2}\left(\boldsymbol{\nabla} k\cdot\boldsymbol{\nabla} k\right);\frac{1}{\omega^2}\left(\boldsymbol{\nabla}\omega\cdot\boldsymbol{\nabla}\omega\right)\right];0\right\},$$

where (see also *Eqn.* 5.18)

$$S := \sqrt{2}\,\|\mathbf{S}\|_{\mathrm{F}} = \sqrt{2\mathbf{S}:\mathbf{S}}$$

is added to the transport equation for the specific turbulence-dissipation rate (*Eqn.* 5.15).

The source term increases the specific turbulence-dissipation rate and, therefore, reduces the turbulent kinetic energy when the modelled turbulence length scale

$$\ell_{\mathrm{turb}} := \frac{\sqrt{k}}{c_\mu\omega} \tag{C.1}$$

is large compared to the limited von Kármán length scale (see *Eqn.* 5.19), i.e.,

$$\ell_{\mathrm{vK}} := \max\left(\kappa\frac{\|(\mathbf{u}\otimes\boldsymbol{\nabla})\|_{\mathrm{F}}}{\|\boldsymbol{\nabla}^2\mathbf{u}\|_2};C_{\mathrm{S}}\sqrt{\frac{\kappa\zeta_2}{\frac{\beta}{c_\mu}-\alpha}\Delta}\right), \tag{C.2}$$

where the local cell size Δ is calculated from the determinant of the Jacobian matrix,

$$\Delta := |\,\mathbf{J}\,|^{1/3} = J^{1/3}. \tag{C.3}$$

This results in a decrease in the turbulent viscosity and facilitates the formation of unsteady, inhomogeneous flow structures.

The model constants are defined below:

$$\kappa := 0.4, \qquad \zeta_2 := 3.51, \qquad C_{\mathrm{SAS}} := 2.0, \qquad \sigma_\Phi := 2/3. \tag{C.4}$$

The Smagorinsky constant C_{S} must be calibrated specifically for the employed discretisation scheme (see Egorov and Menter 2008).

Appendix D.

Blending of spatial differencing schemes

The method of Strelets (2001) provides a blending between central and upwind differencing schemes to reduce numerical dissipation in flow regions where the SST-SAS model is active yet increase numerical stability in other flow regions. The equations are given below in the notation of this thesis. The inviscid fluxes of the central and upwind differencing scheme are interpolated linearly (see also *Eqn.* 5.22):

$$\mathbf{F}_{\text{inviscid}} = (1 - \sigma)\,\mathbf{F}_{\text{central}} + \sigma \mathbf{F}_{\text{upwind}},$$

where

$$\sigma := \sigma_{\max} \tanh\left(A^{C_{\text{H1}}}\right) \tag{D.1}$$

with

$$\sigma_{\max} := 1.0. \tag{D.2}$$

The argument of the blending function σ is

$$A := C_{\text{H2}} \max\left(\frac{C_{\text{DES}}\Delta_{\sigma}/\ell_{\text{turb},\sigma}}{g} - 0.5; 0\right), \tag{D.3}$$

where

$$\ell_{\text{turb},\sigma} := \sqrt{\frac{\mu + \mu_{\text{turb}}}{\rho c_{\mu}^{3/2} K}}, \tag{D.4}$$

$$K := \max\left(\sqrt{\frac{S^2 + \Omega}{2}}; 0.1\mathcal{T}^{-1}\right), \tag{D.5}$$

and

$$g := \tanh B^4 \tag{D.6}$$

with

$$B := C_{\text{H3}}\Omega \frac{\max\left(S; \Omega\right)}{\max\left(\frac{S^2+\Omega^2}{2}; 10^{-20}\right)}. \tag{D.7}$$

The calibration constants are

$$C_{\text{H1}} := 3.0, \qquad C_{\text{H2}} := 1.0, \qquad C_{\text{H3}} := 2.0. \tag{D.8}$$

In this work, the characteristic convective time was set to $\mathcal{T} = 5.920\,07 \times 10^{-4}$ s.

Appendix E.

Index of hypotheses and corresponding conclusions

The hypotheses and corresponding conclusions developed in this thesis are referenced and summarised below in *Tab.* E.1. Three additional conclusions which do not refer to any hypotheses are listed at the end of the table. The page numbers indicate the beginning of the particular sections in which the statements were made.

Table E.1.: Index of the hypotheses and corresponding conclusions stated in this work

Hypothesis			Conclusion		
Number	Sec. start	Statement	Number	Sec. start	Statement
Hyp. 4.1	*p.* 39	The sensitivity of the diffuser effectiveness towards a given stabilising vortex increases with the diffuser opening angle.	*Con.* 6.7	*p.* 70	The simulation results support *Hyp.* 4.1: the sensitivity of the effectiveness towards vortex-induced stabilisation increases with the diffuser opening angle.
Hyp. 4.2	*p.* 43	The stabilisation of the boundary layer does not depend upon the momentum deficit of the boundary layer, but only upon the circulation of the vortex.	*Con.* 6.4	*p.* 68	The modelling results agree with *Hyp.* 4.2: the sensitivity of the boundary layer towards vortex-induced stabilisation does not depend upon the momentum deficit of the boundary layer, but on the circulation of the vortex.

Continued on the following page

Table E.1 (continued)

Hypothesis			Conclusion		
Number	Sec. start	Statement	Number	Sec. start	Statement
Hyp. 4.3	*p.* 43	Shear stresses imposed by a vortex with a mathematically positive sense of rotation increase the boundary-layer stability in proportion to the vortex circulation.	*Con.* 6.5	*p.* 68	The modelling results show a linear dependency of the boundary-layer parameters displacement thickness and shape factor upon the vortex shear stresses. The results are, thus, consistent with the theory presented.
Hyp. 4.4	*p.* 43	Entrainment of boundary-layer fluid into the vortex decreases the boundary-layer stability in proportion to the vortex circulation.	*Con.* 6.6	*p.* 68	The modelling results show a strictly monotone dependency of the boundary-layer parameters displacement thickness and shape factor upon the vortex entrainment. The results are, thus, consistent with the theory presented.
Hyp. 4.5	*p.* 43	The vortex decay does not depend upon the momentum deficit of the boundary layer, but only upon the vortex circulation.	*Con.* 6.3	*p.* 65	The numerical results partially support *Hyp.* 4.5: the vortex decay is mostly dependent upon the vortex circulation and not upon the momentum deficit of the boundary layer. This conclusion is, however, not applicable to the case of low stabilisation numbers together with strong flow separation just downstream of the diffuser inlet.
Hyp. 4.6	*p.* 46	The diffuser effectiveness ϵ increases linearly with the stabilisation number Σ.	*Con.* 6.1	*p.* 63	The data confirm *Hyp.* 4.6: the effectiveness ϵ increases linearly with the stabilisation number Σ.

Continued on the following page

Table E.1 (continued)

Hypothesis			Conclusion		
Number	Sec. start	Statement	Number	Sec. start	Statement
Hyp. 4.7	*p.* 50	The total-pressure loss coefficient ζ of the diffuser decreases linearly with an increasing product of the extrapolation factor and the stabilisation number, i.e., $\Xi\Sigma$ with regard to an extrapolated reference $\Xi\zeta_{\mathrm{ref}}$.	*Con.* 6.2	*p.* 64	The data confirm *Hyp.* 4.7: the total-pressure loss coefficient decreases linearly with an increasing extrapolated stabilisation number $\Xi\Sigma$ with regard to an extrapolated reference $\Xi\zeta_{\mathrm{ref}}$.
N/A	N/A	N/A	*Con.* 6.8	*p.* 70	The simulation results show that the sensitivity of the extrapolated changes in the total-pressure loss coefficient towards the vortex-induced stabilisation increases with the diffuser opening angle.
N/A	N/A	N/A	*Con.* 6.9	*p.* 72	The simulation results show that the sensitivity of the diffuser effectiveness towards the vortex-induced stabilisation decreases gradually downstream of the separation location in the case of massive flow separation. It increases, however, in the case of attached boundary layers.
N/A	N/A	N/A	*Con.* 6.10	*p.* 72	The simulation results show that the sensitivity of the extrapolated changes in the total-pressure loss coefficient towards the vortex-induced stabilisation increases linearly with the diffuser length.

Curriculum vitæ

Personal information

Name	Dajan Mimic
Date of birth	7th November, 1990
Place of birth	Düsseldorf, Germany

School education

1997–2001	Elementary school, Düsseldorf, Germany
2001–2008	Humboldt-Gymnasium Düsseldorf, Germany: Abitur

Background

2008–2014	RWTH Aachen University, Germany: B. Sc., Mechanical Engineering
2014–2015	RWTH Aachen University, Germany: M. Sc., Aerospace Engineering
since 2016	Leibniz Universität Hannover, Germany: Institute of Turbomachinery and Fluid Dynamics, Research Assistant

Dajan Mimic
Hanover, Germany
October, 2020